The Bulge Globular Cluster Terzan 6 as seen from Multi-Conjugate Adaptive Optics and the HST

Graduation Thesis

Supervisor:

Chiar.mo Prof. Francesco R. Ferraro

Co-supervisor:

Dr. Emanuele Dalessandro

Presented by:

Martina Loriga

Contents

Introduction

The Bulge contains about 25% of the total mass of the Milky Way and represents the first massive structure to have formed. Hence, understanding its structure and evolution and constraining the properties of its stellar populations is key to describe the formation and early evolution processes of the Galaxy.

In this context, Bulge globular clusters (GCs) are useful tools to study the innermost regions of the Galaxy, as they share kinematics, spatial distribution and chemical composition with field stars. Indeed, GCs are among the most studied objects and they are generally acknowledged as fossil remnants of galaxy formation. In this respect, recent studies have shown that stellar systems in the Bulge traditionally catalogued as GCs, namely Terzan 5 and Liller 1, are fossil remnants of more massive structures that contributed to the formation and evolution of the Bulge.

Because of the differential extinction and stellar densities in the direction of the Galactic central region, Bulge globular clusters in general have been systematically excluded from large surveys and little is known so far about the physical properties of most of them. Only thanks to the recent development of the adaptive optics (AO) techniques, a huge improvement in the knowledge of these systems has been made.

The astrophysical object of study in this master thesis work is a globular cluster, named Terzan 6, located in the central region of our Galaxy, the Bulge. Because of that, it is one of the less studied globular clusters but some information can be derived from literature. In particular it is characterized by a mean color excess E(B-V)=2.35 and a high metallicity [Fe/H]=-0.56 (Harris 1996, 2010 edition[79]).

But, not only the presence of a large extinction can lead to some challenges in the observation, but also its spatial variation (*differential reddening*).

In our case of study, we exploited the superb capabilities of the multi-conjugated adaptive optics camera GSAOI at the GEMINI South Telescope, and the HST, which secure high-resolution diffraction-limited images from the optical to near-infrared bands.

The use of GEMINI near-infrared (NIR) filters J and K_s is fundamental to efficiently observe the system since they are less affected by interstellar absorption. The photometric information in the optical band is crucial for determining the extinction law and constructing a high-resolution reddening map in the direction of Terzan 6. In addition, the combination

of the available multi-epoch HST and GEMINI observations enables the determination of relative proper motions, from which cluster member stars can be solidly distinguished from Galactic field interlopers.

The main goal of this work is to provide an accurate characterization of the stellar population content of Terzan 6.

It is organized into 6 different chapters:

- **Chapter 1**: it provides a theoretical description of globular clusters in general, with their main characteristics and classification according to their position in our Galaxy. Then a more detailed description of Bulge globular clusters is presented along with their implication in our understanding of the Bulge formation history. In particular, the peculiar characteristics of Terzan 5 and Liller 1 are highlighted. Also, the information already available in the literature for Terzan 6 is reported.

- **Chapter 2**: it provides a technical description of the instruments exploited in this analysis: Gemini Multi-Conjugate Adaptive Optics System with the concept of adaptive optics in general and the Advanced Camera for Survey mounted at the Hubble Space Telescope.
  Then a detailed description of the adopted dataset is presented.

- **Chapter 3**: it describes in detail the photometric analysis and highlights the differences between the procedures adopted for Gemini and HST data.

- **Chapter 4**: the proper motion analysis and the differential reddening corrections are described in this chapter. They represent two important steps in the analysis of a Bulge globular cluster due to their position in our Galaxy.
  Also, a more general description of the extinction phenomena is provided.

- **Chapter 5**: it is dedicated to the analysis of the structural properties of Terzan 6. First of all, a general description of the most important structural parameters describing GCs is provided; then the estimation of the center of gravity of the stellar system is performed. By exploiting this information, the first radial density profile using resolved stars is obtained in order to derive information about the dynamical stage of the cluster.

- **Chapter 6**: the last chapter is dedicated to the derivation of the age of Terzan 6 by means of an isochrone-fitting approach. To this aim, the adopted analysis to constrain the color excess and distance modulus of the system is described.
  Finally the age of Terzan 6 is compared with that of other bulge GCs and its position in the age-metallicity diagram is explored.

Chapter 1

Globular clusters

This chapter aims to provide a general overview of the main properties of globular clusters, with a particular focus on their use as ideal dynamical laboratories and in the context of galaxy formation and evolution.

1.1   General characteristics

Globular clusters (GCs) are among the first objects to have formed in the Universe (**Fig. 1.1**).

Indeed, with ages of about 12-13 Gyr, they are some of the oldest systems for which ages are known and therefore they are extremely important for the so-called 'near-field cosmology', providing independent tests to cosmological models.

They have typical masses in the range 10^4-10^6 $M_\odot$ (corresponding to integrated luminosities M_V=-5 – -10) and compact sizes (≈ 10 parsec).

It has been traditionally believed that GCs formed from the collapse of a single molecular cloud and that they can be considered the best example in nature of a Simple Stellar Population (SSP): a stellar population made of single stars, having all the same age and sharing the same chemical composition.

While this definition can still be considered appropriate to a large extent, in particular as far as the age and Fe abundance are concerned, it is important to note that results obtained in the past 20-25 years have shown that virtually all GCs host sub-populations differing in terms of their light-element abundances (such as He, Na, O, N, C), the so-called 'multiple populations'.

When GCs are observed at small distances (typically in the Milky Way) and their stars are resolved, they enable statistically significant studies of sub-populations. In fact, all main canonical evolutionary sequences are well sampled thus providing a unique test for the stellar evolution theory.

Figure 1.1: One of the closest GCs to Earth: NGC 6397.

Finally, GCs are prototypical dynamical laboratories, being the only stellar systems able to undergo nearly all physical processes known in stellar dynamics.

Also, gravitational interactions among stars significantly alter the overall system energy budget and considerably affect the (otherwise normal) stellar evolution, even generating objects like blue straggler stars, millisecond pulsars, X-ray binaries and cataclysmic variables.

1.2 Color-Magnitude diagram

The ideal tool to use GCs for stellar evolution studies is the so-called Hertzsprung-Russel diagram (HRD), which shows the effective temperature (T_{eff}) on the abscissa and the bolometric luminosity (L) on the ordinate axis, and the corresponding observational version, the so-called color-magnitude diagram (CMD).

The CMD shows the color of a star (i.e. the difference between the magnitudes in two bands) and its magnitude. The CMD represents a snapshot of a stellar population at a fixed moment.

Similarly, in the HDR the sequence describing the different evolutionary stages for a fixed chemical composition and age is the isochrone.

We can briefly describe the different evolutionary sequences (**Fig. 1.2**) with their main characteristics:

- *Main Sequence (MS)*: it is the first evolutionary stage of a star, characterized by the hydrogen (H) burning in the core through 2 main processes (according to the star mass): pp-chain[1] ($M_{star} < 1.2 M_{\odot}$) or CNO-cycle[2] ($M_{star} > 1.2 M_{\odot}$).

---

[1]It is a set of thermonuclear reactions in which 4 H nuclei are fused to produce a nucleus of He ($T \approx 10^7$K).

[2]it is a set of thermonuclear reactions characterized by the same final results of the pp-chain in terms of
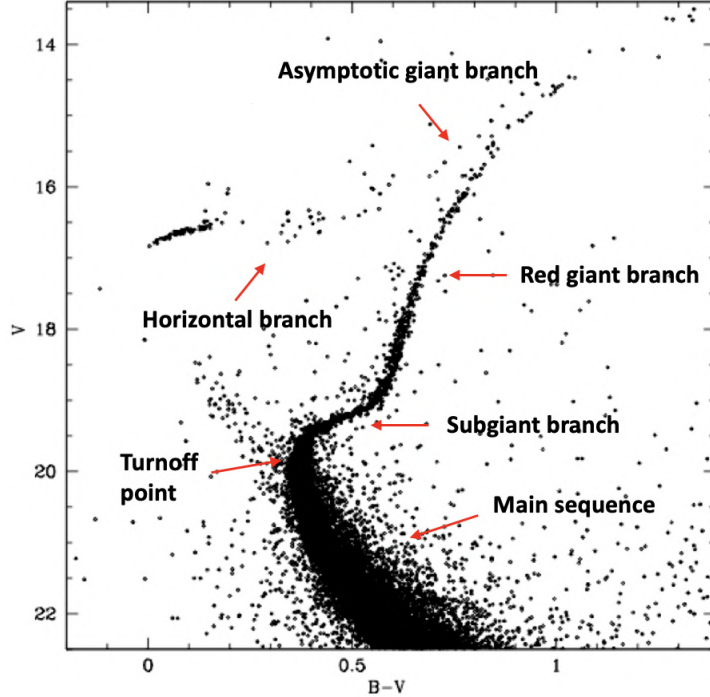
Figure 1.2: Example of a CMD of a GC located in our Galaxy (NGC5466)(Adapted from Beccari, 2013[5]).

It is the slowest evolutionary stage and so the most populated one.

One of the main features is MS-Turn Off (TO), corresponding to the H exhaustion in the core and the bluest point in the CMD. Also, the shape of the TO is related to the different processes of H burning in the core, going from the typical hook-like shape in the case of CNO-cycle, because of the need for a gravitational contraction in order to ignite the H burning in the shell, to a more 'smooth' transition in case of pp-chain. The mass of the star at the TO is the best feature for the determination of the age, but, since it is not an observable feature, it is possible to exploit the TO-luminosity as an age indicator of a stellar population.

- *Subgiant branch (SGB)*: it is an evolutionary stage characterized by the H burning in a thick shell. The amount of stars that can be found in this part of the CMD depends on the age of the stellar population, being less populated in the case of a young stellar population (*Hertzsprung gap*).

- *Red giant branch (RGB)*: it is composed of stars which are burning H in a thin shell in an evolutionary track parallel to the Hayashi tracks[3]. Due to their location, they are characterized by a convective envelope.

---

consumed H and produced He. The differences are related to the presence of C, N, O and their isotopes as catalysts, the energy budget, activation temperature (T$\approx 1.8 \times 10^7$K) and typical timescale.

[3]Fixed the chemical composition, it is a family of different masses which defines regions of hydrostatic equilibrium in the HR diagram where stars are completely convective.

In the case of an old stellar system ($M_{star} < 2.2 M_\odot$), the RGB is well extended and populated. The ending point is called *RGB tip* and if $M_{star} < 2.2 M_\odot$ it is characterized by the same luminosity, so it can be used as a standard candle.

Another important feature is the so-called *RGB bump* (**Fig. 1.3**) which represents the moment in which the discontinuity left by the propagation of the convection from the outer region up to the inner one encounters the H-burning shell. This leads to a temporary decrease of the luminosity and, from an observational point of view, an increase in the number of stars observed in a region along the RGB and a change in the slope of the luminosity function[4].
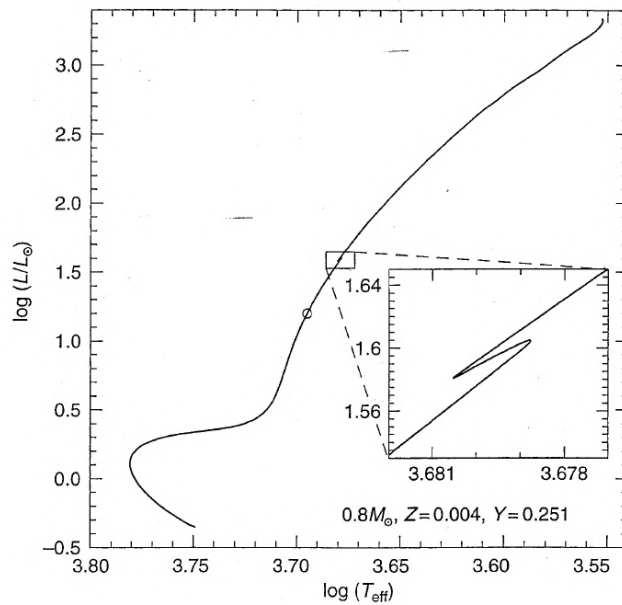

Figure 1.3: Example of an HR diagram in which the RGB bump feature has been highlighted.

- *Horizontal branch (HB)*: in this evolutionary stage, also called *Red clump (RC)*, stars are experiencing the He burning in the core and the H burning in the shell. It is characterized by stars with a convective core due to the 3α process[5].

  Its morphology is driven by different factors:

  - *Age*: increasing the age of a stellar system, the TO-mass decreases, like the RGB Tip one, which leads to a bluer HB.

  - *He abundance*: the increase of the He content produces the same effect of the age, so a bluer HB.

---

[4]It is a function which defines the number of stars in a given range of luminosity. So if we count stars in a representative volume, $\phi(L)\mathrm{d}L$ is the number of stars with luminosities between L and L + dL

[5]It is a set of thermonuclear reactions in which 3 He nuclei (the so-called α particles) are combined to generate a C nucleus ($T \approx 1.5 \times 10^8$ K).

– *Metallicity (Z)*: increasing Z means the development of a redder HB since the TO-mass becomes larger.

– *Mass loss*: increasing the mass loss (parametrized by the η free-parameter) means the generation of a bluer HB.

- *Asymptotic giant branch (AGB)*: it represents the evolutionary stage in which the H burning shell and the He burning shell are producing the energy needed for the support of the star evolution. It is characterized by two different stages:

    – *Early AGB*: it is characterized by the ignition of the He burning shell with the generation of convective motions and an expansion of the inter-shell region, leading to the H burning shell being switched off.

    – *Thermal pulses AGB*: after the exhaustion of the He, the He burning shell is switched off and the inter-shell region starts to contract leading to the activation of the H burning shell. This process produces the fuel for the He burning shell (*self-production* of He) that at some point it is active again.
    So this phase is characterized by an alternating ignition of these two shells.

The final stages of the evolution of a star are strongly dependent on its mass.

In the case of a massive star (M>$8M_\odot$), its evolution is characterized by the ignition of all the thermonuclear reactions up to the generation of a Fe core and its collapse as Type II Supernovae (SN II). These stars are the main polluters in terms of α elements, but also a small amount of Fe is produced.

Then if M<$25M_\odot$, the remnant of the SN II explosion is a *Neutron Star* (NS)[6], while if M>$25M_\odot$ is a *Black Hole* (BH)[7].

While if the star is characterized by a M<$8M_\odot$, it becomes a *White Dwarfs (WD)*[8] with a different composition according to the last thermonuclear reaction which was active in the core. If the mass of the core is larger than the Chandrasekhar mass ($M_{ch} = 1.44M_\odot$), the stellar structure is not in hydrostatic equilibrium due to the electron-degenerate gas anymore and the collapse can start. So if, in the case of a binary system, the mass transfer to the WD can lead to the overcoming of the M_{ch}, the star will explode as SN Ia. It can produce a huge amount of Fe and Fe-group elements in general.

In order to study the chemical enrichment, the $[\alpha/Fe]$ vs $[Fe/H]$ plot is fundamental (**Fig.1.4**), in which the y-axis is mostly driven by SN II, while the x-axis by SN Ia (even if

---

[6]Stellar structure with a mass of 1.2-1.5 $M_\odot$ composed by neutron-degenerate matter and a central density which can reach 10^{14-15} g/cm^3.

[7]It is an astronomical object characterized by a gravitational field so strong that not even light can escape.

[8]It is a stellar structure composed by electron-degenerate matter and a density $\approx 10^6$ g/cm^3, which cools down at almost constant radius in the WD cooling sequence, located on the left part of the CMD.

also a small amount of Fe is produced by SN II).

The typical enrichment timescale is completely different between the 2 processes, due to the different progenitors, being much shorter for SN II ($\approx 10^7$ yrs). It is difficult to quantify the timescale needed in the case of SN Ia but, since the development of a WD is necessary, it is for sure much longer than the one needed for SN II.

This is why, in the case of a younger stellar system, we expect the environment to be polluted mostly by α elements, leading to an increase in the extension of the plateau of the plot. This is strictly related to the number of massive and young stars present in the stellar population and so to the Initial Mass Function (IMF)[9] of the system.

At some point we can notice the presence of a change of the slope in the plot, the *"knee"* of the distribution, which identifies the moment in which the first SN Ia exploded, leading to an increase of the Fe amount and so a decrease of $[\alpha/Fe]$.

Also, the increase of the Star Formation Rate (SFR) produces the shift of the "knee" of the distribution to a larger value of [Fe/H]. This is due to the small production of Fe by SN II. This plot is also important because, according to the different Galactic components (halo, disk/bulge), the behavior is different. So it allows us to potentially identify in which region of the Galaxy a stellar system was formed (see **Sec. 1.3.1**).
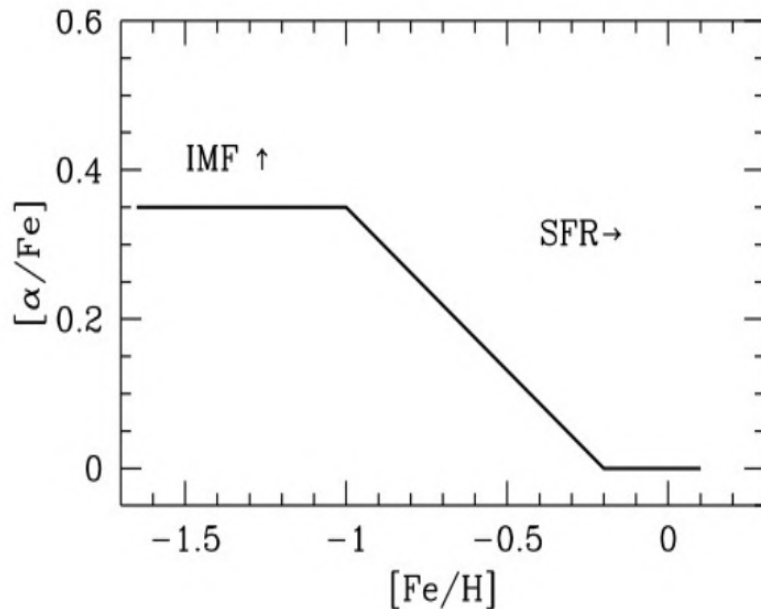

Figure 1.4: $[\alpha/Fe]$ vs $[Fe/H]$ plot, in which the effects of the increasing SFR and IMF are shown.

---

[9]The IMF is an empirical function that describes the initial distribution of masses for a population of stars.

1.3 Bulge Globular Clusters

After a systematic study by Harris et al., 1976[30], globular clusters were divided into two main categories according to their position in our Galaxy: halo globular clusters and disk/bulge ones. About 30% of the total population of Galactic GCs is located in the Bulge. The Bulge is one of the least accessible regions in the Milky Way and its structure, formation and evolution is still the subject of intense debate (see for example Rich 1998[62]; Ness et al. 2013[51]; Origlia et al. 2014[56]; Zoccali & Valenti 2016[82]).

The Galactic Bulge contains about one quarter ($6 \times 10^{10} M_\odot$) of the total stellar mass of the Milky Way and represents the oldest massive component of the Galaxy, made of 12-13 Gyr old stars. Understanding its structure and the properties of its stellar population is therefore of great relevance for all the theoretical models that aim at describing how the Milky Way Bulge and any galaxy spheroid formed and evolved with cosmic time.

However, the formation mechanisms of galaxy bulges remain an extremely debated subject, and the detailed characterization of the globular clusters orbiting the Milky Way central spheroid is one of the most promising ways to shed light on this topic.

There are two main theories used to explain the Bulge formation mechanism which are described by Immeli et al., 2004[32] by exploiting 3D chemodynamical models. It was shown that the galaxy evolution proceeds differently according to the efficiency of energy dissipation (η_{coll}) of the cold cloud component from which stars form.

1. If the η_{coll} is large, dynamical instabilities in the gas dominate the evolution, leading to the fragmentation of the disk into a small number of clumps. Since they are characterized by a large amount of cold gas, strong star formation events are ignited. The clumps start to interact with each other and with disk stars and, by losing angular momentum, start to spiral to the central region of the Galaxy, merging to form a centrally concentrated bulge. Simulations show that bulges formed in this way have properties typical of classical early-type bulges and the timescale from the formation of the clumps to the merging (≈ 1 Gyr) is compatible with a rapid formation mechanism, again typical of classical bulges (Elmegreen et al., 2008[21]). Because of the starburst origin, many of the bulge stars formed in this way are characterized by a large $[\alpha/Fe]$ abundance ratio.

2. If the η_{coll} is small, on the other hand, the system can form stars in a quiescent mode until the stellar disk becomes unstable, leading to a stellar bar at late times. Then, due to the bar instabilities, the gas is channeled into the central regions and the bulge can form in a longer timescale. In this case, the bulge is characterized by bar-like kinematics, meaning disk-like properties and a lower $[\alpha/Fe]$ abundance ratio.

Some theories also predict that the Bulge of our Galaxy is characterized by properties of both classical and pseudo-bulges. This is because there is evidence of two different populations in the Bulge of our Galaxy: an old, metal-poor population, characterized by a large $[\alpha/Fe]$ abundance ratio, which was born in a short timescale from gas polluted mostly by SN II; a younger metal-rich population formed from gas polluted also by SN Ia on a longer timescale (Grieco at al., 2012[29]).

1.3.1 Terzan 5 and Liller1

Among the Bulge Globular Clusters, two of them, Terzan 5 and Liller 1, have been largely studied in recent years after the discovery of the presence of sub-populations with a significant difference in age up to 7-10 Gyr and metallicity $\Delta[Fe/H] \approx 1$ dex (Ferraro et al. 2009[25], 2021[23]; Massari et al. 2013[43]; Origlia et al. 2011[55]; Dalessandro et al. 2022[18]).
Terzan 5 is a Bulge GC located at a distance of 2.1 Kpc from the Galactic Centre ($\alpha_{J2000} = 17^h48^m4.85^s$, $\delta_{J2000} = -24°46'44.6''$; Lanzoni et al., 2010[40]) in a region strongly affected by extinction phenomena (*reddening*, see **Sec. 4.2**) because of the large amount of dust along the line of sight, with an average value of E(B-V)=2.38 ±0.55 (Valenti et al., 2010[76]). Moreover, there are also spatial variations in the reddening values, the so-called *differential reddening* (see **Sec. 4.2.1**).
By exploiting the high-resolution images of Terzan 5 provided by a Multi-Conjugate Adaptive Optics demonstrator (MAD) instrument installed at the Very Large Telescope (VLT) of the European Southern Observatory (ESO) in the K and J band it was possible to notice the presence of two well defined red horizontal branch clumps in the central region of the cluster (**Fig. 1.5 (left)**). Also in the optical CMD, obtained from the Advance Camera for Survey (ACS) on board of Hubble Space Telescope (HST), it is possible to notice a bimodality in the HB (**Fig. 1.5 (right)**), even if strongly elongated by the effects of the differential reddening.
 Medium-resolution IR spectroscopic information of the six stars on the HB clumps obtained by using KeckII/NIRSPEC data demonstrates the existence of two sub-groups of stars with a difference in iron abundance of $\approx$ 0.5 dex: [Fe/H]=-0.2 for the fainter component, while [Fe/H]=+0.3 for the brighter one.
Also, a study on the α elements abundance and the possible presence of anti-correlations (like expected in the case of genuine GC) was performed by Origlia et al., 2011[55]. The absence of the typical Al-O anti-correlation was observed.
In addition, the two populations were found to show different $[\alpha/Fe]$ abundances. The metal-poor one appeared to be α-enanched ([α/Fe=+0.34]), so it is compatible with a short formation history from a gas enriched by SN II only; while the metal-rich one is characterized by solar-scaled [α/Fe], formed from gas enriched by both SN II and SN Ia.
This observational evidence is a clear hint of an auto-enrichment scenario in which Terzan
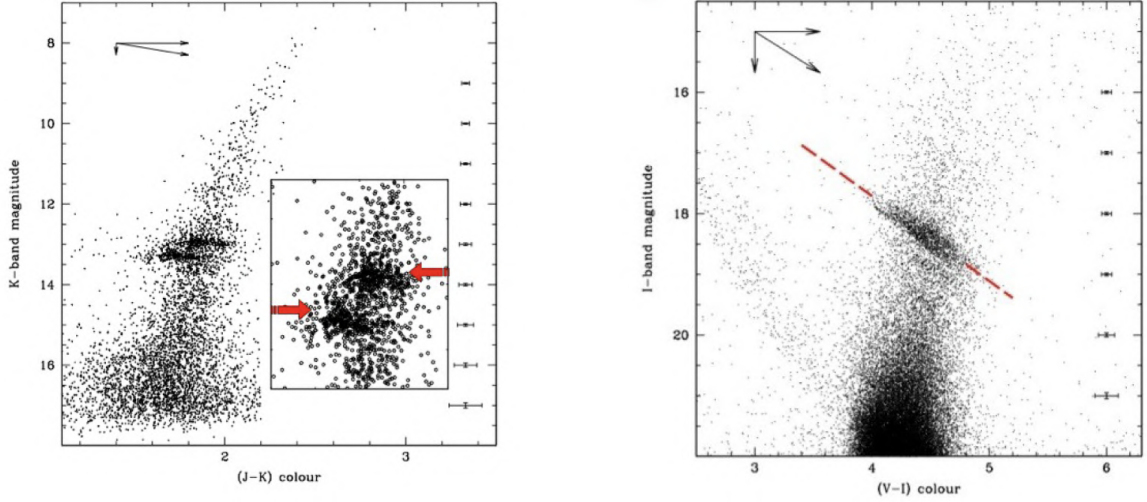
(a) *Infrared CMD obtained from MAD@VLT observations in which the two red clumps are highlighted .*

(b) *Optical CMD obtained from ACS@HST, in which the two parallel HB structures are divided by the dashed red line .*

Figure 1.5: Terzan 5 infrared and optical CMD (Ferraro et al., 2009[25]).

5 was able to retain the SN ejecta of the first generation of stars, from which the second generation was born. This requires a quite massive system, even more massive than the current one (M$\approx 10^6 M_\odot$, Lanzoni et al. 2010[40]).

Thanks to these studies it was understood that the best filter combination in order to highlight the possible presence of multi-populations is the one composed of optical and IR filters as shown in **Fig.1.6**. By exploiting the differential reddening corrected CMD it was possible to derive the ages of the 2 populations: t=12 Gyr for the metal-poor one and t=6 Gyr for the metal-rich one.

Liller 1 is a Bulge GC that shows similar characteristics to Terzan 5 in terms of the position occupied in our Galaxy and the metallicity ([Fe/H=-0.30], Origlia et al. 2001[54]). It is located at 0.8 Kpc from the Galactic Centre ($\alpha_{J2000} = 17^h 33^m 24.5^s$, $\delta_{J2000} = -33°23'20''$, Harris et al. 1996[7]) and so it is affected by a large extinction (E(B-V)$\approx$ 3.07, Harris et al. 1996[7]) like the case of Terzan 5.

In the first ultra-deep observations of this system in the optical band (V, I bands images acquired by ACS/HST) and NIR (J, K band images obtained with the multi-conjugate adaptive optics systems GEMS/GSAOI mounted at the Gemini South telescope) revealed the presence of sub-populations (**Fig.1.7**) with a significant variation in age of about 10 Gyr (Ferraro et al., 2021[23]).

In fact, in the (I-K, K) CMD 3 main features can be identified: a sparse stellar population associated with the MS of the Galactic disk, a dominant old population resembling the one of Terzan 5, and a younger, very populated one (*Blue Plume*) extending up to 4 mag above the MS-TO, in the typical position occupied by Blue Stragglers Stars (BSS).
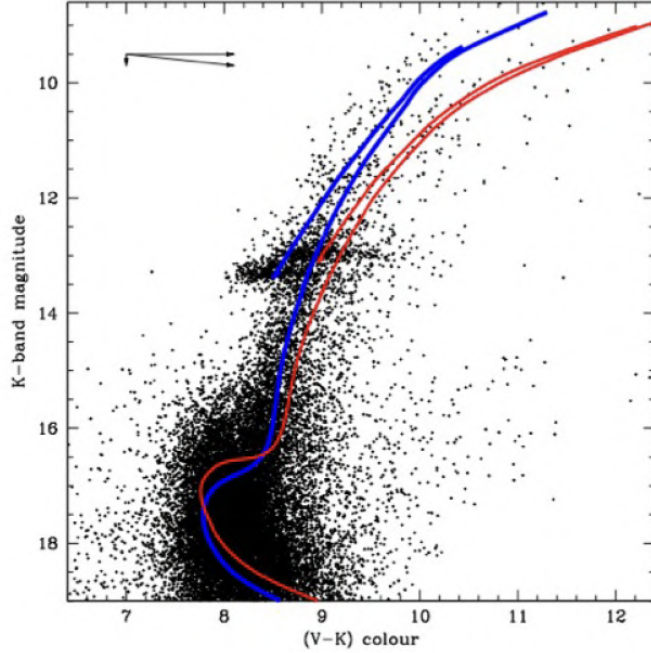
Figure 1.6: Differential reddening corrected (V-K, K) CMD in which 2 isochrones of 12 Gyr (blue) and 6 Gyr (red) are plotted to highlight the 2 different populations (Ferraro et al., 2009[25]).

By performing proper motion studies and constructing the radial density profiles, the cluster's membership of the older and younger stellar populations was confirmed.

The first spectroscopic investigation (Crociati et al., 2023[15]) showed a metallicity spread of the order of 1 dex, with an older metal-poor [Fe/H=-0.5] sub-population and a younger and metal-rich one [Fe/H=+0.3].

A detailed analysis of the CMD of the system (Dalessandro et al. 2022[18]) has shown that Liller 1 must have undergone an extended and bursty star formation history, with two main events that took place ≈12 Gyr and ≈2 Gyr ago.

While Terzan 5 and Liller 1 may differ in a few detailed aspects, they have in common the critical fact that the resulting chemical patterns of their populations nicely overlap those observed for Bulge stars, thus suggesting they can be strictly related to the Bulge formation mechanisms (**Fig.1.8**).

The most probable hypothesis is that they belong to a new category of stellar systems called *Bulge Fossil Fragments (BFF)*(Ferraro et al., 2009[25]), which are remnants of massive clumps which formed the Bulge of our Galaxy (see **Sec. 1.3**).

Moreover, the so-called *clumpy* or *chain galaxies* observed at z>2 (Elmegreeen et al., 2008[21]) confirmed the possibility of the existence of massive clumps characterized by a mass of $\approx 10^8 M_\odot$, large enough to retain SN ejecta.

So, if this scenario is confirmed, it can lead to a huge improvement in the knowledge of the formation mechanisms of not only the Bulge of our Galaxy but any galaxy's bulges.
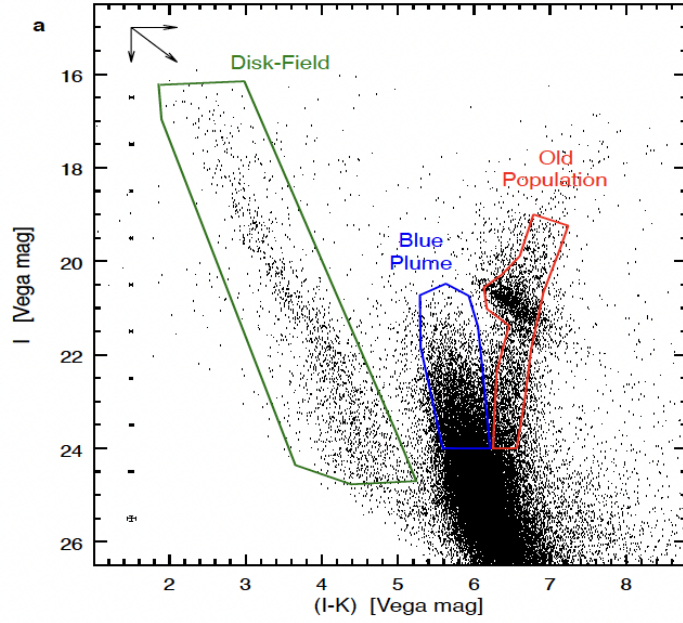
Figure 1.7: (I-K, K) CMD in which the different populations are highlighted (Ferraro et al., 2021[58]).
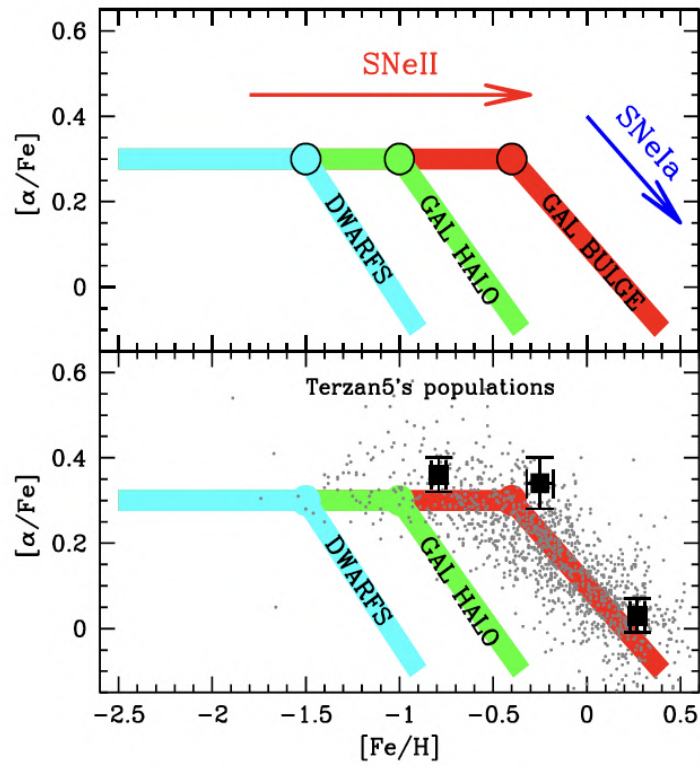

Figure 1.8: Illustration of $[\alpha/Fe]$ vs $[Fe/H]$ pattern in 3 different environments (Local Group dwarf galaxies, the Galactic Halo and the Bulge). In the lower panel, the sub-populations of Terzan 5 are shown.

1.3.2 Terzan 6

The stellar system which is analyzed in this master thesis work is Terzan 6 and, like Terzan 5 and Liller 1, is a Bulge Globular Cluster ($l = 358.571°, b = -2.162°$, Barbuy et al., 1997 [3]). It is located at a distance of 1.3 Kpc from the Galactic Centre and it was discovered by Terzan (1968) [75] with Schmidt plates obtained at the Haute-Provence Observatory. Its position in the Bulge of our Galaxy is shown in **Fig.1.9**.

Due to its vicinity to the Galactic Centre, the GC is heavily obscured because of the large
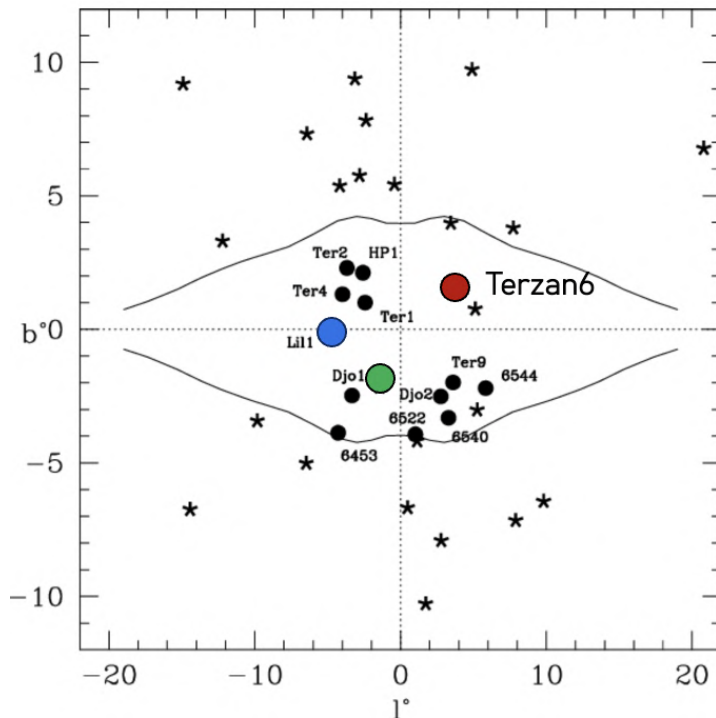

Figure 1.9: The position of different Bulge Globular Clusters in galactic coordinates. The colored dots show the position of Terzan 6 (red), Liller 1 (blue), Terzan 5 (green) (Adapted from Valenti et al., 2010[76]).

amount of dust along the line of sight (LOS), with the consequence of being strongly affected by interstellar absorption. The mean extinction is $A_V \sim 7.3$ mag ($E(B - V) = 2.35$, Harris 1996, 2010 edition[79]).

This is why Terzan 6 is one of the less-studied bulge GCs. In addition, Terzan 6 is also one of the most crowded GCs in the Galaxy.

So far Terzan 6 has been observed only with ground-based seeing-limited instruments. In particular, in the observational campaign of Fahlman et al., 1995[22], they exploited the Las Campanas Infrared Camera at the 2.5m Irénée du Pont Telescope (Chile). The camera detector is constituted of an array of 256x256 pixels and the images were obtained in the J, H and K bands with a resolution of 0.348 arcsec/pixel and a FOV of 89 arcsec^2.

It was also observed at the ESO, using the 3.55 m New Technology Telescope (NTT) and the

Danish 1.54 m telescope (Barbuy et al., 1997 [3]). At the NTT the observations were carried out under excellent seeing conditions (0.6") by using the SUSI camera, which employs a 1024x1024 CCD. The pixel size is 24 μm and the frame size is 2.2'x2.2'.

While at the Danish telescope, they used a 1024 $\times$ 1024 pixels CCD, with pixel size 24 μm, corresponding to 0.37 arcsec/pixel and a FOV of 6.3' $\times$ 6.3'.

The images obtained in these observational campaigns are shown in **Fig.1.10**.
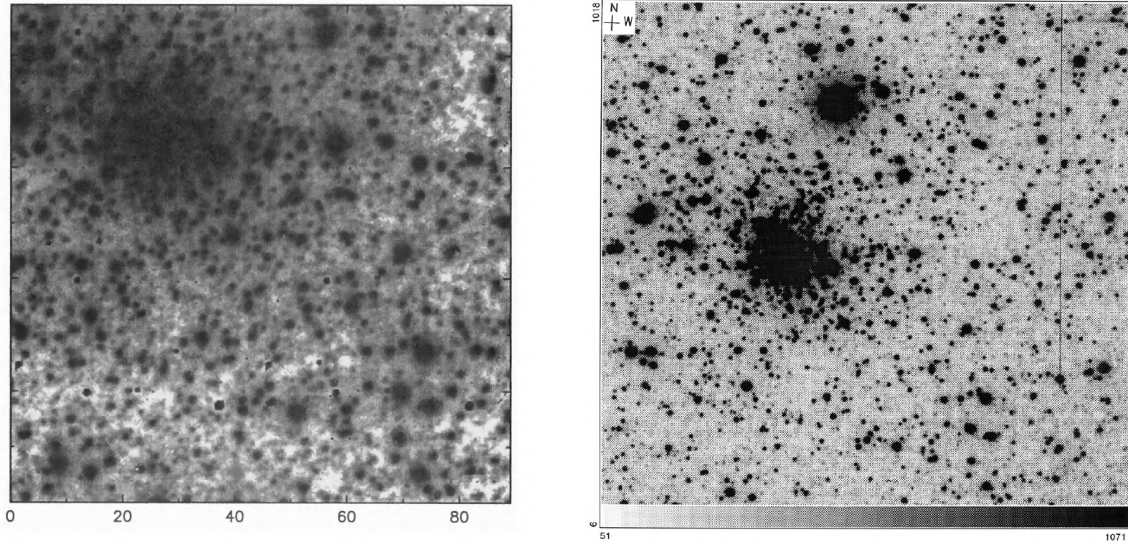
(a) *Negative H band images obtained as the average of 100 $\times$ 5 s images, Las Campanas Infrared Camera.*

(b) *NTT SUSI image.*

Figure 1.10: Comparison between 2 different images of Terzan 6 from literature.

Chapter 2

Ground-based and space observations: setting the dataset

For the study of the stellar population in Terzan 6 we used a powerful combination of ground-based and space observations. We exploited a multi-wavelength high-resolution diffraction limited data set from space (with the Hubble Space Telescope) and from the ground (with the Gemini Multi-Conjugate Adaptive Optics system (GeMS) working with the Gemini South Adaptive Optics Imager (GSAOI) mounted at the 8mt Gemini South telescope).

The aim of this chapter is to provide a detailed description of both instruments exploited in the analysis.

Many of the concepts presented in the following section have been adapted from Astronomical Instrumentation lectures (Rodeghiero, 2022 [65]).

2.1   Ground-based Observations with Adaptive Optics

In order to introduce the basic ideas behind AO astronomical instrumentation, it is necessary to start by analyzing the problem which leads to its development.

The presence of atmospheric turbulence represents a significant limitation for ground-based instrumentation as it transforms a plane wavefront coming from a distant object into a distorted one when it arrives at the telescope. This phenomenon is called atmospheric seeing, meaning a worsening of the angular resolution from the diffraction-limited one ($\Theta = \frac{1.22\lambda}{D}$, the so-called Airy profile, due to the optics of the telescope itself) to the seeing limited one, defined as $\Theta \propto \frac{\lambda}{r_0}$, where r_0 is the so-called Fried parameter (**Fig. 2.1**).

The r_0 parameter defines the scale length within which the wavefront phase is unperturbed. It depends on the zenith angle and the integral of the index of refraction structure coefficient C_n^2, related to the parametrization of the turbulence

$$C_n^2 = C_t^2[77.6 \cdot 10^{-6}(1 + 7.52 \cdot 10^{-3}\lambda^{-2}\frac{P}{T^2})]^2 \tag{2.1}$$
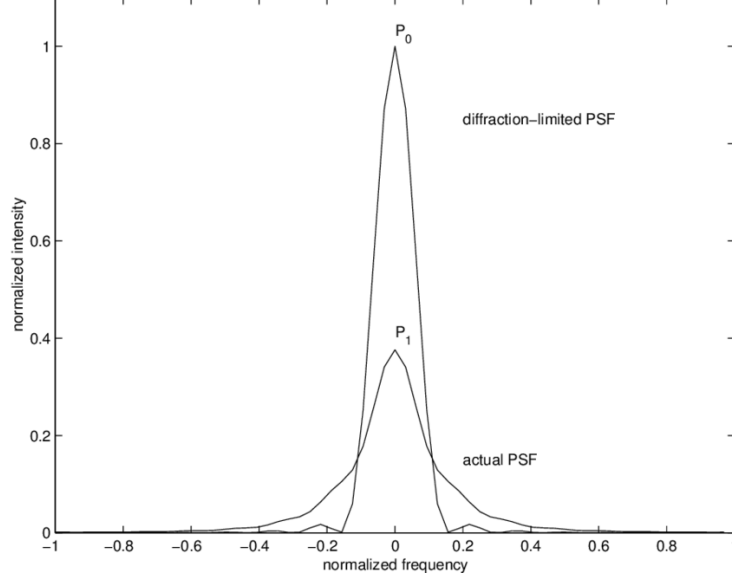
Figure 2.1: Effect of the turbulence on the Point Spread Function (PSF) starting from a diffraction-limited profile (Irwan, 2023[33]).

where $C_t^2 = \frac{D_t(r)}{r^{2/3}}$ and D_t the delta temperature between 2 different points at a distance r, P is the pressure and T the temperature.

The Fried parameter is characterized by a strong dependence on the wavelength ($\propto \lambda^{6/5}$), so it increases going from the optical to the NIR band.

An important parameter that can be defined is the coherence time, meaning the interval of time in which the wavefront phase can be considered constant

$$t_0 \approx 0.314 \frac{r_0}{v} \tag{2.2}$$

It represents the time interval in which the correction for the atmospheric turbulence must be performed on the system.

Since t_0 depends on the r_0 parameter, it has the same dependence on the wavelength and this can explain why the use of the AO technique is "easier" in the NIR band (larger wavelength means larger r_0 and t_0, so more time to correct for the atmospheric turbulence).

2.2 The Adaptive Optics technique

The solution to the seeing problem was found in the concept of Adaptive Optics (Babcock, 1953 [2]), which consists of 3 main components:

1. **WaveFront Sensor (WFS)** to measure the aberrations present in the wavefront;

2. **Deformable Mirror (DM)** to correct for the aberrations, thanks to the presence of different actuators able to perform negative corrections;

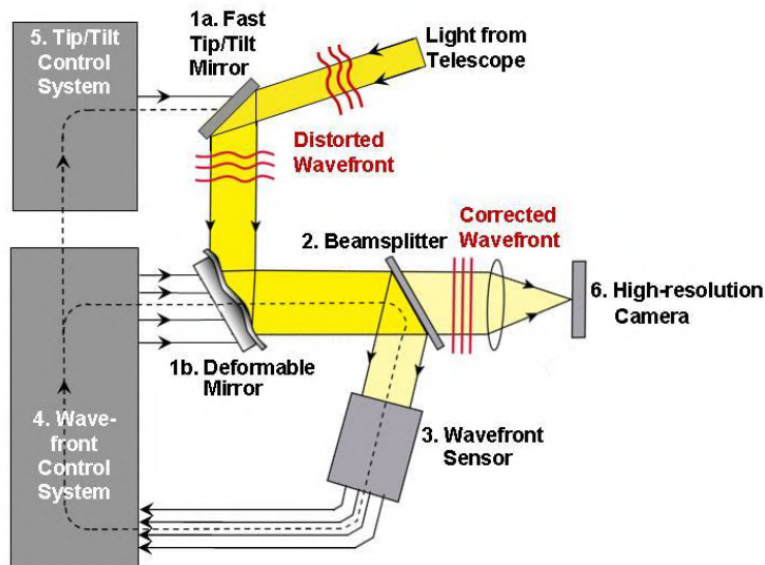3. **Real Time Computer (RTC)** to command the corrections to the DM.

Figure 2.2: AO system scheme.

As we can notice in **Fig. 2.2**, the perturbed wavefront passes through 2 different mirrors since the aberrations can be decomposed in a weighted sum of different orders Zernike Polynomials[1]. The first one is a Tip-Tilt (TT) mirror which corrects for the radial and azimuthal components of the first-order aberrations, related to the motion of the PSF on the focal plane, while the second DM, characterized by more actuators, is used for the correction of the higher order aberrations. When possible, it is always better to split the corrections into 2 DMs since the amplitudes of the corrections are different.

Then the wavefront passes through a beam splitter so that half of it is used for scientific purposes, after being corrected, while the other half passes through the WFS and the control system to evaluate the corrections and later apply them to the DMs. It is possible to use a dichroic filter so that the light is split according to the wavelength.

One of the main performance figures of merit of an AO system is defined by the so-called sky coverage, which is the fraction of the sky for which the system provides a useful level of atmospheric turbulence correction. An important aspect to take into account is that the wavefront sensing is performed on a guide star, which should be within the isoplanatic angle of the target so that the same correction can be applied.

The **isoplanatic angle** (Θ) is an important concept that can be defined, according to a representation of the atmosphere as the sum of lenses (Rigaut & Neichel, 2018 [64]), as the angle subtended by a lens, within which the turbulence of different wavefronts is correlated.

---

[1]Orthonormal polynomials defined as $Z_n^m(\rho, \theta) = N_n^m R_n^m(\rho) cos(m\theta)$, where N_n^m is a normalization factor, R_n^m the radial term and $cos(m\theta)$ the azimuthal one.

It can be written as:

$$\Theta = 0.94 \left[\int C_t^2(z) dz \right]^{3/5} \tag{2.3}$$

The first idea about guide stars was considering real astronomical sources (stars, planets, moons, etc.) located close to the target, the so-called Natural Guide Stars (NGS) (Wizinowich, 2015 [80]). They should be bright enough to be used to measure the wavefront aberrations.

This first category of guide stars is characterized by several limitations since it is not always possible to find a bright astronomical object within the same isoplanatic angle of the scientific target.

However, by increasing the telescope diameter it is possible to improve the number of detectable stars reaching fainter magnitudes and so increasing the percentage of coverage. Despite this, the so-called **sky coverage problem** is still present and it can be partially solved by the introduction of the Laser Guide Stars (LGS).

They are artificial stars which come in 2 main varieties:

1. Sodium-wavelength (Na) (Foy & Labeyrie, 1985 [28]): produced by an artificial laser diode which can excite the Na atoms released by the meteoroids in the upper Mesosphere layers ($\approx 90 km$ above the ground). These atoms re-emit at the same wavelength of the inelastic scattered laser photon (589.2 nm);

2. Rayleight: generated by a high-power artificial laser (UV or green wavelengths usually, for example, neodymium-doped yttrium aluminum garnet or lithium niobate solid-state lasers) which exploits the Rayleight back-scattering from air molecules (N_2, O_2 etc.) at a maximum distance of 10-35 km from the telescope. The maximum altitude is set by the exponential decay of the atmospheric density.

Despite the huge improvement in the sky coverage, LGS are still characterized by some limitations:

- **Cone-effect or Focus Anisoplanatism** (Foy & Labeyrie, 1985 [28]): due to the finite distance at which the artificial star is generated, the area covered in the sky is not represented by a cylinder, as expected in case of a NGS due to the infinity distance, but by a cone. So a small deviation between the measured distortions and those experienced by the light from the science object is generated and it increases with the altitude of the turbulence.

- **Elongation** (Clare, 2007 [13]): due to the finite extension of the Na layer in the atmosphere and the slightly off-axis position of the laser emitted light compared to the telescope entrance pupil, the produced image spot in the detector is severely elongated. The consequence, for example, can be an ambiguity in the determination of its centroid

in the Shack-Hartmann WFS[2] and so in the slope of the wavefront. Also, the spot shape is not constant, but it varies with time because of the layer changes in atom density, altitude and thickness leading to focus errors for the LGS AO system (Pfrommer & Hickson, 2010[59]).

- **TT indetermination** (Rigaut & Gendron, 1992 [63]): as previously said, the introduction of LGS can 'partially' solve the problem of the sky coverage because NGS are always needed to perform the TT correction. Indeed, the LSG are projected from the ground, so the light travels upward and downward along the same path without providing a correction. In this case, the use of NGS is not a huge problem because also faint stars can be easily exploited since all the aperture is used to collect the TT information.

Moreover, another problem is related to aircraft traffic since the laser can be potentially dangerous, so it should be shut down during the passage of airplanes. Also, the presence of clouds can attenuate the laser light.

Even if some problems are still present, the introduction of the AO system brought already a huge improvement in terms of achievable angular resolution for ground-based observations.

2.2.1 Multi-Conjugate Adaptive Optics

There are different possible configurations for Adaptive Optics systems based on the different number of components (WFS, DM) and the atmospheric layers with which they are coupled. One of the best possibilities is the Multi-Conjugate Adaptive Optics system (MCAO), described for the first time by Beckers (1989)[6]. In this configuration, several DMs are stacked in a series to form a 3D corrector, which can then be optically conjugated to the whole turbulent volume and thus provide anisoplanatic correction (Rigaut & Neichel, 2018 [64]).

The main advantage of using this system is the possibility to provide a uniform atmospherical correction on a larger Field of View (FoV) by exploiting different NGS and LGS located in different positions in the sky. The approach used is the so-called tomographic one, which can be simply described as a mathematical method to reconstruct 3D content based on multiple projections of the 3D content onto 2D measurements from different angles (Rigaut & Neichel, 2018 [64]).

Fig.2.3 shows one of the 2 possible configurations for a MCAO system, the so-called **Star Oriented MCAO**, in which there are N WFS for N different guide stars.

---

[2]One of the most used WFS, characterized by a lenslet array in the pupil plane of the telescope which splits the pupil itself into different sub-apertures, each of them imaged as a spot in the detector. By measuring the centroid of each spot, related to the first moment of the wavefront, we can infer the Zernike coefficients and reconstruct the wavefront.
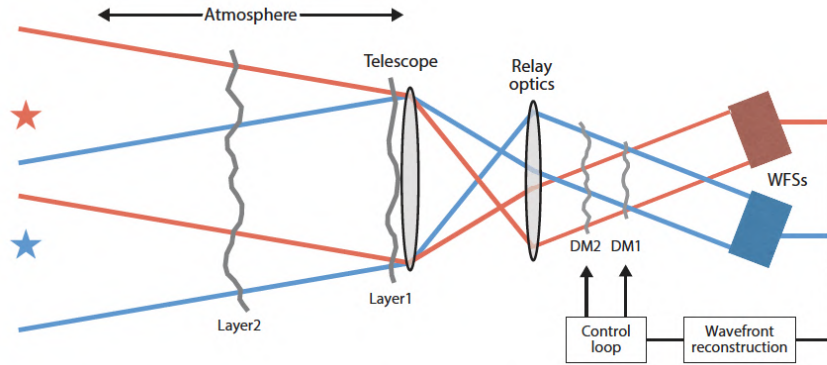
Figure 2.3: MCAO scheme.

The other possibility is a **Layer Oriented MCAO** (Ragazzoni, 2000 [61]) in which there is a correspondence between the number of WFS and the number of turbulent layers that are sampled (usually 2-3) and it is based on the concept of Piramid WFS[3].

The Multi-Conjugate Adaptive Optics Demonstrator (MAD) is the first MCAO systems prototype realized by the European Southern Observatory (ESO) and it was mounted at the Nasmyth platform of the Very Large Telescope (VLT) UT3 in Cerro Paranal, Chile in 2008. The project was developed by ESO in collaboration with two external consortia that developed strategic components of the system, for example, the layer-oriented MCAO (Marchetti, 2007 [42]).

MAD was designed to provide corrections at NIR wavelengths on a FoV of 2 arcmin by exploiting up to 3 NGS and 2 DM conjugated to the ground turbulence layer and an altitude of 8.5 km (Neichel, 2014 [49]).

The improvement provided by MAD can be seen in **Fig.2.4**, in which the image of the Galactic Centre has been cleaned up from the blurring effect of the atmosphere.

2.3 GeMS

The Gemini Multi-Conjugate Adaptive Optics System (GeMS) is the first sodium layer-based multi-LGS AO system used in astronomy. It is mounted at the 8.1mt GEMINI South Telescope in Chile and it delivers near-diffraction-limited images in the wavelength range of 0.9 - 2.5 μm.

GeMS is made of two main sub-systems (Neichel, 2014 [49]):

- The *LGS Facility (LGSF)* that includes a 50 W laser and an optical system called Beam Transfer Optics (BTO) that relays the laser light and controls the LGS;

---

[3]A pyramid (four-facet prism) is placed at the telescope focus and it slices the pupil in four equal pupils that are re-imaged with a lens. Like the Shack-Hartmann WFS, the aim is to measure the local slopes (derivative) of the wavefront.
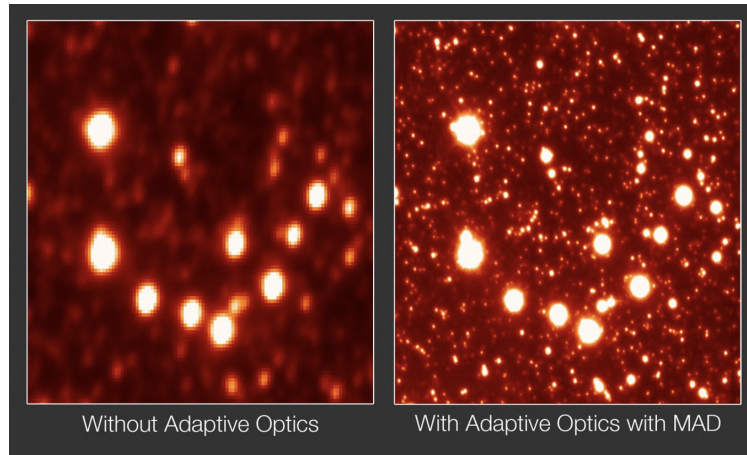
Figure 2.4: Galactic Centre images comparison before and after the development of MAD (ESO [52]).

- *CANOPUS*, the MCAO bench.

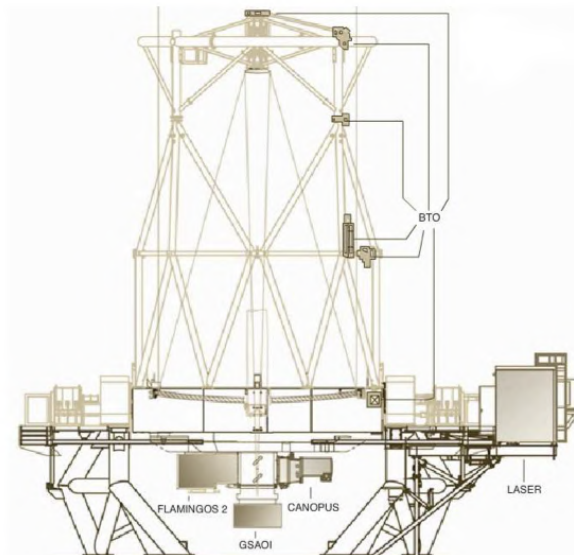A scheme of its components is shown in (**Fig.2.5**).

**Figure 2.5:** GeMS scheme (Gemini observatory [53]).

In short, the 50 W laser is split into 5 beams of 10 W by a series of beam splitters to produce 5 LGS projected on the sky at the corners and center of a 60" square. These LGS feed five 16x16 sub-apertures Shack-Hartmann WFS. The slope measurements are used to compute the MCAO high-order correction provided by two deformable mirrors conjugated to 0 and 9 km. In addition, up to three visible NGS provide the measurements for the compensation of the tip-tilt and anisoplanatic modes.

GeMS performance is analyzed, for example, by considering the distribution of the Strehl ratios[4] and the PSF as a function of the seeing, exploiting a constellation of three NGS with

---

[4]The Strehl Ratio (S) is used to quantify the resolution of the telescope and the difference from a

exposure times between 10 and 180 seconds (**Fig.2.6**).

The K-band data are represented by the red circles, the H-band by the green squares and the J-band by the blue triangles, while the full lines are median values of the Strehl ratio. As expected, decreasing the seeing value the field average Strehl ratio increases while the Full Width Half Maximum (FWHM) decreases meaning that the image quality increases. Also, the performances of the system are increasing as a function of the wavelength, as explained in **Sec. 2.1**.
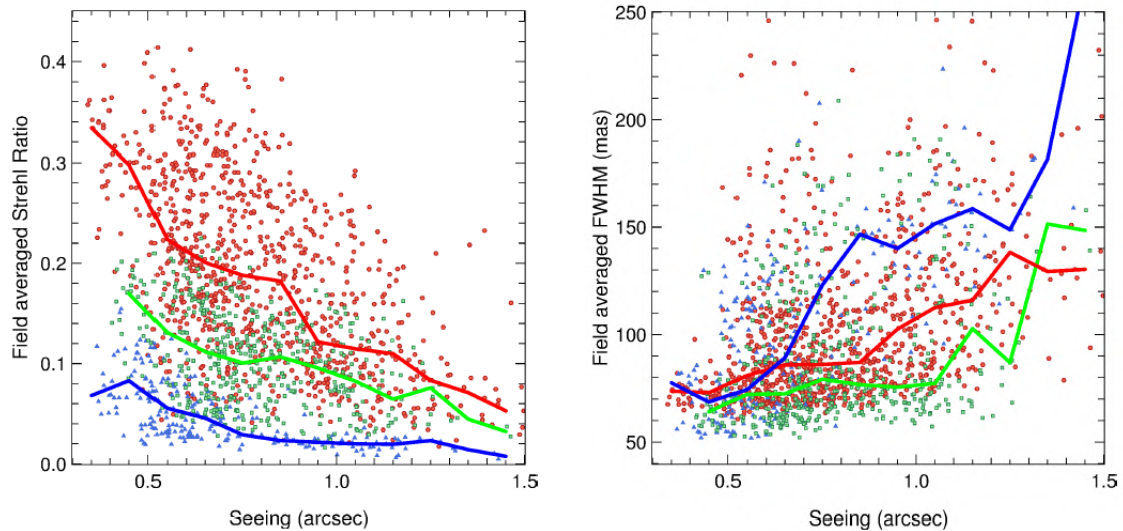
(a) *Field average Strehl ratio as a function of the seeing.*

(b) *Field average FWHM as a function of the seeing.*

Figure 2.6: Performance analysis of MCAO (Neichel, 2014 [49]).

The main instrument used to date is the Gemini South Adaptive Optics Imager (GSAOI), a 4k x 4k NIR imager covering 85" x 85" designed to work at the diffraction limit of the 8-meter telescope with a spatial sampling of 0.02"/pixel. This is the instrument that has been used for the observations discussed in this Thesis and the FOV is shown in **Fig.2.7**.

2.4 Observations from space: The Hubble Space Telescope

Hubble Space Telescope is a Cassegrain reflector telescope launched on 25 April 1990 by NASA. It represents a long-term, space-based observatory with regular servicing missions. Like a classical Cassegrain reflector, the light passes through a tube up to the 2.4m primary mirror and then it is reflected to the 0.3m secondary mirror. Lastly, the light is focused in a central hole in the primary mirror, where the focal plane is located and the different instruments are placed. A scheme of its components is shown in **Fig.2.8**.

---

diffraction-limited one. It is defined as the ratio of the maximum intensity of an actual image to the maximum intensity of a fully-diffraction limited image normalized to the same total flux.
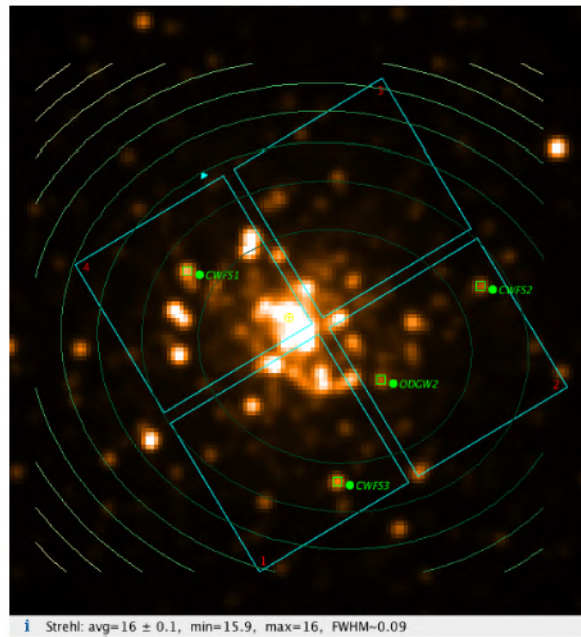
Figure 2.7: GSAOI FOV with the chip positions (cyan squares) (Neichel, 2014 [49]).
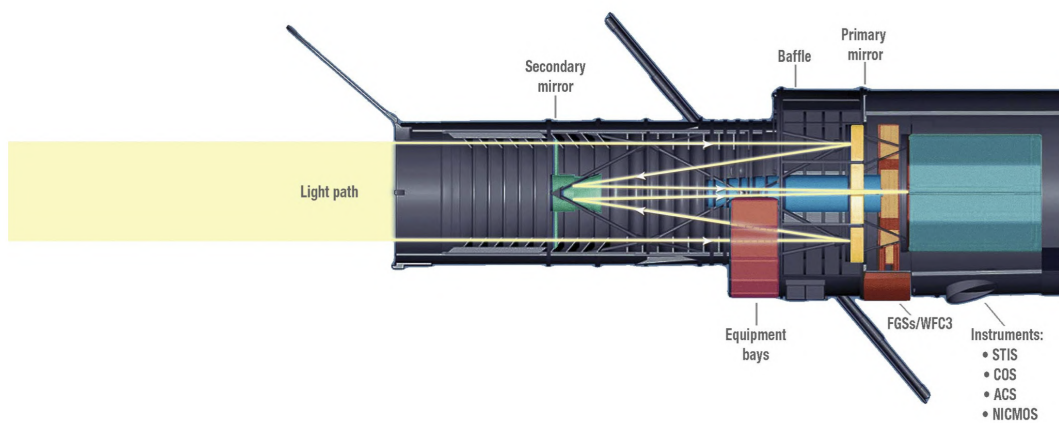

Figure 2.8: HST scheme (NASA [48]).

Hubble is currently composed of 5 instruments: Wide Field Camera 3 (WFC3), Cosmic Origins Spectrograph (COS), Advanced Camera for Surveys (ACS), Space Telescope Imaging Spectrograph (STIS) and Fine Guidance Sensors (FGS) (**Fig.2.9**).

In the past, there was also a sixth instrument, the Near Infrared Camera and Multi-Object Spectrometer (NICMOS) which was decommissioned in 2008.
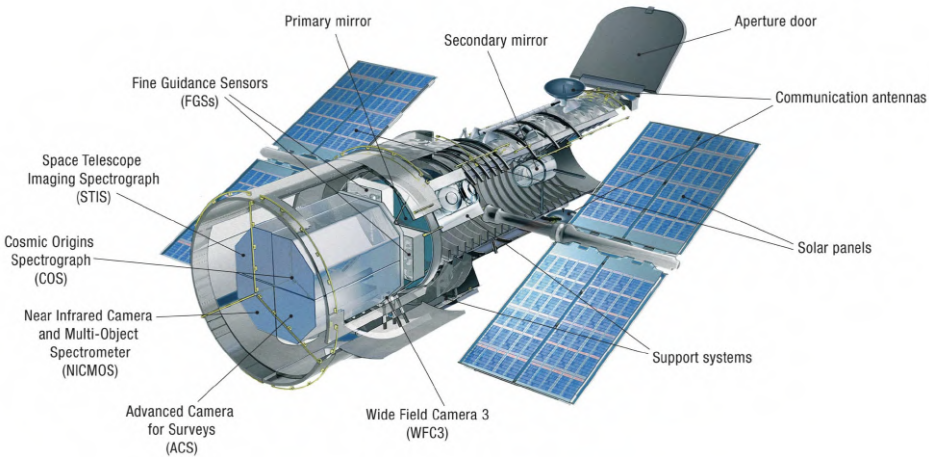

Figure 2.9: HST instruments, (NASA [48]).

The wavelength range covered by each of these instruments is shown in **Fig.2.10**, going from ultraviolet to infrared.
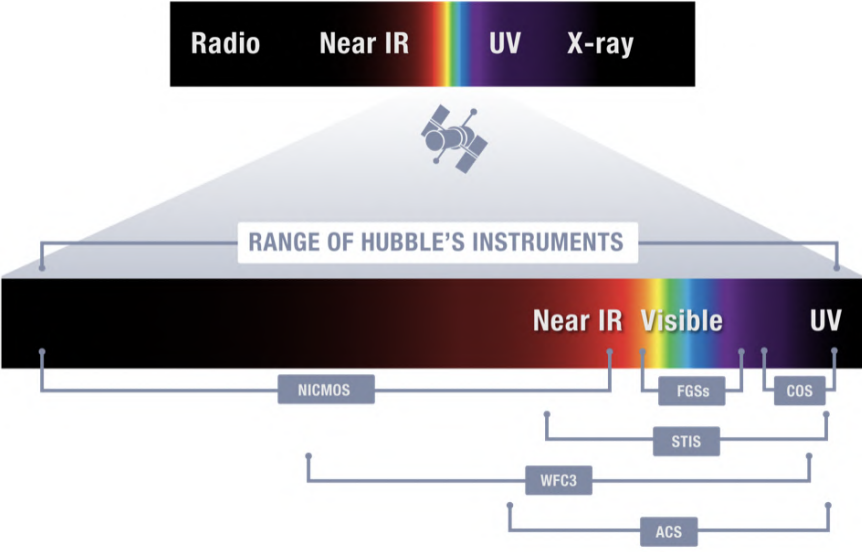

Figure 2.10: Wavelength range covered by Hubble's instrument (NASA [48]).

The WFC3 extended the HST wavelength range and, thanks to its large resolution and FoV, it became the telescope's workhorse camera. It is configured as a two-channel instrument, the Ultraviolet-Visible (UVIS) channel (pixel scale of 0.04 arcsec/pix and FoV of 162 × 162 arcsec) and the Near-Infrared (NIR) one (pixel scale 0.13 arcsec/pix and a FoV of 136 × 123 arcsec)(Dressel,2023[20]).

COS performs high-sensitivity, medium- and low-resolution spectroscopy of astronomical objects in the UV range. It is characterized by two independent observing channels, a far-ultraviolet (FUV) detector and a near-ultraviolet (NUV) one (Soderblom, 2023 [70]).

STIS is a versatile imaging spectrograph, working from 1150 to 10300 Å and its capabilities are complementary to those of the COS (Medallon, 2023 [44]).

Hubble's three FGS are devices that lock onto guide stars and keep Hubble pointed in the correct direction. Two of the sensors point the telescope at an astronomical target and then hold that target in a scientific instrument's FoV. The third sensor is available to perform scientific observations, precisely measuring the distance between stars and their relative motions (Nelan, 2021 [50]).

Lastly, we can focus on the Advance Camera for Surveys (ACS), a third-generation instrument installed in March 2002 characterized by three independent channels that provide wide field, high resolution, and ultraviolet imaging capabilities respectively. These 3 channels are called: Wide Field Channel (WFC) [2002-present], High Resolution Channel (HRC) [2002-2007] and Solar Blind Channel (SBC) [2002-present].

The HRC was used for near-UV to near-IR imaging and coronagraphy and it is not operative anymore, while the SBC is still dedicated to far-UV imaging and spectroscopy.

The one that has been exploited for the data we analyzed is the first one, which employs a mosaic of two 4096x2048 Scientific Imaging Technologies (SITe) CCDs. The 15×15 μm^2 provide ~ 0.05 arcsec/pixel spatial resolution, resulting in a nominal 202 x 202 arcsec^2 FOV. The spectral sensitivity of the WFC ranges from 3500 Å to 11,000 Å, with a peak efficiency of 47 % at 6700 Å (Ryon, 2023 [66]).

The WFC shares 2 filter wheels with the HRC visible in a scheme shown in **Fig.2.11**. The desired filter in one filter wheel is rotated into position and a CLEAR aperture in the other filter wheel is automatically selected. The position of each filter is shown in **Fig.2.12** and the ones exploited in our analysis have been highlighted.
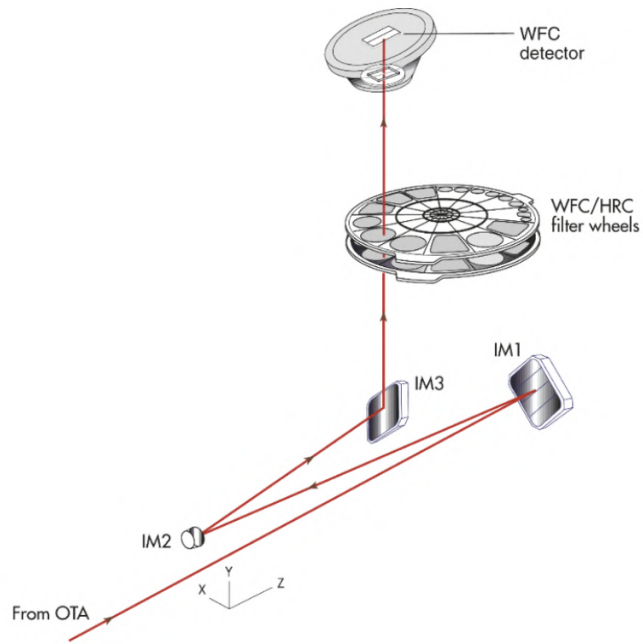
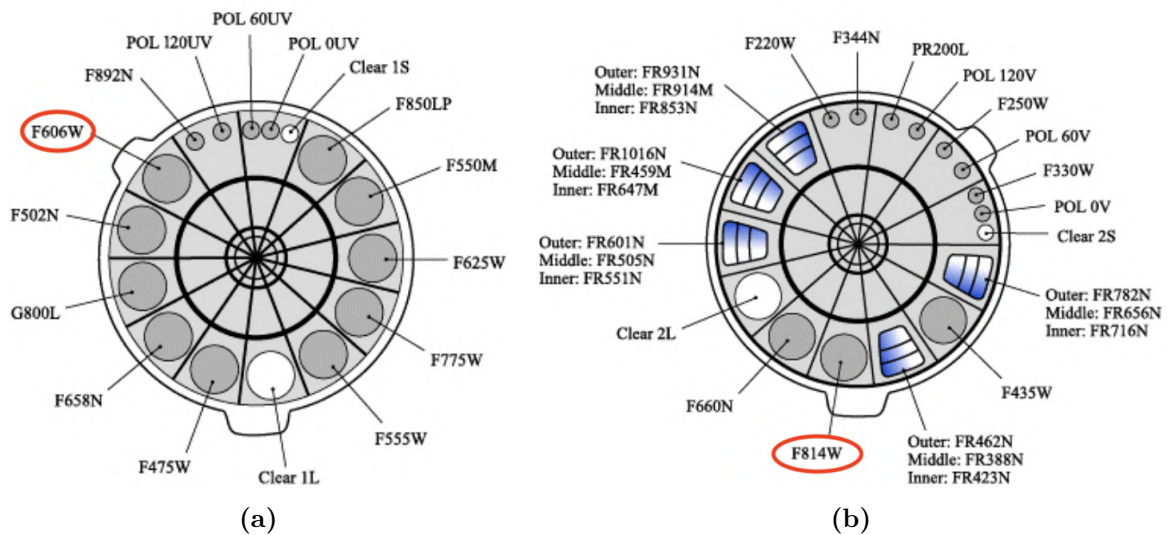**Figure 2.11:** WFC scheme (Ryon, 2023 [66]).

Figure 2.12: WFC and HRC filter wheels layout. The filters highlighted in red are the ones used for the analyzed data set (Ryon, 2023 [66]).

2.5 Data set

After an accurate description of the instruments exploited in the analysis, we can focus on the data set under study.

Due to the vicinity of the astrophysical object of interest, Terzan 6, to the Galactic Centre, as previously explained (**Sec.1.3.2**), the GC is heavily obscured with a mean extinction of $A_V \sim 7.3$ mag ($E(B-V) = 2.35$).

This is the reason why observations in the NIR are the ideal tool to properly explore the stellar populations in this cluster. Indeed the extinction coefficients at NIR wavelength (filter J and K) are significantly smaller than in the optical ($A_J = 2.0$ mag, $A_K = 0.8$ mag). Moreover, the superb capabilities of the MCAO-assisted GSAOI camera at the GEMINI South Telescope described above offer the ideal instrument to secure these observations.

These observations combined with HST images in the optical filters (F606W, F814W) secured several years ago will extend the wavelength range and provide the ideal time baseline to perform proper motion analysis.

The analyzed data set is composed of multi-epoch observations obtained with HST and GEMINI.

In particular, the first HST data set consists of a set of ACS/WFC images acquired on the 24th of July 2016 (Proposal ID. 14074 P.I Cohen). It is composed of 5 images for both the F606W and the F814W.

The second HST data set includes 5 ACS/WFC images acquired on the 11th of November 2021 (Proposal ID. 16420 P.I Homan) with the F606W band.

The first GEMINI data set includes a set of images that has been acquired from the 8th to the 12th of June 2013 (Program GS-2013A-Q23 P.I Geisler). It is composed of 26 images in the J filter and 27 images in the K_s filter.

The second data set, acquired from the 1st up to the 6th of August 2018 (Program GS-2018A-Q-231 P.I Cohen), is composed of 27 images in the J filter and 44 images in the K_s filter.

In the case of GEMINI, not all the images have been used for the scientific analysis, so they have been highlighted in the summary of the complete data set (**Tab 2.1**).

An example of the HST and GEMINI images we analyzed can be seen in **Fig.2.13**.

		HST		GEMINI			
	2016		2021	2013		2018	
	F606W	**F814W**	**F606W**	**J**	**K_s**	**J**	**K_s**
N. images	5	5	5	26	27	27	44
	4 (480s)	4 (473s)	4 (494s)	*23 (30s)*	*20 (30s)*	*25 (230s)*	*18 (45s)*
	1 (30s)	1 (30s)	1 (60s)	2 (10s)	5 (10s)	2 (15s)	*26 (30s)*
				1 (10.2s)	2 (10.9s)		

Table 2.1: Summary of the complete data set we exploited for the analysis with the total number of images per filter for the different epochs and the exposure times. The data in *italics* represents the GEMINI data exploited in the scientific analysis.
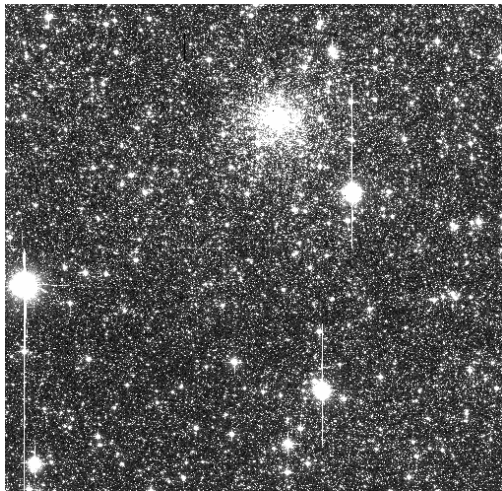
(a) *HST image obtained in F606W with an exposure time of 473s with a zoom in the cluster region.*
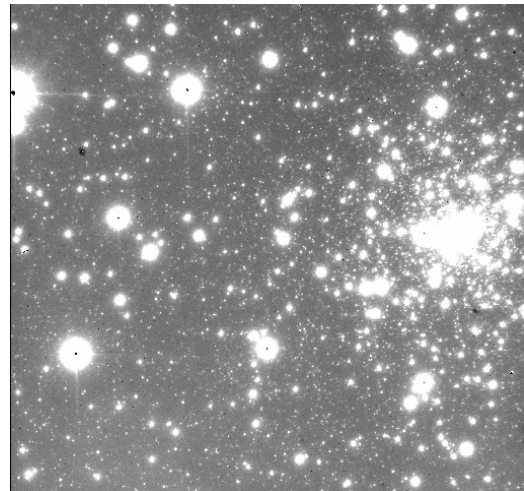
(b) *GEMINI image (2013) in the Ks filter with an exposure time of 30s.*

Figure 2.13: Examples of analyzed images.

Chapter 3

Data Analysis

The aim of this chapter is to provide a description of the photometric techniques adopted for the analysis of both the GEMINI and HST images.

In order to derive the magnitudes of the detected sources, here we adopt the so-called PSF-fitting technique, since this approach allows us to derive accurate measures of the source luminosities even in case of high level of crowding, as expected in the case of the central regions of a GC.

The procedure which has been used is slightly different in the 2 cases. For GEMINI, due to the large variability of the PSF according to the conditions of the observations in terms of the used asterism, weather and image correction quality in general, the analysis has been performed image by image.

3.1 PSF fitting

There are two main techniques to derive the magnitudes of stars by performing a photometric analysis: *aperture photometry* and *PSF fitting.*

The first one is normally used for isolated sources and it consists of summing the counts in a given area defined by the aperture radius, after the subtraction of the sky level in a given annulus, so that the magnitude is defined as

$$m = -2.5 log(\sum counts - Area \cdot sky)$$

The PSF fitting approach instead, estimates the source magnitudes from the integral of the detector counts under the analytical function that best reproduces the brightness profile of the point sources. In general, the procedure consists of 3 steps:

1. The search for the analytical function that best reproduces the brightness profile of the point source. This is usually done by considering single and bright stars, well distributed and not saturated;

2. The selection of all the sources in the FOV according to a chosen threshold level;

3. The fitting procedure, when the derived PSF model is adopted for all the selected sources.

The final output of this procedure is the "volume" of each source that represents an estimation of the detector counts generated by each source.

The magnitude of each source is computed as follows:

$$m = -2.5 log(Volume)$$

This approach is fundamental in the case of crowded regions like the central regions of globular clusters since it is possible to estimate the magnitude of faint sources even if they are close to brighter and/or saturated ones.

There are different analytic functions used to fit the brightness profile and the most common ones are:

- *Gaussian function*

$$g(x) = \frac{1}{\sigma\sqrt{2\pi}} exp(\frac{-(x-\mu)^2}{2\sigma^2})$$ (3.1)

  where μ is the expected value of the distribution and σ^2 the variance.

- *Moffat function* (Moffat, 1969[46])

$$m(r) = \frac{\beta - 1}{\pi\alpha^2}[1 + (\frac{r}{\alpha})^2]^{(-\beta)}$$ (3.2)

  where α has a similar meaning to μ in the Gaussian distribution and β is used to model the wings of the distribution (the most common ones are $\beta = 1.5$ and $\beta = 2.5$). If $\beta \to \infty$ the Moffat distribution approached the Gaussian one as seen in **Fig.3.1**.

- *Lorentz function*

$$L(x) = \frac{1}{\pi}\frac{\frac{1}{2}\Gamma}{(x - x0)^2 + (\frac{1}{2}\Gamma)^2}$$ (3.3)

  where x0 is the center of the distribution and Γ is related to the width of the distribution. We show here a comparison between the Gaussian and the Lorentzian function which appears less peaked in the central region and more extended in the wings (**Fig.3.2**).

- *Penny function*, which is characterized by a central Gaussian profile and a Moffat-like shape for the wings. It comes in 2 varieties, Penny1 and Penny2, according to whether the axes are aligned or not with the image ones.
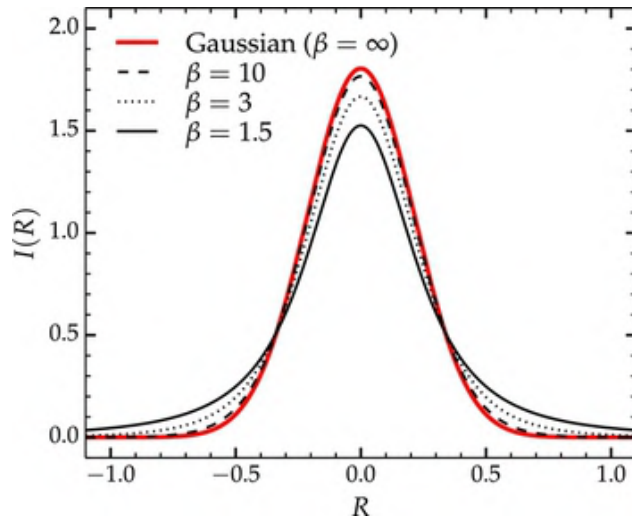
Figure 3.1: Comparison between a Gaussian ($\beta = \infty$) and Moffat functions with different β parameters (Ciambur, 2016 [12]).
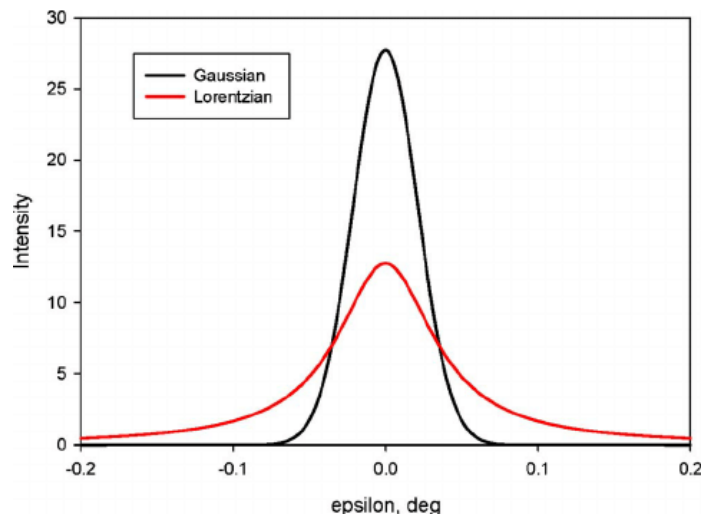

Figure 3.2: Comparison between a Gaussian and a Lorentz function (Kaduk, 2011 [35]).

3.2 Data Analysis: HST

The HST images analyzed here have been downloaded from the HST Archive. These images are already calibrated and corrected for the Charge Transfer Efficiency (CTE). The CTE effect is the decrease of the efficiency of the charge transfer due to the flux of energetic particles such as relativistic protons and electrons which damages the silicon lattice of the CCD detectors (the so-called 'hot' pixel) (Ryon, 2023[66]).

So the retrieved HST data are already processed by the Space Telescope Institute dedicated pipeline and are corrected for bias and flat-fielding effects. These effects are going to be better described in the **Section 3.3**, since for GEMINI the pre-reduction procedure has been entirely performed.

The analyzed dataset is composed of two different epochs: the first one was observed on the 24th of July 2016, while the second one on the 11th of November 2021.

3.2.1 Photometric Analysis

For the photometric analysis of the HST data, we used the publicly available software *img2xym* (Anderson, 2008[1]). Since HST is a space-based telescope and by definition diffraction-limited, the value of the FWHM is expected to be more or less constant for all the stars. So we used an equivalent PSF which has been already computed and that we could directly use to fit the brightness profiles.

To proceed with the PSF fitting procedure, we applied the PSF model (*img* command) by setting the minimum distance between 2 sources (4 pixels in our case) and the background value. We were also required to take into account the thermal gradient due to the relative position of HST and the sun ([PERT]).

In particular, we used a value of the background increased by 50% compared to the one obtained by evaluating the peak of the distribution of the counts as a function of the pixels number, in order to perform a sharper selection. This represents the threshold level for the procedure of source finding.

Among the different outputs, we focused on an ASCII catalog in which the xy coordinates have been corrected for 2 main effects:

1. the geometrical distortion due to the projection of the CCD plane onto the focal plane, which is not exactly perpendicular;

2. the variation in the magnitudes of any source in the FOV caused by the different effective areas each pixel is exposed to because of the same projection effects.

Then the following analysis was performed independently for long exposures (4 images in the F606W filter with an exposure time of 480s and 4 images in the F814W with an exposure

time of 473s for the 2016 epoch, while 4 images in the F606W with an exposure time of 494s for the 2021 epoch) and short exposures images (1 image in both F606W and F814W with an exposure time of 30s for the 2016 epoch, while 1 image in the F606W with an exposure time of 60s for the 2021 epoch).

First of all, we should cross-correlate the different long exposures images in order to report them to a common coordinate reference frame since during the observations the pointing can change.

The exploited software ($CataXcorr$[1], Montegriffo 1995[47]) identifies the common objects between the images and a reference one (at least 3 since we are performing a roto-translation) by considering both the coordinates and the magnitudes, then it determines the geometrical transformation to apply. In this case, we chose one of the long-exposure images as a reference. Then we proceeded with the evaluation of the mean magnitude difference between common stars in order to re-scale the images to the reference one by using $CataComb$[2], but in this case the magnitude shifts were so small (of the order of ≈ 0) that they could be neglected. So we could directly cross-correlate the long exposure and short exposure results to obtain the final catalog, after the correction for the magnitude shifts.

This procedure has been applied to both HST epochs.

Finally, we combined the 2 catalogs we obtained for the 2 different HST epochs.

3.2.2 Astrometry and Calibration

In the final catalog, it was necessary to report the instrumental coordinates to an absolute reference frame (α and δ) and to perform a photometric calibration on the magnitudes.

The astrometric transformation of the catalog has been performed by using the stars in common with the publicly available ESA/Gaia catalog as the astrometric reference frame. Geometric transformations were computed and applied to the HST catalog.

More precisely, we exploited also the capability of the SExtractor software[3] (Bertin, 1996 [7]) in order to read instrumental and absolute coordinates from a reference image.

The photometric calibration has been performed by reporting the magnitudes to the Vega photometric system[4]:

$$m_{cal} = m_{instr} + zero \quad point + aperture \quad correction \tag{3.4}$$

---

[1]It is a Cata program developed in 2002 by P. Montegriffo (Astronomical Observatory, Bologna) particularly useful for astrophysical analysis.

[2]It is a Cata program used to obtain catalogs with information of different sources from different lists analyzed with CataXcorr.

[3]SExtractor is a program that builds a catalog of objects from an astronomical image and it is extremely useful both for large-scale galaxy-survey data and stellar field.

[4]The Vega system or Johnson system of magnitude sets the zero point for a magnitude scale, taking the magnitude of the star Vega as zero.
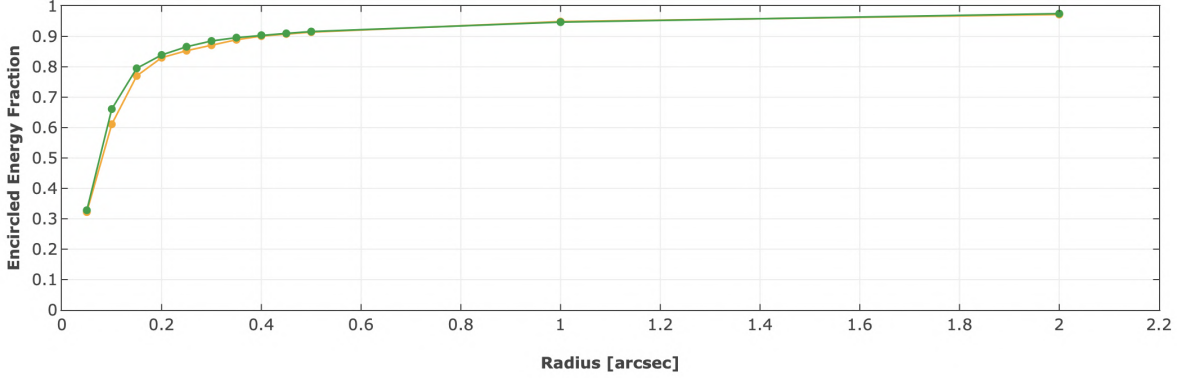
Figure 3.3: ACS/WFC encircled energy curves, where the green line represents the F606W while the orange one is the F814W (Space Telescope Science Institute [74]).

where $m_{instr} = -2.5log(Flux/t)$, where the flux is the magnitude of the final catalog and t is the exposure time of the reference image per filter.

To find the zero points we used the ACS Zeropoint Calculator[73] available online, by considering the filter, the detector and the date of the observation; while for the aperture correction, we considered the encircled energy plots available on the Space Telescope Science Institute (STScI) website[74]. The encircled energy values are used to compute the aperture corrections required to account for flux falling outside an aperture of radius R (**Fig.3.3**).

In particular, we considered the encircled energy fraction at 2 different radii: 0.2" (since the zero points we used in the photometric calibration are defined according to this aperture, corresponding to 4 pixels) and ∞.

The first one is the amount of flux lost because of the errors in the fit of the brightness profile of the star, i.e. the flux lost from the brightness peak to 0.2"; while the second one is the amount of flux lost since the volume integral of the stellar source is radially limited but the wings of the PSF are more extended. So the aperture correction is the difference between the value at infinity and at 0.2".

For the first epoch, the zero points were 26.398 (F606W) and 25.503 (F814W), while for the second epoch 26.402 (F606W); the aperture corrections were 0.136 (F606W) and 0.142 (F814W).

At this point, the final catalog is composed of the calibrated magnitudes with photometric errors and flag, instrumental and absolute coordinates.

A preliminary version of CMD obtained from the analyzed HST data set is shown in **Fig.3.4**, in which the different evolutionary sequences are evident. In particular, we can already notice a well-extended and populated RGB, with the RGB bump at around $m_{F814W} \approx 19$. Also, the RC is visible around $m_{F814W} \approx 18.5$ but still elongated due to the presence of differential reddening.

The photometric sample extends down to $m_{F814W} \approx 24$ roughly 3 magnitudes below the
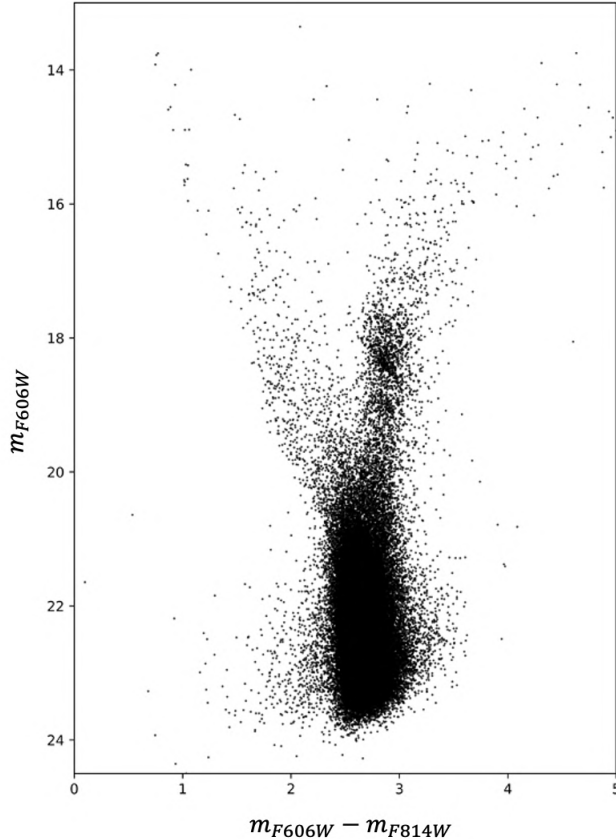
Figure 3.4: Preliminary HST ($m_{F606W} - m_{F814W}$,m_{F814W}) CMD.

MS-TO which is approximately located at $m_{F814W} \approx 21$, but the MS is still largely contaminated by galactic field interlopers making the identification of the MS-TO more challenging. This is why a differential reddening correction and a proper motions selection, in order to determine the cluster membership, is needed. This will be better explained in **Chapter 4**.

3.3 Data Analysis: GEMINI

Before starting with the photometric analysis of the GEMINI data set, it was necessary to perform a pre-reduction procedure, which consists of bias and flat-field correction, and sky subtraction.

3.3.1 Pre-reduction

As described in **Sec. 2.3**, the GSAOI camera is composed of 4 different chips, so the analysis of the GEMINI data set has been performed independently on each of them. It was necessary to extract each of the individual chips by using the task *fitsutil/fxsplit* of IRAF[5].

---

[5]The Image Reduction and Analysis Facility is a general purpose software system for the reduction and analysis of astronomical data written by the National Optical Astronomy Observatories (NOAO) in Tucson,

Detector	Read noise [ADU]				Gain [e-/ADU]
	$FS1-1$	FS 4-4	FS 8-8	$FS16-16$	
1	11.6	5.6	4.2	3.2	2.434
2	9.5	4.9	3.7	2.9	2.010
3	11.2	5.9	4.4	3.3	2.411
4	12.4	6.3	4.8	3.7	2.664

Figure 3.5: Readout noise and gain values according to the different Fowler sampling, in case of our dataset the 1-1 sampling has been adopted (Carrasco, 2012 [10]).

The output of this task is 4 different files for each input provided.

Starting from the **SKY-SUBTRACTION**, the adopted observational strategy requires that we estimate the unresolved background by combining the target scientific images. This procedure is characterized by some disadvantages, like the problems related to the large crowding in the central region. Anyway, the results that we got were good enough also for the central region.

The first step was to combine all the scientific images in a MASTER SKY after setting the value of the READOUT NOISE and the GAIN according to the GEMINI Observatory website[53]. The adopted values were different according to the different chips used (**Fig.3.5**).

The different images were combined using the median value. It means that this was the operation performed by the software (IRAF task *imcombine*) on all the pixels after a rejection procedure done by considering a sigma clipping (1σ) exclusion criteria.

Then we proceeded with the **FLAT-FIELD** correction since the response/sensitivity of a detector is not uniform but it varies from pixel to pixel.

In this case, we considered both FLAT-ON and FLAT-OFF images, which are images obtained with a closed and uniformly illuminated dome or on the sky, respectively.

We combined (IRAF task *flatcombine*) 35 images for the J filter and 40 images for the K_s filter for the 2013 dataset, while 15 images for the J filter and 30 images for the K_s filter for the 2018 dataset by assuming again the median value as combining operation, but different exclusion criteria: the n-high and n-low pixels. Generally, it means that a specific fraction of the highest and lowest pixels in the images are rejected and it is specified by the factor n. For each filter, we normalized the combined images by the mean value of the difference <FLAT ON - FLAT OFF> by exploiting the *imarith* task IRAF.

In the end, we applied the corrections by using the task *ccdproc* for each filter and chip:

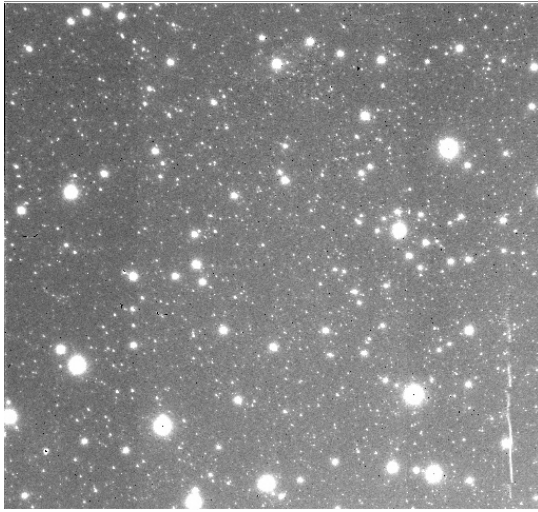$$I_{SCIENCE} = \frac{I_{RAW} - SKY}{(FLAT\ \ ON - FLAT\ \ OFF)_{norm}} \tag{3.5}$$

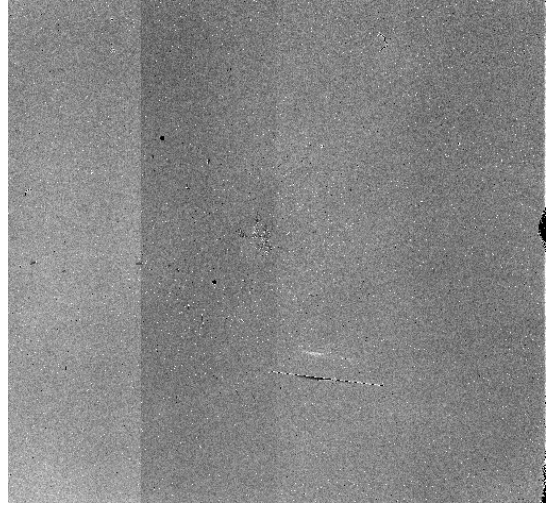where $(FLAT\ \ ON - FLAT\ \ OFF)_{norm}$ is the normalized difference between FLAT ON and FLAT OFF.

The images can be then used for a 'scientific analysis'.

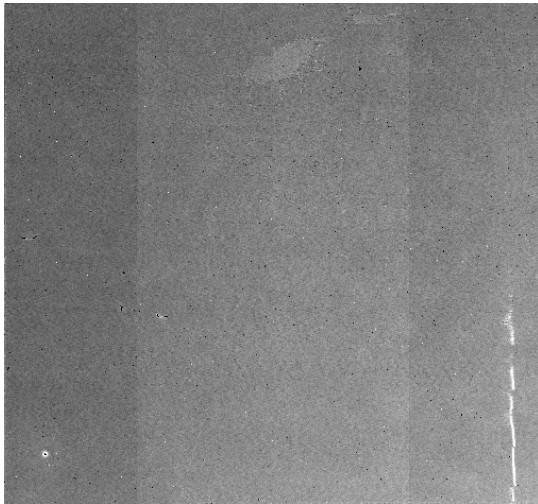
Arizona.

We show here some images to summarize the main element and results of the pre-reduction procedure (**Fig.3.6**).

(a) *Example of a raw image (K_s filter, chip 3, 2013 epoch).*

(b) *Example of a DOMEFLAT image (K_s filter, chip 3, 2013 epoch).*

(c) *Example of a MASTER SKY image (K_s filter, chip 3, 2013 epoch).*
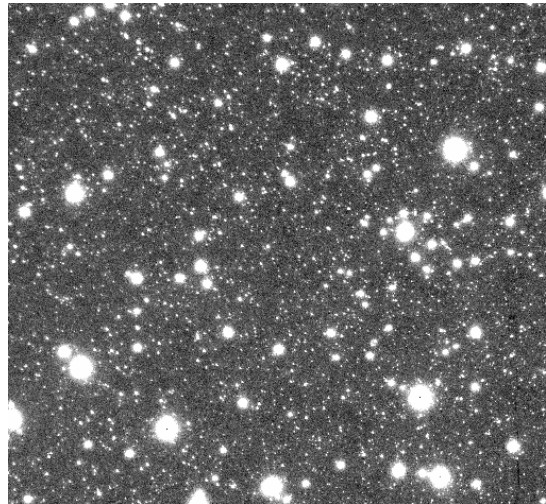
(d) *Example of the result of the pre-reduction procedure (K_s filter, chip3, 2013 epoch).*

Figure 3.6: Pre-reduction elements and results.

3.3.2 Photometric analysis

The photometric analysis was performed for each chip independently by using the software *DAOPHOT II*[6] (Stetson, 2011 [71]).

Before running the PSF analysis, we constrained the quality of the images delivered by the AO system by estimating the mean FWHM and its variation within each chip.

---

[6]DAOPHOT is a package for stellar photometry designed to deal with crowded fields. It was written by Peter Stetson at the Dominion Astrophysical Observatory.

It was important to derive for each image a first guess on the FHWM by considering tens of bright, single and not saturated stars by exploiting the IRAF task *DAOEDIT*. This is an interactive way to visualize the radial and the brightness profile of the chosen star in order to verify if it is a good candidate for an estimation of the FWHM. Then it provides as output the FWHM in pixels for each chosen star so that the mean FWHM value for each image can be evaluated.

The PSF fitting analysis was performed only on the images having a reasonable FWHM which are: 13 images for the K_s filter and 18 images for the J filter (2013 dataset), while 17 images for the K_s filter (only 45s ones) and 24 images for the J filter of the 2018 dataset.

As a first step, we searched for possible sources in the FOV whose brightness peak was above a defined threshold (see below) by using DAOPHOT/FIND which evaluated the approximated position of all the considered stars.

Then, starting from the obtained catalog, aperture photometry was performed (DAOPHOT II-*PHOTOMETRY*) on an aperture of 3 pixels in radius. The aperture magnitude was only used to provide a relative ranking of stars for the PSF modeling procedure.

Then the best-fit model for the PSF and its possible spatial variation within the FOV was obtained by using the task DAOPHOT/*PSF*. A large number of relatively bright (but not saturated stars) homogeneously distributed within the FOV were selected by means of an iterative procedure. The resulting list of selected stars was then provided to DAOPHOT/*PSF*, which selected the best PSF models (among those available) and best-fit parameters according to a χ^2 test.

The parameters needed for this part of the analysis were organized in .opt files:

- **Readout noise** and **Gain**. They are different according to the different chips analyzed as shown in **Fig. 3.5**.

- **Saturation level** which was set to 45000 ADU, smaller than the nominal one (50000 ADU), in the PSF modeling procedure.

- **Threshold** represents the number of counts in sigma compared to the background level above which the software starts to identify the sources. At the beginning, the level was set to 6 sigma in order to detect only bright sources to model the PSF in the best possible way.

- **PSF radius**, so the radius (in pixel) within which the FWHM can be evaluated. The value was set to 20 pixels.

- **Inner Sky radius** and **Outer Sky radius** which are the inner and outer radius of the annulus used to evaluate the background level. In our case, the values were set to 15 and 25 pixels respectively.

- **Analytic** which defines how many analytic PSF models the software can test on the sources. We set -6 in order to allow the DAOPHOT II task *PSF* to try to fit all the available models.

- **Varia** which indicates the allowed spatial variability degree of the PSF. During the first part of the analysis, the PSF modeling, this parameter was set $= 1$, so it means that we allowed the PSF to linearly vary in the FOV; then it was set $= 3$, which means that the allowed variability was a cubic one.

- **FWHM** which was set according to the value obtained in the *DAOEDIT* task.

- **Fitting Radius** defines the radius in pixel inside which it is possible to define the PSF, usually it is set as 2 times the FWHM. Anyway in the case of some images characterized by a larger FWHM, the fitting radius was set equal to the FWHM.

At the end of this procedure, the best-fit models were a *Lorentz* function with 3 free parameters for both the K_s filter of the 2018 dataset and the J filter of the 2013 dataset, a *Moffat* function with a β parameter $=1.5$ for the J filter of 2018 and a *Penny1* with 4 free parameters for the K_s filter of 2013 dataset.

The following step consists of the derivation of the magnitudes of the stars utilizing the PSF-fitting procedure and this is done by running DAOPHOT/*ALLSTAR* on all stars brighter than 4σ from the local background. We also assumed the saturation level to be the nominal one for the instrument.

At this point, for each image, we had a list with instrumental coordinates, magnitudes and relative errors for all detected stars. Residual images were also provided in order to check if the application of the PSF model on the sources was successful (**Fig.3.7**). It can be noticed that all the non-saturated stars have been identified and removed by the procedure, while the residuals represent the saturated ones.

Finally, we combined all the different images based on the coordinates of the stars in common among the different catalogs by using *DAOMATCH*.

The derived geometrical transformations among the images were stored in a dedicated (.mch) file.

Then we finally combined all the images for each chip by using *DAOMASTER* in order to generate a catalog .mag in which to each star the mean of the magnitudes derived in the different images and the standard deviation were computed as reference image and error, respectively. In this step, it was important to decide the number of frames in which the considered star must be in order to be included in the catalog and this was particularly important to avoid fake detection. As a general criterion, we included stars detected in half of the images (per chip and filter) + 1.

The last step of the photometric analysis was the *ALLFRAME* (Stetson, 1994 [72]) routine,
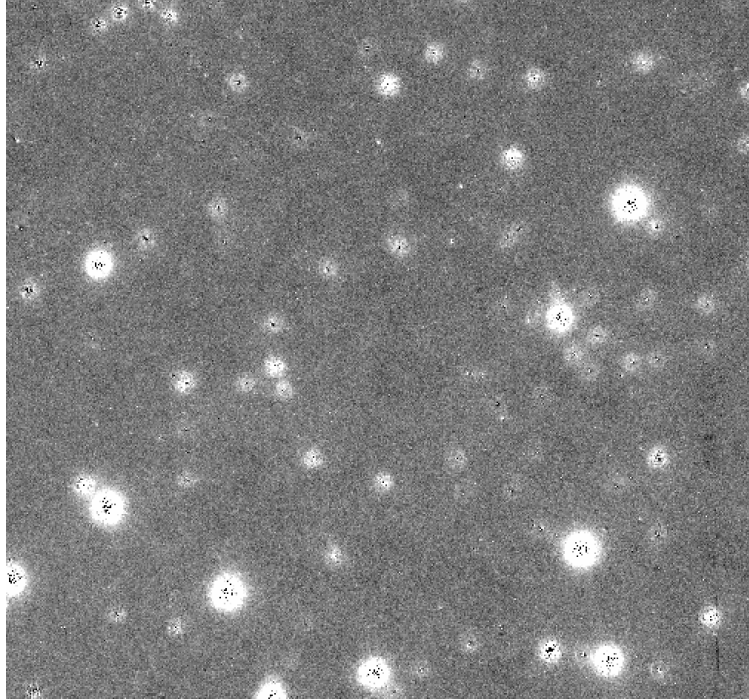
Figure 3.7: Example of a residual image after the PSF fitting.

which makes simultaneous use of the geometric and photometric information from all images of a given field to derive a self-consistent set of positions and magnitudes for all detected star-like objects in that area of sky, thereby extending the range of magnitude and crowding conditions for which useful photometry is obtainable. It exploits a combination of analytic functions and numerical residuals to estimate the magnitudes of all the star-like objects.

It can increase the accuracy in the determination of the centroids of all the stars, improving the precision in the determination of the magnitudes.

The input was the previously generated .mag files, in particular, we considered the K_s filter as a reference since it was much deeper than the J one and the result obtained from the *DAOMATCH* procedure by combining all the images for each chip. Then it was possible to derive a final catalog asking for all the stars present in both .mch files for the J and K_s filters for each chip.

The information shown in the final catalog is the ID, instrumental coordinates xy and magnitudes with the associated errors, together with the mean χ^2 value[7] and sharpness[8], fundamental to understand if the analyzed sources are actually stellar objects.

---

[7]It is a measure of the difference between the observed and expected frequencies of the outcomes of a set of events or variables and it is defined as the sum of the quadratic difference between the observed data and the model, divided by the square of the associated error.

[8]It is a statistical parameter used to test the real nature of the source and it is defined as the quadratic difference between the FWHM of the stellar object and the one of the model.

3.3.3 Astrometry and Calibration

As in the case of HST, in the final catalog generated in the previous step of the photometric analysis, the xy coordinates and magnitudes were the instrumental ones that should be reported to the absolute coordinate and magnitude scales.

For the 2013 dataset, the astrometric correction was performed by cross-correlating the final catalog of each chip with the previously generated HST catalog, after exploiting again SExtractor; then the photometric calibration by matching the final catalogs with the publicly available NIR catalog obtained with the SOFI imager mounted at the ESO/NTT telescope. Finally, to perform the astrometric and photometric calibration for the 2018 epoch we used the GEMINI 2013-HST combined catalogue. In **Fig.3.8** we have reported examples of the (J-K_s, K_s) CMD which have been obtained for both epochs after that a sharpness selection (sharpness>-0.2 & sharpness<0.2) has been performed to reduce the 'noise' in the fainter part of the MS.
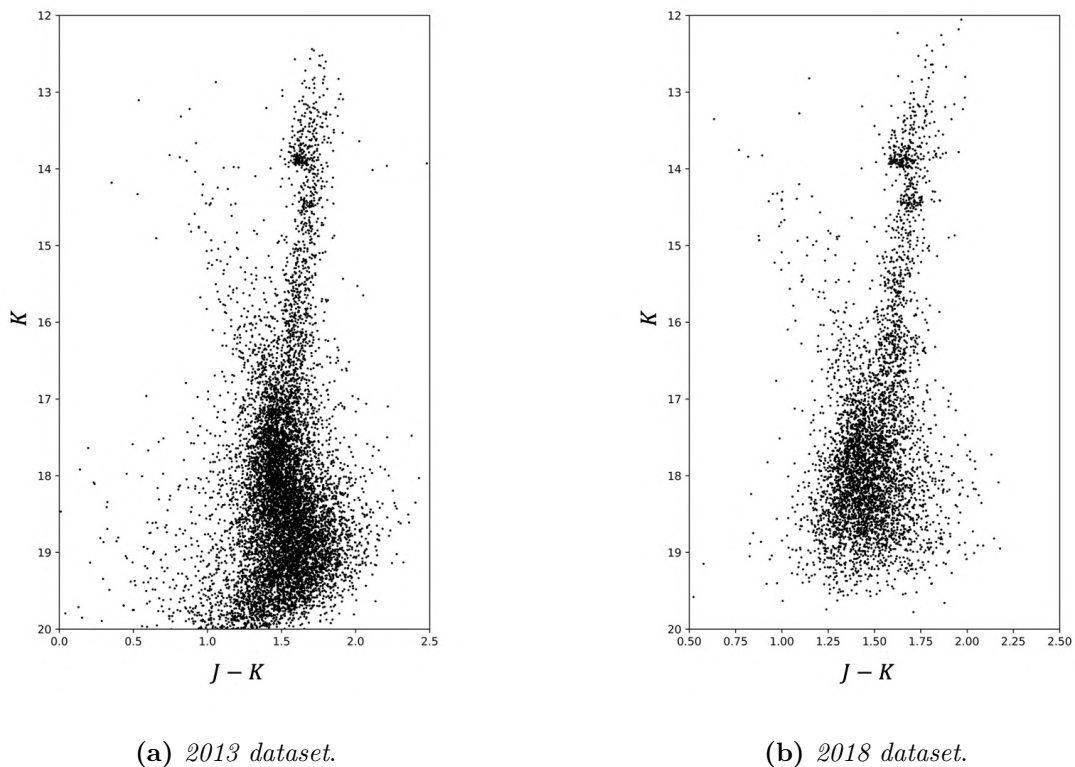

(a) *2013 dataset.* (b) *2018 dataset.*

Figure 3.8: (J-K_s, K_s) CMD not corrected for differential reddening nor proper motions selected.
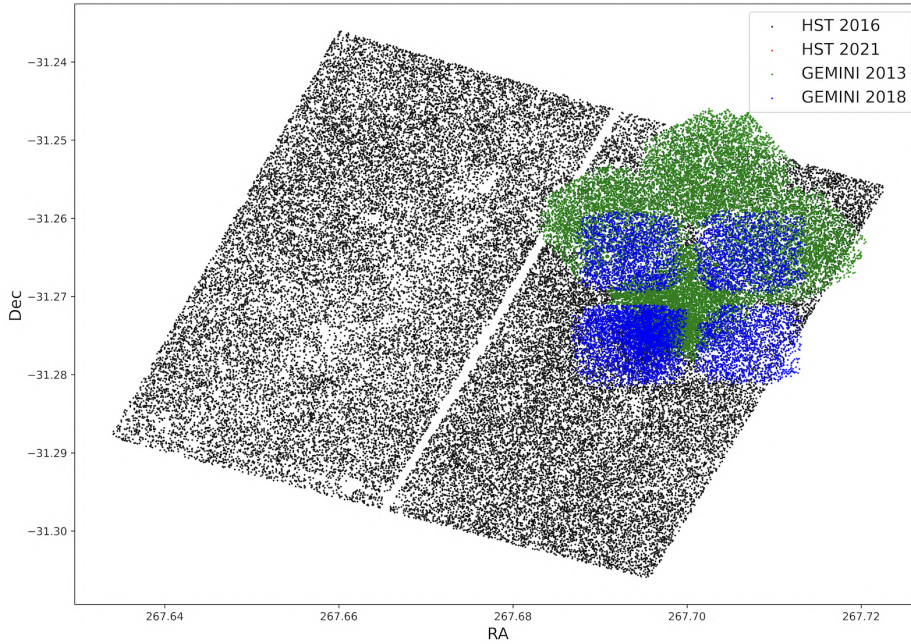
Figure 3.9: Spatial distribution of the different data sets by considering the stars included in the final catalog. The different data sets are represented by using different colors.

3.4 Final catalogue

The final result of this photometric analysis is a catalog in which the first epoch of HST was used as a reference and it was obtained by performing a series of cross-correlations between the previously generated catalogs. In the last cross-correlation (the one between the HST-GEMINI 2013 catalog and the GEMINI 2018 one) it was also necessary to correct for some magnitude J and K_s shifts between the 2 GEMINI epochs.

The final catalog contains the absolute coordinates, the δx and δy (the difference in xy instrumental coordinates between the 2 HST epochs, useful for the proper motions analysis), the magnitudes in the F606W, F814W, K_s, J bands with the relative errors (and flags, in case of the F606W, F814W bands), sharpness and χ^2 (in case of the K_s, J bands), the ID of the different epochs.

The spatial distribution of the stars considered in the final catalog is shown in **Fig.3.9**.

We show here an example of a $(m_{F814W}-K_s, K_s)$ CMD for both epochs in **Fig.3.10**. A more detailed analysis of the CMD evolutionary features will be provided after the proper motions selection and differential reddening correction (**Chapter 4**).
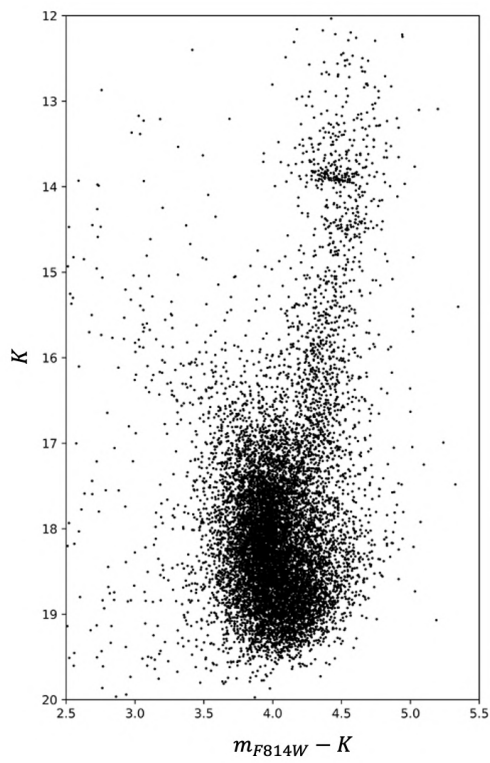
(a) *2013 dataset.*
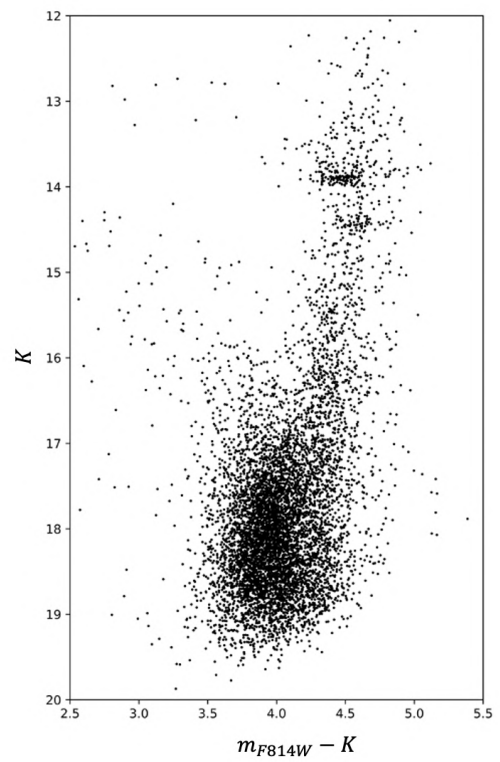
(b) *2018 dataset.*

Figure 3.10: $(m_{F814W}\text{-}K_s, K_s)$ CMD not corrected for differential reddening nor proper motions selected.

Chapter 4

Proper motions analysis and differential reddening

This chapter aims to provide a detailed description of the relative proper motions estimate and the differential reddening correction. These corrections are fundamental in the case of Terzan 6 (and Bulge Globular Clusters in general) due to its location in a region strongly affected by contamination from field stars and highly variable extinction.

4.1 Proper motions analysis

The proper motion (PM) is the angular change in the position of a star across the line of sight of an observer and it is generally measured by securing observations of the same scientific target several years apart and measuring the variation of the position of stars with respect to distant background sources (typically galaxies).

In the past years, accurate astrometric information has been provided by the ESA Gaia mission for over 1 billion stars in the Galaxy. Nevertheless, because of its distance and strong extinction, Terzan 6 stars are mostly out of reach with Gaia and proper motions are available for only a handful of stars located in the periphery of the system. This is not adequate to disentangle between cluster members and field interlopers along the evolutionary sequences sampled by our photometric analysis.

For this reason, we estimated relative proper motions to decontaminate the observed CMD from field stars, by exploiting the large temporal baseline sampled by the adopted dataset ($\Delta t \approx 8.41$ yrs) by following the approach of Dalessandro, 2013[16].

We used the two HST epochs, as for these images it can be easier to derive accurate stellar centroids than with GeMS/GSAOI data. In addition, the ACS/WFC has a larger field of view than GSAOI, thus ensuring that the analysis samples a larger portion of the cluster.

The procedure consists of determining the displacement of the centroids of the stars measured in the two epochs once a common coordinate reference frame is defined.

The first step is to adopt a distortion-free reference frame, hereafter "master frame". The master-frame catalog contains stars measured in all the ACS/WFC F814W-band single exposures of the first (older) epoch. Their coordinates were corrected for geometric distortions as described in **Sec. 3.2.1**.

To derive accurate transformations between the second-epoch catalog and the master catalog, we selected a sample of 1379 bona fide stars having instrumental magnitude $m_{F814W} < -11$ and $1.77 < (m_{F606W} - m_{F814W}) < 2.5$, which we judged to be likely cluster members based on their position in the CMD (i.e., stars distributed along the RGB, red-clump and AGB sequences - **Fig.4.1**).

The mean position of a single star in each epoch (x_m, y_m) has been measured as the 3σ-

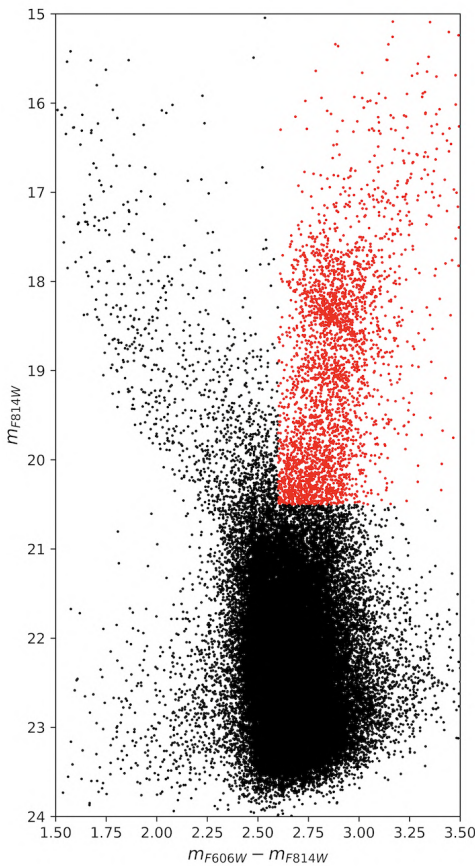**Figure 4.1:** Example of RGB stars selected as astrometric reference system in the analysis of the proper motions. This example of selection has been performed after the photometric calibration of the HST catalog.

clipped mean position calculated from all the N individual single-frame measurements. The relative rms of the position residuals around the mean value divided by N has been used as the associated error (σ).

Finally, the displacements are obtained as the difference of the positions (x_m, y_m) between the two epochs for all the stars in common. The error associated with the displacement is the combination of the errors on the positions of the two epochs.

We should stress here that the first epoch is by construction in the same coordinate reference frame as the master catalog.

The relative PMs (μx, μy) are finally determined by measuring the difference of the mean x and y positions of the same stars in the two epochs, divided by their temporal baseline Δt. Such displacements are in units of pixels yr^{-1}.

We then iterated this procedure a few times by removing likely non-member stars from the master reference frame based on the preliminary PMs obtained in the previous iterations. The convergence is assumed when the number of reference stars that undergo this selection changes by less than $\approx 10\%$ between two subsequent steps.

In the end, we derived relative PMs for 32515 stars in the area where the two HST datasets overlap.

To build a clean sample of stars with a high membership probability, we defined the so-called vector-point-diagram (VPD) for 5 magnitude bins with a width of 1.5 mag each.

The right panels of **Fig.4.2** show the derived VPDs at different magnitude levels. As expected, the PM distributions get broader for increasing magnitudes because of the increasing uncertainties of the centroid positions of faint stars.

By definition in each magnitude bin, cluster stars are expected to be distributed around position (0,0). Around this value, we defined fiducial regions as those including stars within 3σ, where σ is the average PM error in that magnitude bin.

The sample of stars thus selected represents the "member stars" sample which is analyzed in the following sections and after the differential reddening correction will provide the characterization of the stellar populations belonging to the cluster.

The CMD of the "member stars" sample is shown in **Fig.4.2(b)**. For comparison in **4.2(c)** we plot the CMD of the likely field stars that have been excluded from the analysis. Note that because of the partial overlap between the motion of Terzan 6 and that of bulge and disk stellar populations in this region of the galaxy, a possible residual contamination also is expected in the PM-cleaned CMDs.

4.2 Interstellar absorption

Because of its position in the Bulge of the Galaxy, at only about 1 kpc from the Galactic center, one of the most severe challenges in the observation of Terzan 6 is the huge interstellar absorption along the line of sight.

The main effect of the interstellar absorption is the so-called **reddening**, which is a shift of the electromagnetic radiation wavelength toward redder values while traveling through the
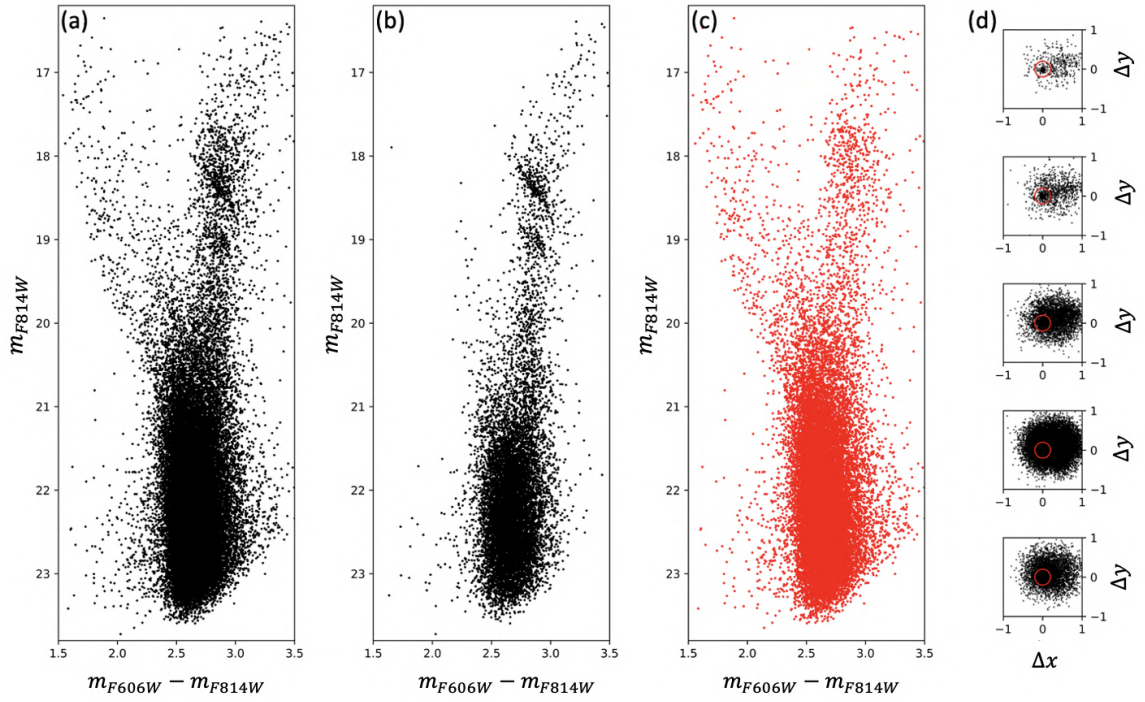
Figure 4.2: Example of a proper motion analysis performed on a $(m_{F606W}\text{-}m_{F814W}, m_{F814W})$ CMD: **(a)** Original CMD with all the stars in common between the HST epochs (2016, 2021), **(b)** PM selected CMD, **(c)** CMD of the likely field stars interlopers which have been removed according to the analysis of the proper motions, **(d)** VPD at different magnitudes bins.

interstellar medium (ISM).

The wavelengths which are more affected by this phenomenon are the shortest ones. They can be easily absorbed by the ISM dust grains during their traveling and then re-emitted in the IR band or they can be scattered to longer wavelengths because of collision with the dust grains themselves.

In order to describe the extinction process it is important to start from the radiative transfer equation in the most simplified form, meaning considering just radiation that is being absorbed from the ISM, neglecting emission processes. In this case

$$dI_\lambda = -\alpha_\lambda I_\lambda ds \tag{4.1}$$

where I_λ is the intensity of a considered bright source at a given wavelength λ, α_λ is the absorption coefficient of the medium (cm^{-1}) and ds the distance traveled by the light in the medium.

By integrating **Eq.4.1** we get

$$I_\lambda = I_{0\lambda}e^{-\tau_\lambda} \tag{4.2}$$

where $I_{0\lambda}$ is the 'original' intensity and τ_λ is the so-called *optical depth* defined as

$$\tau_\lambda = \int_0^s \alpha_\lambda ds \tag{4.3}$$

assuming the radiation to be produced at s=0.

We can describe the extinction phenomenon by defining the extinction parameter A_λ as

$$A_\lambda = -2.5 log(\frac{I_\lambda}{I_{\lambda_0}}) \tag{4.4}$$

which is related to the optical depth as

$$A_\lambda = 1.086 \tau_\lambda \tag{4.5}$$

Thus, the intrinsic observed magnitude is defined as

$$m_{0\lambda} = m_\lambda - A_\lambda \tag{4.6}$$

where m_λ is the observed magnitude affected by extinction. It is important to parametrize the extinction in the most precise way to obtain accurate intrinsic magnitude values.

The interstellar extinction variation with wavelength is known as the *interstellar extinction law* or *interstellar extinction curve* and it is most commonly determined using the "pair method" which compares the spectrum of a reddened star with that of an un-reddened star of the same spectral type (Li, 2015[41]). This method can be used to determine the Galactic extinction curve or the extragalactic one, but only for the Local Group galaxies since it is necessary to have resolved stars.
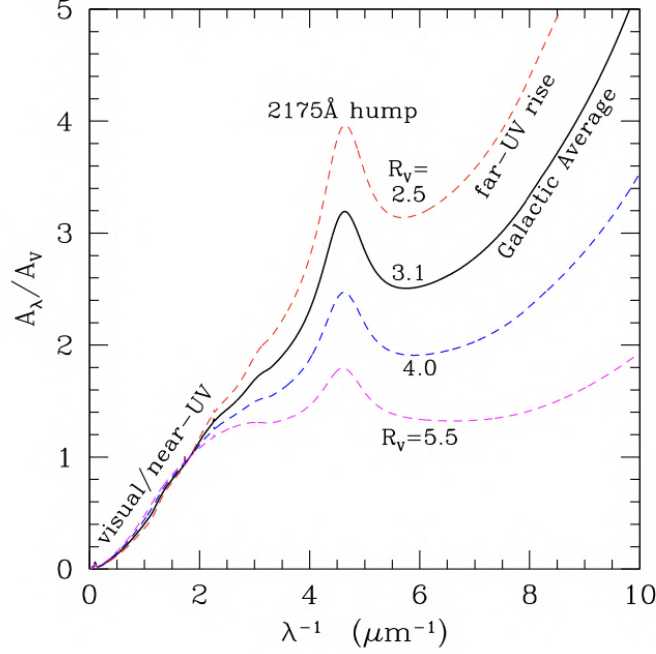
Figure 4.3: Different Galactic extinction curves according to the different grain sizes distribution along the line of sight (Li, 2015[41]).

A few examples of Galactic extinction curves are shown in **Fig.4.3**. They depend on different values of the empirical R_λ parameter, which in turn depends on the properties of the ISM, for example, the average grain dimension.

In order to properly define this parameter is important to introduce another way in which the reddening phenomenon can be described: the color excess. It is used to describe the difference between the intrinsic color and the observed one.

By considering the magnitude of a source in two different bands (ex. B, V) as

$$B_0 = B_{obs} - A_B \tag{4.7}$$

$$V_0 = V_{obs} - A_V \tag{4.8}$$

$$\rightarrow (B - V)_0 = (B - V)_{obs} - E(B - V) \tag{4.9}$$

where the quantities with 0 are the intrinsic ones and E(B-V) represents the color excess. So starting from the color excess there is a relation with the extinction coefficient:

$$A_\lambda = R_\lambda E(B - V) \tag{4.10}$$

The R_λ is different for each band. For example the coefficients used in this project are $R_{F606W} = R_V \times 0.9 = 3.12 \times 0.9 = 2.81$, $R_{F814W} = 1.87$, $R_J = 0.87$, $R_{K_s} = 0.35$.

4.2.1   Differential reddening

The interstellar extinction along the Galactic plane and in the direction of the Galactic center can be highly spatially variable on scales that can be as small as a few arcseconds

(Pallanca, 2021 [58]), as a result of the presence of clouds with different column densities along the line of sight.

The main effect on the CMD is an elongation of the main evolutionary features along the direction of the reddening vector[1]. Such an effect is commonly referred to as **differential reddening**.

It is therefore important to correct for these effects for Terzan 6.

The method that has been adopted is the so-called *star by star* approach, which consists of the estimation of the reddening of individual stars by evaluating the displacement from a mean ridge line. We adopted the procedure described in Dalessandro et al., 2018 [17] and properly adapted it to the dataset used for this Thesis.

We used likely member stars (based on the proper motion analysis described in **Section 4.1**) located in the RGB, SGB and the brightest part of the MS in the $(m_{F606W} - m_{F814W}, m_{F814W})$ as the reference population. Then we computed the mean ridge line of these stars.

The adopted procedure can be schematically summarized as follows.

- First of all, starting from the mean ridge line we selected stars enclosed within 3 times the average color error in the considered magnitude range. Magnitude selection was performed by following the slope of the reddening vector $(R_V - R_I = 1.25)$. The 2890 stars selected are shown in **Fig.4.4**.

- For each of the selected star, the distance $\Delta(m_{F606W} - m_{F814W})$ from the mean ridge line was computed. The distribution is shown in **Fig.4.5** in which the mean ridge line is located at $\Delta(m_{F606W} - m_{F814W}) = 0$.

- For each star of the original catalog we evaluated the $\Delta(m_{F606W} - m_{F814W})$ as the mean of the values of the 20 nearest (in the plane of the sky) reference stars. This number of neighboring stars was found to be the best compromise in this project.
  In **Fig.4.6** we show an example of the 20 closest stars with respect to the i_{th} considered star (in red) of the original catalog.

- Finally the differential reddening $\delta E(B - V)$ is found by applying:

$$\delta E(B - V) = \frac{\Delta(m_{F606W} - m_{F814W})}{\sqrt{2R_{F606W}^2 + R_{F814W}^2 - 2R_{F606W}R_{F814W}}} \qquad (4.11)$$

  We assumed $R_{F814W} = 1.884$, $R_{F606W} = 2.874$ (Casagrande, 2014 [11]).

The result of the reddening distribution within the HST field of view is shown in **Fig.4.7** in which the blue/purple regions are the ones with the smallest reddening values, while the yellowish ones are the most extinct. An overall variation $\delta E(B - V) \approx 0.1$ is observed.

Once we estimated the differential reddening values, we applied the results to each star of

---

[1]It is the vector whose slope is given by the ratio of the color excesses of any color-color pairs.
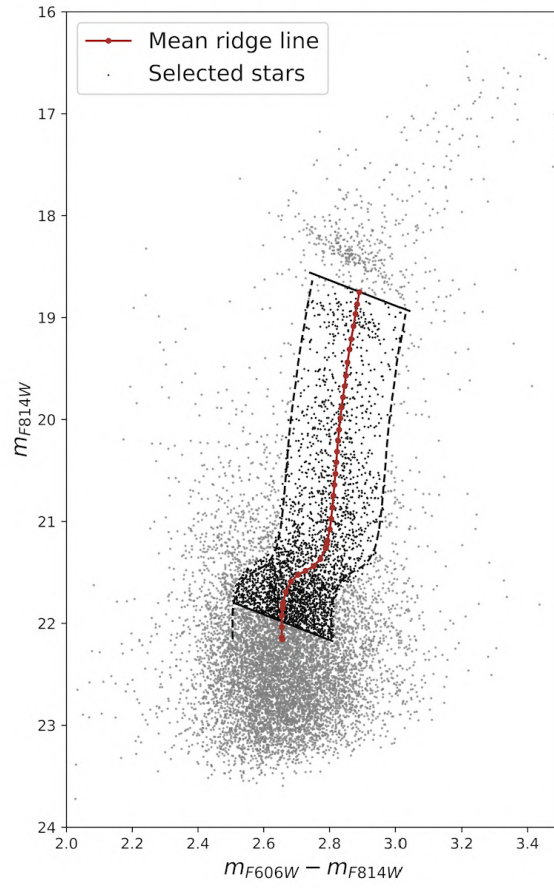
Figure 4.4: Reference stars selected according to their position.
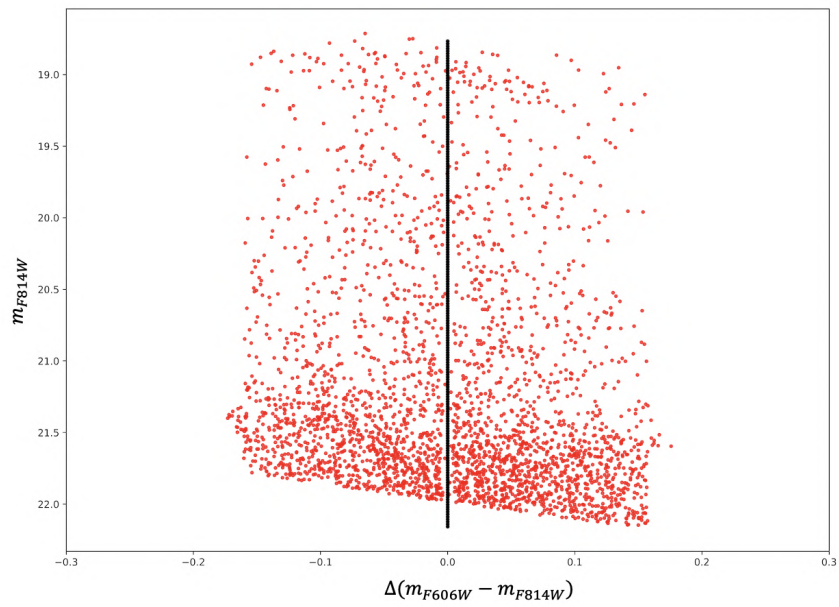

Figure 4.5: Distribution of the distances in the color of the reference stars (red dots) from the mean ridge line (black vertical line).
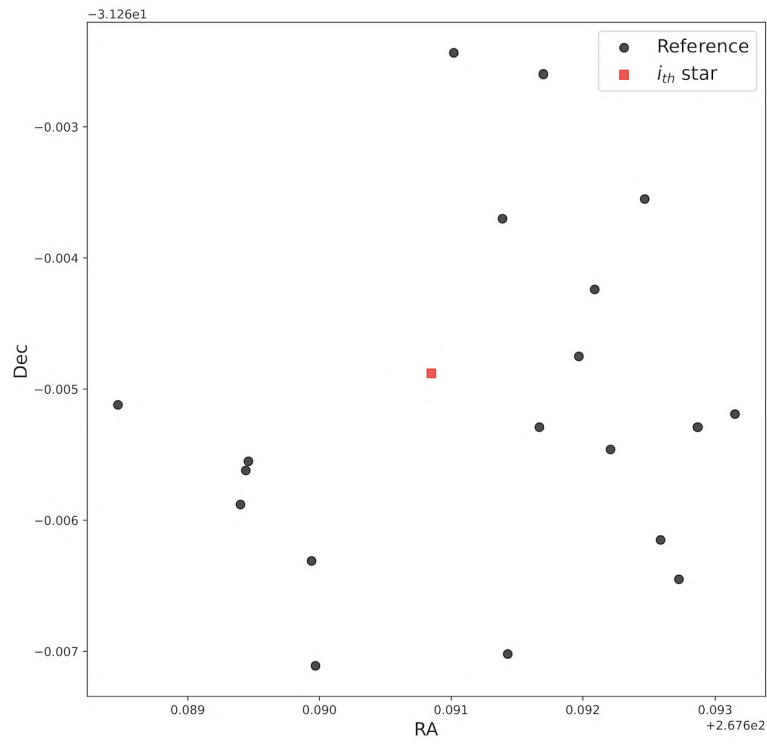
Figure 4.6: Reference stars selected according to their position in the plane of the sky.
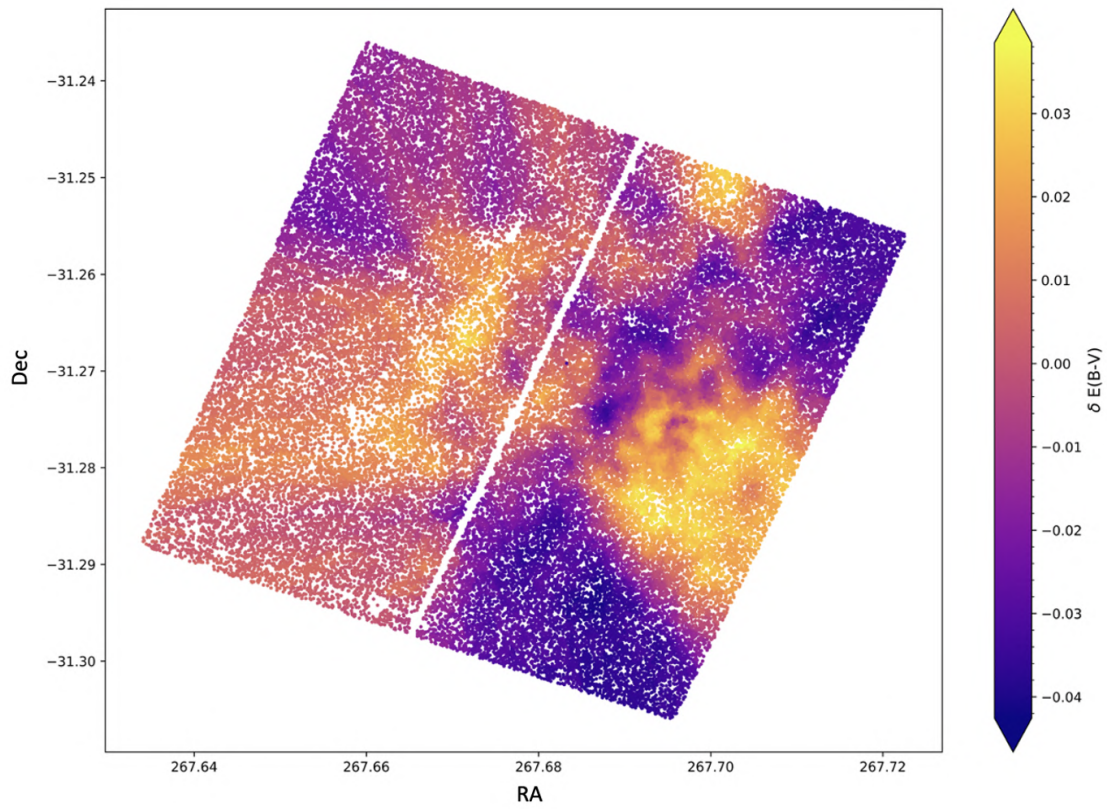
Figure 4.7: Reddening map obtained at the end of the procedure.

the final catalog by using **Eq.4.6** and **Eq.4.10**:

$$m_{0\lambda} = m_\lambda - R_\lambda \delta E(B-V) \qquad (4.12)$$

where m_λ are the magnitudes present in our catalogue.

We show here an example of the correction in the $(m_{F814W}\text{-}K_s, K_s)$ final CMD, where the m_{F814W} magnitude comes from the first epoch of the HST, while the K_s one from the 2013 GEMINI epoch (**Fig.4.8**).

We notice that the effect of the correction is admittedly small (**Fig.4.9**).
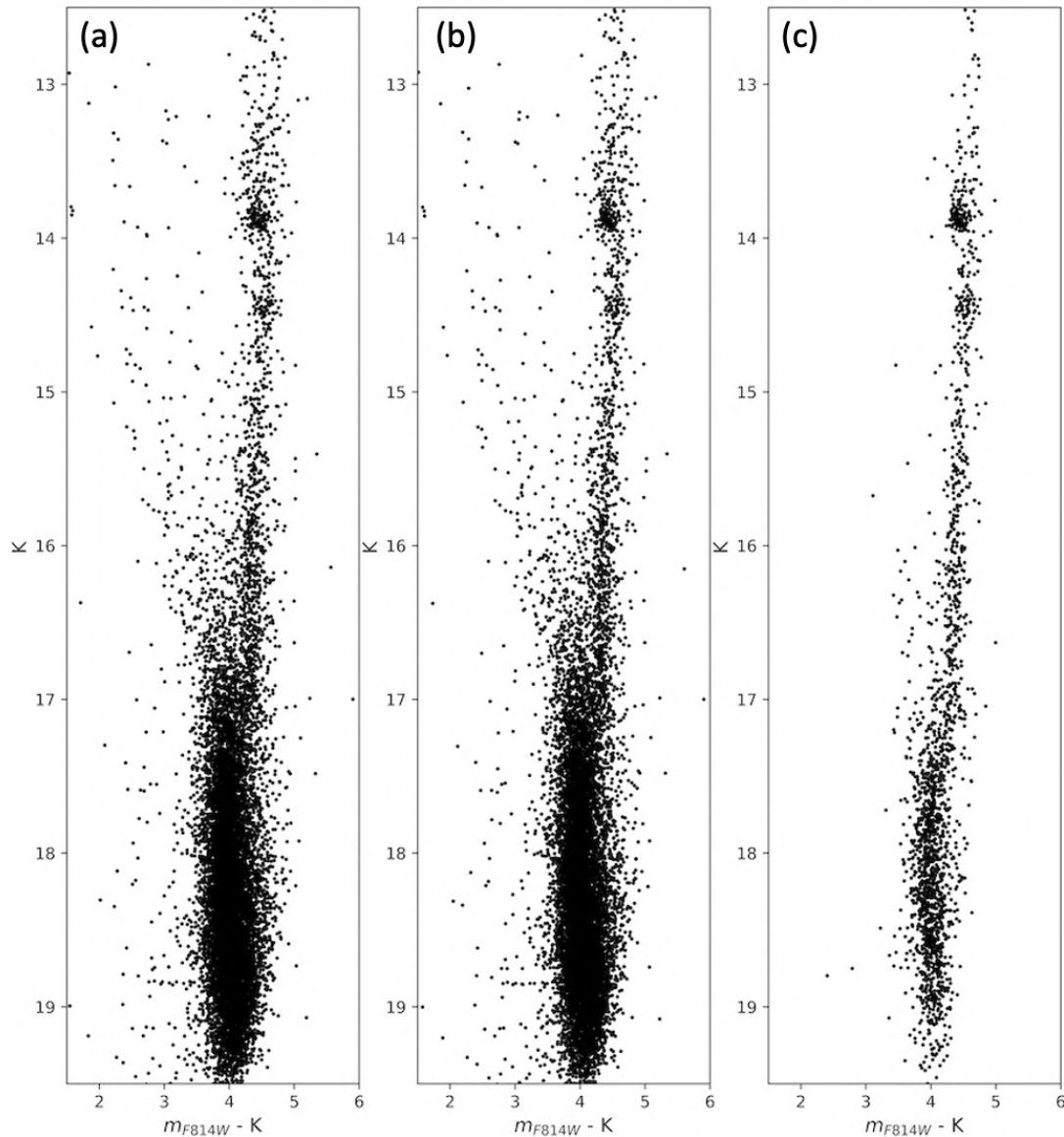
Figure 4.8: Comparison between the original CMD **(a)**, the differential reddening corrected CMD **(b)** and the reddening corrected-proper motions selected CMD **(c)**.

Thus, this can be considered a first-order correction of the differential reddening. However, a first improvement can be appreciated, since the evolutionary sequence (for instance the RGB) appears to be a little bit more defined, and the spread in color is reduced.
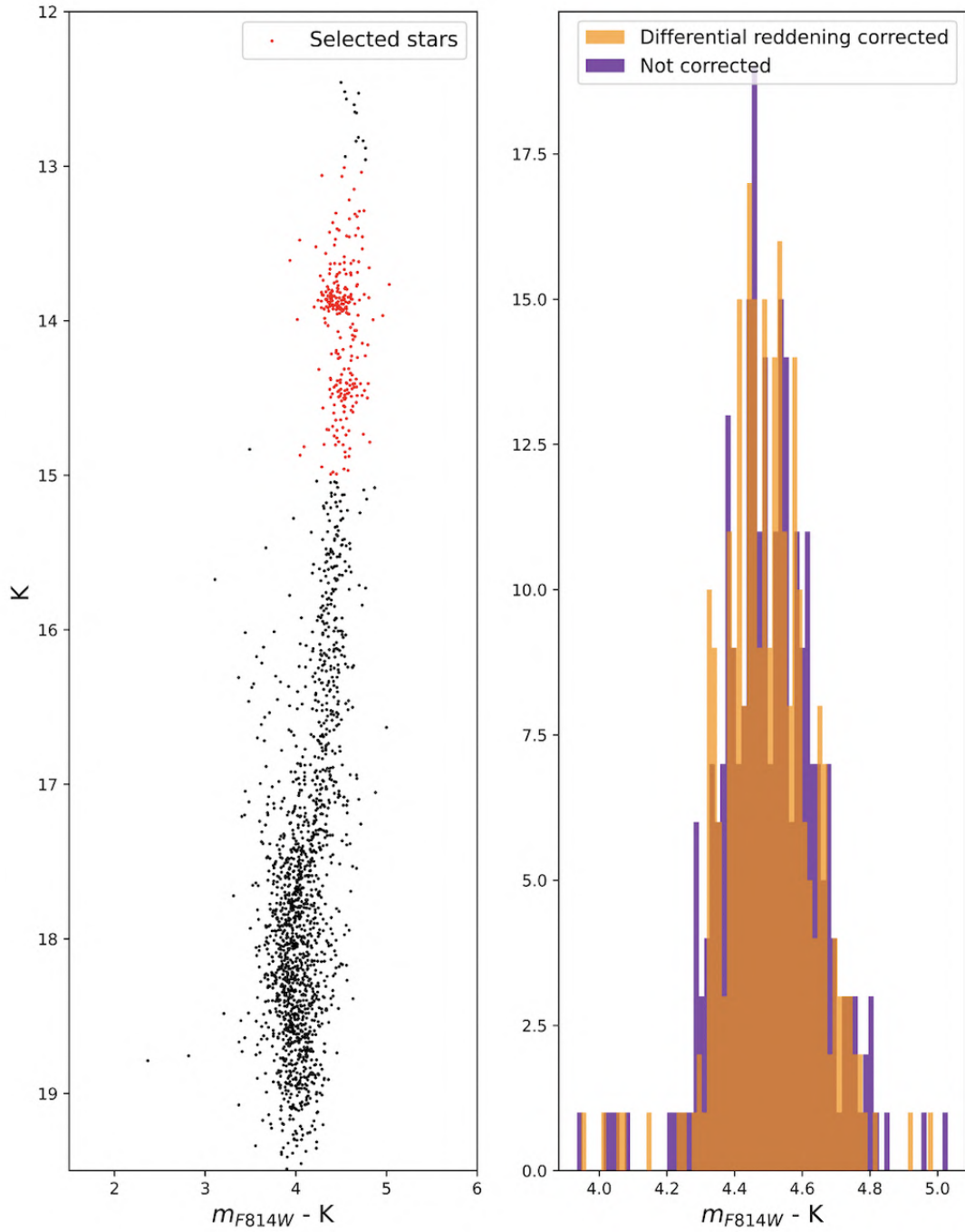
Figure 4.9: (a) Proper motions selected $(m_{F814W}\text{-}K_s, K_s)$ CMD in which a sample of RGB stars is shown in red; **(b)** Histogram representing the color $(m_{F814W}\text{-}K_s)$ of the sampled RGB stars before and after the differential reddening correction.

4.3 CMD

Finally in **Fig.4.10** we plot the proper motion selected and differential reddening corrected CMD for Terzan 6.

For the analysis, we chose the $(m_{F814W}\text{-}K_s, K_s)$ CMD since it provides the best combination of color baseline and sensitivity to reddening variations.

The CMD shows the typical morphology of an old metal-rich stellar population with a
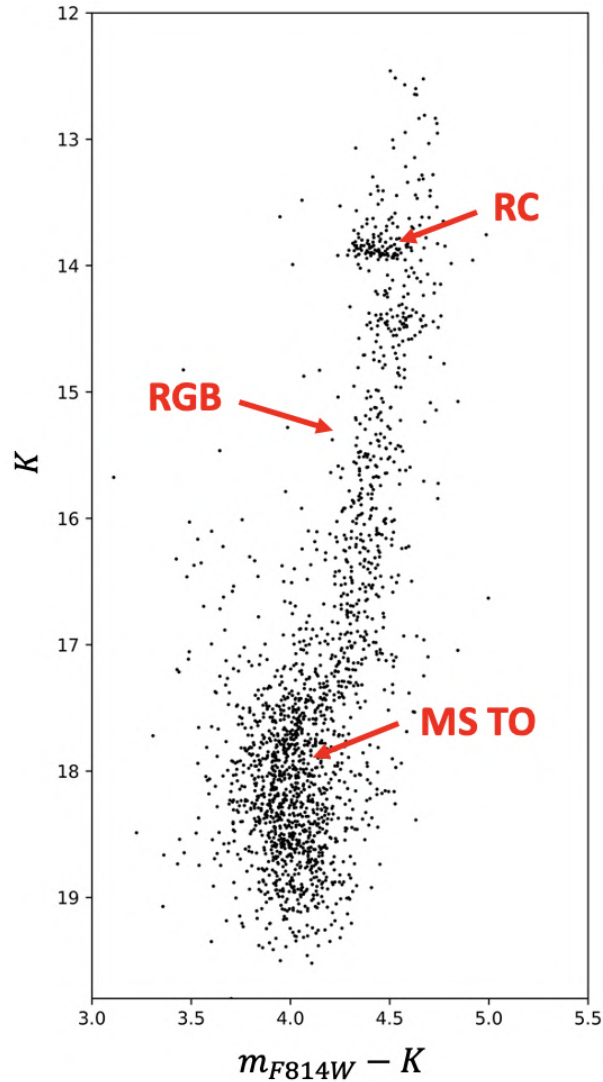
Figure 4.10: Proper motions selected and differential reddening corrected CMD.

well-defined and extended RGB and a well-populated Red Clump (visible around K_s=13.8 and color $4.2 < m_{F814W} - K_s < 4.5$). Also, the RGB bump is distinguishable as a clump of stars along the RGB at K_s=14.4.

The photometric sample extends down to K_s= 19.5 roughly 1.5 magnitudes below the MS-Turn Off which is approximately located at K_s=18. Despite the increasing spread in the color of the sequences for K_s>17.5 due to the increasing photometric errors, the MS TO is clearly visible and can be used to derive the cluster age.

In **Chapter 6** we use this CMD to determine the age of Terzan 6 via one of the most common ways to estimate the age of a stellar system: the isochrone fitting method.

Chapter 5

Determination of the structural parameters

As part of the characterization of the stellar system Terzan 6, in this chapter we derive the cluster gravity center and, for the first time, the star density profile from which the main structural and dynamical parameters can be derived.

Indeed as anticipated in **Chapter 1** GCs are the best laboratories in nature to study the effect of the dynamical evolution of stellar systems.

5.1 Theoretical introduction

Globular clusters are considered collisional systems, as their *2 body-relaxation time (t_{2b})*(Binney et al. 1987[8]) is much smaller than their age. The t_{2b} is defined as

$$t_{2b} \approx \frac{0.1N}{lnN}t_{cross} \tag{5.1}$$

where N is the number of stars in the system and t_{cross} the timescale needed for a star to cross the system.

The result is that the stars' orbits are strongly modified by the gravitational interactions, completely losing memory of the initial conditions in a timescale smaller than the age of the system. So, during the dynamical evolution of the system, high-mass stars lose energy that is acquired by low-mass ones, reaching the *energy equipartition*. The more massive stars spiral to the central region, while the less massive ones are ejected to the outer regions. This phenomenon is called *mass segregation*.

So it is reasonable that after several relaxation times, a stellar system can be considered completely relaxed and it is expected to acquire a *Maxwellian* velocity distribution, in which any inhomogeneity is completely erased.

The stellar dynamical model characterized by this velocity distribution is the so-called

isothermal sphere, which is characterized by a limitation: the model requires that a significant number of stars have a $v \to \infty$, in the wings of the distribution, which translates into a $M \to \infty$ if we consider a mass distribution, while a more realistic model should be characterized by:

- an isothermal profile in the central region, but a distribution function $\to 0$ if $v \to v_{escape}$, where v_{escape} is the escape velocity of the system;

- a finite limiting radius because of the effect of the Galactic tidal field.

The first dynamical model that was introduced to describe the stellar density and velocity distribution of stars in GC is the so-called *King profile* (King et al, 1966[38]). This is a mono-parametric family of models that can be fully described by W_0, a dimensionless parameter related to the central potential.

The typical shape of the King profile is the combination of an almost constant density central region (*core*) and a monotonic decreasing behavior in the outer part (**Fig.5.1**) and it can be used to describe both the radial density and surface brightness profiles in the majority of globular clusters.

Assuming this dynamical model, the structural parameters that are normally used to
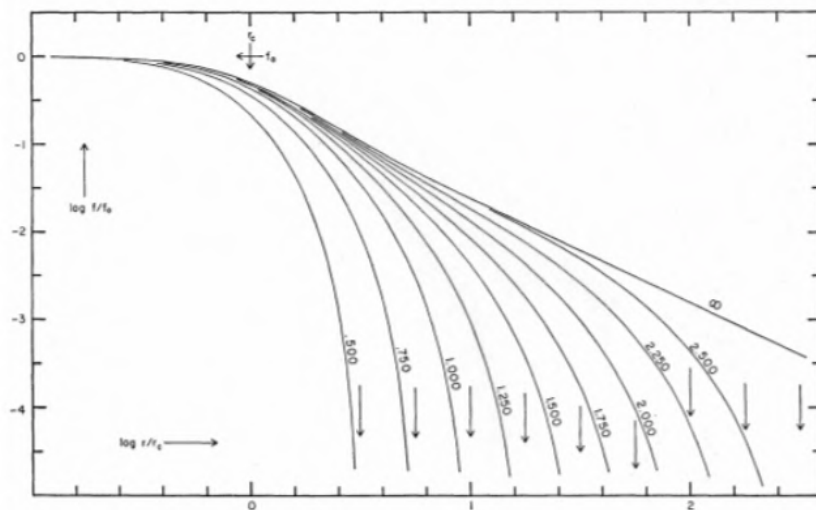
Figure 5.1: Example of a King profile with different c parameters. The y-axis shows the logarithmic surface brightness normalized to the central value, while the x-axis is the logarithmic distance from the center of the cluster in units of r_c.
The arrows highlight the positions of r_t for the different considered models.

describe the physical properties of the cluster are:

- *Core radius (r_c)*: it defines the distance from the center at which the projected density or the surface brightness is equal to half of the central value and it is strictly related to the *King radius (r_0)*, the characteristic scale of the model;

- *Half mass radius (r_h)*: it represents the radius that contains half of the total mass of the system;

- *Truncation radius or tidal radius (r_t)*: it defines the distance from the center of the cluster at which its gravitational potential is negligible compared to the Galactic one (so it is related to the finite size of the cluster).

According to these definitions, it is possible to derive an additional parameter, called *concentration (c)*, which can be used to fully characterize the King model (**Fig.5.1**). It is defined as:

$$c = log(\frac{r_t}{r_0}) \tag{5.2}$$

An additional dynamical effect, fundamental in the cluster dynamical evolution, is the so-called *core collapse*: according to the virial theorem, if a low-mass star is characterized by a v>v_{escape}, it can leave the cluster (*evaporation*) reducing the kinetic energy (K) of the central region which reacts by contracting. At this point, the system is more bounded and compact, which means that the number of gravitational interactions increases and the possibility to have the evaporation of the stars increases. This leads to the collapse of the core since the system is not able to reach the equilibrium anymore.

The collapse can be potentially halted by the presence of binary stars in the central region since the energy that is subtracted during the evaporation process is not the kinetic energy of the cluster anymore but the binding energy of the binary system. The main effect is the decrease in the distance between the stars of the binary system with the release of energy.

Observationally speaking, a cluster that has experienced the collapse of the core is characterized by a central cusp in the radial density/surface brightness profile. It is called Henon profile (Henon, 1961[31]).

So GCs can be divided into two different classes according to the fact they have experienced (Post-core collapse) or not (Pre-core collapse) the collapse of the core. This can be described by the *c parameter*:

- *Pre core collapse*: it means that the systems is dynamically young (c<2). In this case, the classical King profile can be used to describe the radial density/surface brightness profile;

- *Core collapse* or *Post-core-collapse*: the system is dynamically old (c>2), which means that it is currently in the phase of core collapse or has been concluded recently. To realistically represent the radial density/surface brightness profile, the Henon model is needed.

5.2   Center of gravity

As anticipated, the density profile of a GC is an important tool to study its dynamical state. As a first step in this direction, it is fundamental to estimate the *center of gravity* of the system (C_{grav}) which in this case has been derived by using resolved star counts.

In fact, due to the large spatial resolution of the data set exploited for the analysis, C_{grav} can be estimated by considering the resolved stars' counts with an iterative procedure (Montegriffo et al., 1995[47]). Specifically, C_{grav} has been defined as the barycenter of the positions of stars within a given magnitude range and located within a fixed distance from an approximate guess center.

The use of resolved stars has the main advantage of avoiding the observational bias that can come out when center derivation is based on the use of integrated light. In fact, few bright stars can dominate the integrated luminosity making the approach sensitive to statistical fluctuations.

The iterative procedure for the estimate of C_{grav} can be summarized schematically in the following way. Within the FOV of the observations (HST+GeMS) a position (α,δ) of the center from the literature has been defined (Harris 1996, 2010 edition[79]). Starting from this value, six radial ranges have been defined in which the mean of the position of stars has been derived. If the difference between the resulting solution and the reference is larger than 0.01", the mean is calculated again by using the center just derived and the procedure is iterated till convergence is reached (i.e. when the difference with the previous value is smaller than 0.01").

The choice of the confidence radii is set in such a way that a gradient in the cluster density profile is sampled. A decrease of the density profile starts to be detectable around the core radius, hence the confidence radii are typically set larger than these values.

For Terzan 6 we selected the following confidence radii: 3",5",10",15",20",25" (after checking that there were no problems related to the size of these regions compared with the FOV). The full iteration was repeated for three different magnitude ranges:

- $16 < m_{F814W} < 22$

- $16 < m_{F814W} < 21.5$

- $16 < m_{F814W} < 20$

It is important to define a range of magnitude in which this analysis can be performed for two main reasons:

1. the upper magnitude limit is necessary to exclude stars affected by saturation problems;

2. the lower magnitude limit is fundamental to avoid spurious fluctuations related to completeness problems.

Also, the magnitude limit guarantees that the stars that were selected for the determination of the center have approximately the same mass.

We considered as rough reference center the one obtained from the visual inspection of an HST image.

At the end of the procedure, we obtained 18 independent positions of the center of gravity of the system which are reported in **Table 5.1**.

The final result is obtained by averaging the 18 center positions we obtained and the associated error is the standard deviation of the mean.

The C_{grav} value of Terzan 6 is $\alpha_{J200} = 17^h \, 50^m \, 46.9^s$, $\delta_{J200} = -31° \, 16' \, 30.14''$ with an error of 0.53" on α_{J200} and 0.91" on δ_{J200} (**Fig.5.2(a)**). It is important to emphasize that the new determination of the cluster center is by far different from that reported in the literature (for instance it is located at a distance of ≈ 8.6" from the one of the Harris Catalogue[79], see **Fig.5.2(b)**).

5.3   Radial density profile

Once the C_{grav} has been determined, it was possible to derive the radial density profile from the star counts in annuli at different distances from the cluster center. We stress that this is the first density profile obtained by using resolved stars.

The implemented routine splits the FoV into concentric rings of different sizes centered on C_{grav} set to ensure good statistics. In some cases, such as the one shown in **Fig.5.3**, angular limits have been applied to some rings to avoid areas where the observations do not fully sample the sectors. Stars selected in this way for density estimation are shown in red.

To take into account possible asymmetries, the procedure we considered is the one described by Ferraro et al., 1999[26], characterized by the definition of different sub-sectors in each annulus.

So each ring is divided into a variable number of sub-sectors (from 2 to 4). The density within each sub-sector is calculated as the ratio between the number of stars present and the area in $arcsec^2$.

The radial density corresponding to each ring is then determined by averaging the density values found in the individual sub-sectors, and the error associated with each density value is represented by the standard deviation of the mean.

To account for completeness problems connected to the analysis, we considered a combination of the results obtained in two different magnitude ranges ($16 < m_{F606W} < 20.5$ for the central regions of the GC r<8", while $16 < m_{F606W} < 21$ for r>8").

These two profiles have been combined to obtain a total one, applying a normalization to the distributions. The normalization was calculated using the density values obtained inside the common rings (r>13" for the normalization between HST+GeMS and HST). The mean

| R	$16<m_{F814W}<22$			$16<m_{F814W}<21.5$			$16<m_{F814W}<20$		
	RA	Dec	N. stars	RA	Dec	N. stars	RA	Dec	N. stars
3"	267.6955575	-31.2752385	122	267.6955957	-31.2752861	109	267.6957012	-31.2751902	51
5"	267.6956302	-31.2753341	308	267.6957058	-31.2752233	235	267.6957310	-31.2751976	97
10"	267.6958351	-31.2753109	859	267.6957448	-31.2751789	561	267.6954862	-31.2751739	226
15"	267.6957430	-31.2749970	1400	267.6957234	-31.2749982	859	267.6954280	-31.2750490	327
20"	267.6955981	-31.2747705	1964	267.6955793	-31.2746764	1136	267.6956175	-31.2750639	427
25"	267.6953915	-31.2744437	2538	267.6953451	-31.2746059	1420	267.6952997	-31.2749677	528

Table 5.1: Positions (α,δ) of the center of gravity obtained during the iterative procedure considering 3 different magnitude ranges $16 < m_{F814W} < 22$, $16 < m_{F814W} < 21.5$, $16 < m_{F814W} < 20$ and 6 confidence radii (3",5",10",15",20",25"). The number of stars used in the evaluation of the different center positions is reported.
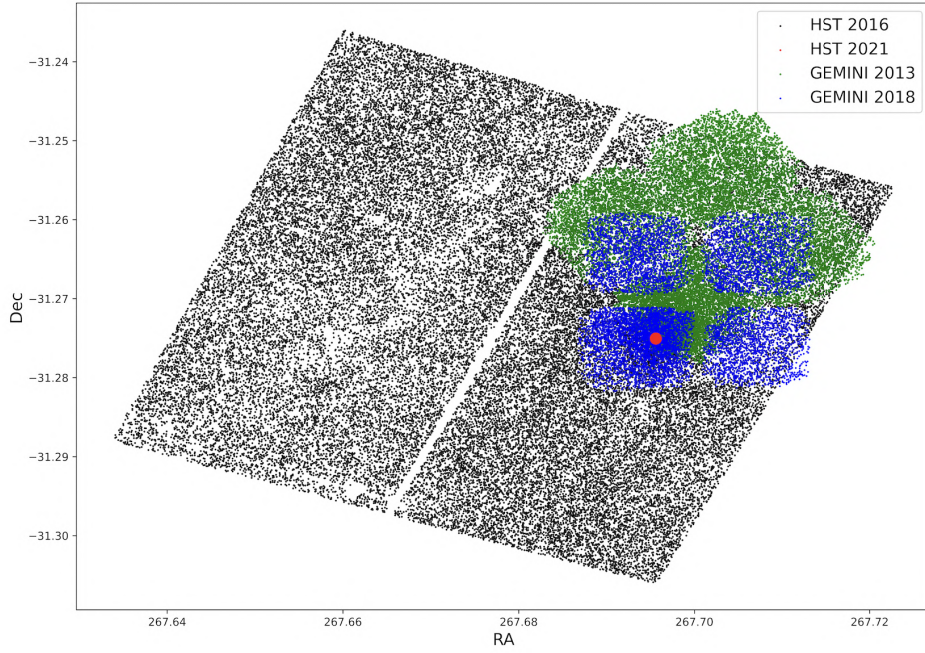
(a) *FOV of the catalogue with the position of C_{grav} (red dot).*
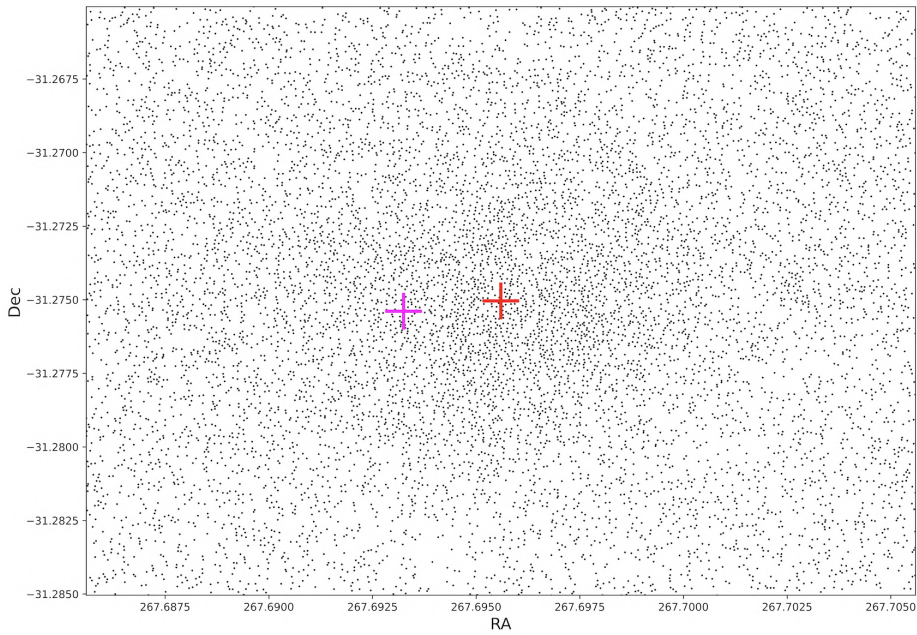
(b) *Zoomed version of the map, just by considering HST data, in which a comparison of our result (red cross) with the Harris value (fuchsia cross) is shown.*

Figure 5.2: Map of the FOV obtained from the analyzed catalog (**Sec. 3.4**) in which the center of gravity of Terzan 6 is highlighted in red.
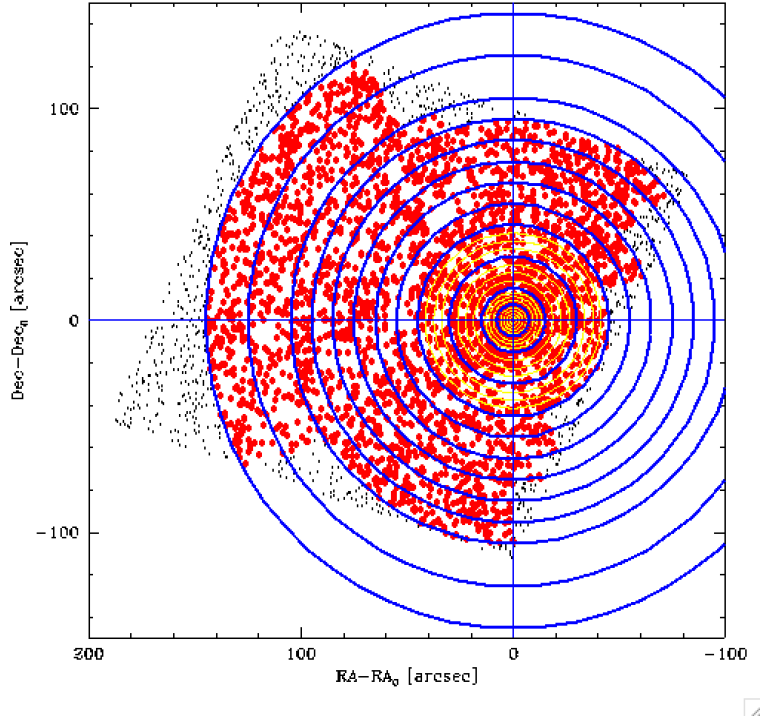
Figure 5.3: Map of the concentric annuli exploited for the realization of the radial density profile. The selected stars (red dots), the sectors (blue) and the sub-sectors (yellow) are highlighted.

of the difference of these values represents the respective normalization for the two pairs of distributions.

The total profile resulting from this operation is represented in **Fig.5.4** (and **Fig.5.5**) by empty points.

In the outermost regions of about r > 25" we note a flattening of the trend with density values that remain constant at about 0.28 stars arcsec^{-2}, caused by the contribution of the galactic field stars.

Through this feature, it is therefore possible to estimate the contribution of the background and subtract it from the observed profile. The average level of the background density was defined as the mean of the densities of the 6 outermost rings. This value was subtracted from the observed profile.

The resulting decontaminated density profile is represented by solid dots with relative errors. As expected, the decontamination significantly affects the most external region leaving essentially unaffected the central ones.

To obtain an estimate of the structural parameters of Terzan 6, the density profile from which the average background was subtracted was compared with the family of King models, varying W_0 from 4.0 to 12 with steps of 0.05.

For each explored value of $W_{0,i}$ the scale parameter $r_{0,i}$ and the central density $\Sigma_{0,i}$ were derived, giving the minimum reduced χ^2 (χ^2_{min}). The value corresponding to the lowest value

of χ^2_{min} (χ^2_{best}) is adopted as the best-fit model.

In addition to the best-fit values for $\Sigma_{0,i}$, $r_{0,i}$ and $W_{0,i}$, this procedure also provides values for r_c and r_h.

The best-fit profile thus derived is shown in **Fig.5.4**. They correspond to $r_c = 2.75''[\pm0.35]$, $r_h = 24.08''$, $r_t = 229.01'' = 3.82' \pm 1.5'$. The uncertainties for each of these values are derived with the maximum variation in the range $\chi^2 \leq \chi^2_{best} + 1$. The derived concentration parameter is $c = 1.91[+0.13, -0.15]$[1].

These values differ slightly from those estimated by Harris 1996, 2010 edition[79] using the surface brightness of the cluster, which are $r_c = 3''$, $r_h = 26.4''$, $c = 2.50$.

In both analyses, the large c value and the small r_c value can be considered hints of a dy-
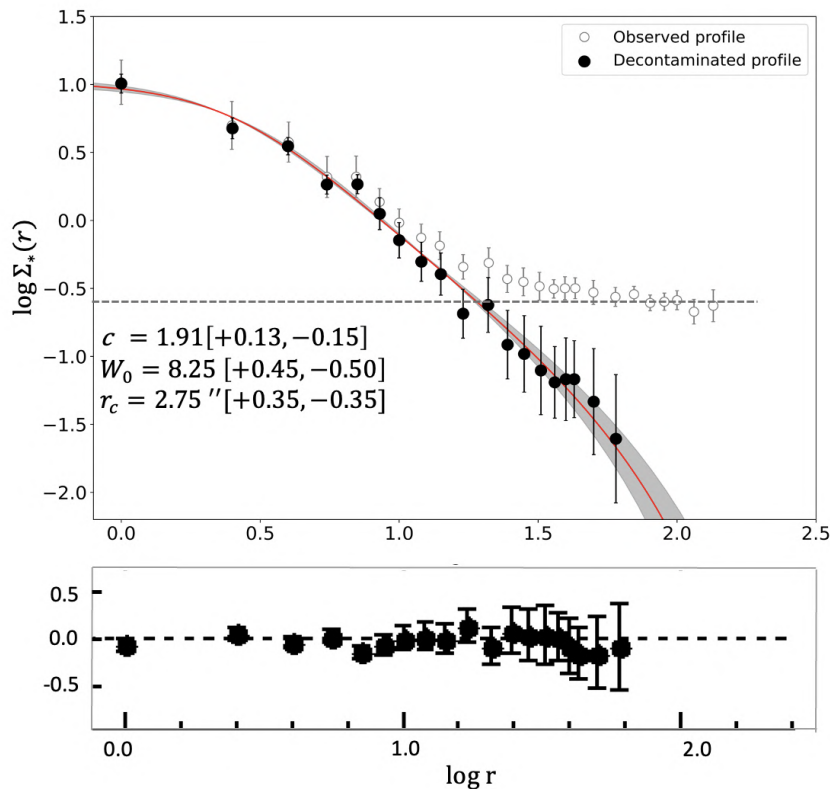

Figure 5.4: Upper panel: Radial density profile of Terzan 6. The lighter points represent the original observed profile in which the effects of field star is evident in the external regions, while the darker ones are the decontaminated one. The best-fit profile is also shown as a red line and the shaded regions define the error associated with the parameter W_0, which defines the model. The grey dotted line defines the mean level of the background.

Lower panel: Residuals of the best-fit procedure with the King model.

namically evolved cluster (Post core-collapse) and this is why we also tried to fit the central region of the density profile with a power law in order to highlight the presence of a cusp. The result is shown in **Fig.5.5**, where we neglected the 3 innermost points of the profile in

---

[1]The error evaluation has been done exploiting the Cosmic Lab website[14] and Miocchi et al., 2006[45]

the best-fitting procedure with the King models, in order to exploit them for the definition of the central cusp.
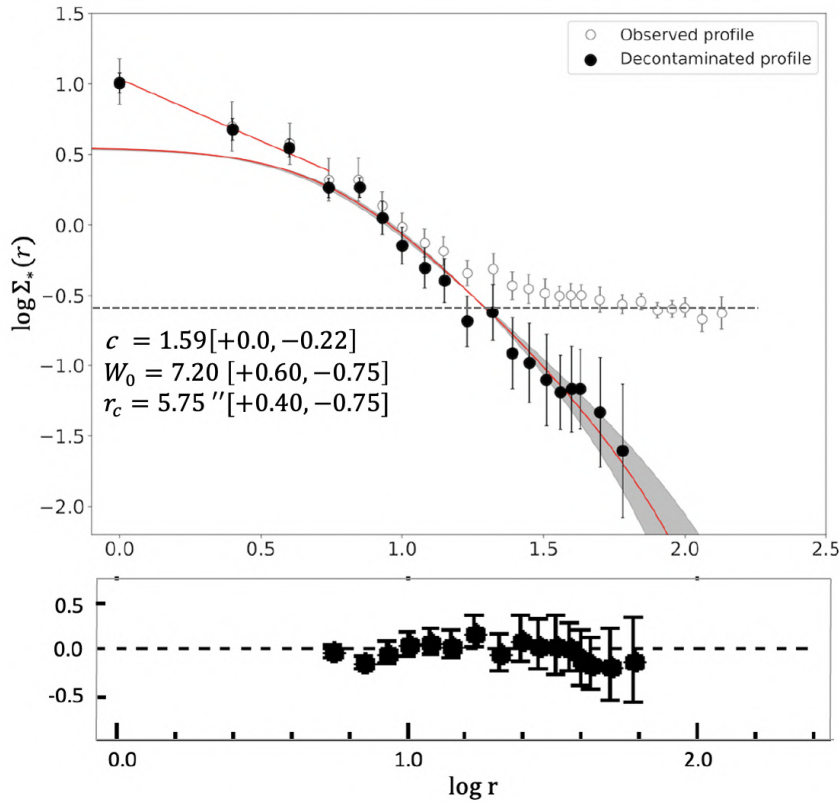
Figure 5.5: Upper panel: Radial density profile of Terzan 6, characterized by the presence of the King model for the external region and a power-law for the central one.
Lower panel: Residuals of the best-fit procedure with the King model.

The structural parameters obtained by considering this King model are $W_0 = 7.20[+0.60, -0.75]$, $r_c = 5.75''[+0.40, -0.75]$, $c = 1.59[+0.0, -0.22]$, $r_h = 25.93''$, $r_t = 232.59'' = 3.88' \pm 1.1'$, while the power law is defined as $\log\Sigma_* = -0.88 \times \log r + 1.036$.

Both models are overall consistent according to *reduced χ^2 test*, and in both cases, the large value of c (in the first case) and the presence of a cusp (in the second case) indicated that Terzan 6 is in an advanced stage of its dynamical evolution. Hence the analysis presented here clearly indicates that Terzan 6 has experienced the collapse of the core.

Chapter 6

Age determination

To fully characterize Terzan 6 and possibly its formation it is necessary to provide an accurate estimate of its age.

In order to do that, we first derived the distance modulus and the mean color excess, we then used the isochrone fitting approach.

6.1 Distance Modulus and mean Color Excess

The distance modulus and the mean color excess of Terzan 6 can be obtained by performing a comparison with a well-known GC of similar metallicity, characterized by a larger galactic latitude compared to Terzan 6 so that its extinction value and its uncertainty are much smaller and for which the distance has been robustly derived. In our analysis, we used 47 Tucanae (47Tuc) as reference GC to constrain the distance modulus and the color excess of Terzan 6.

Indeed, 47Tuc is one of the best-studied stellar clusters in the Galaxy. It has a metallicity [Fe/H]=-0.72 (Harris 1996, 2010 edition[79]), which nicely matches the one derived for Terzan 6 ([Fe/H]=-0.56; Harris 1996, 2010 edition[79]), it is located at $l = 305.89°$ and $b = -44.89°$ thus being characterized by a low foreground extinction E(B-V)=0.04, and its distance modulus is well constrained $(m - M)_V$=13.37.

For the analysis we used the publicly available 47Tuc HST ACS/WFC catalog obtained as part of the 'Galactic Globular Cluster Legacy Survey' (Sarajedini et al. 2007 [69]). In particular, consistently with what was done for Terzan 6, we used the m_{F814W} and m_{F606W} in the VAGAMAG photometric system.

We compared the $(M_{F606W}\text{-}M_{F814W}, M_{F606W})$ PM-selected CMD of Terzan 6 with the 47Tuc one, after reporting them to the absolute plane with the aim of detecting the shifts in magnitude and color of Terzan 6 in order to superimpose them.

For Terzan 6 we assumed the color excess and distance modulus reported in the literature (E(B-V)=2.35, $(m - M)_V$=21.44).

The distance- and reddening-corrected CMDs of the two clusters are super-imposed in **Fig.6.1**. We note that a fairly good match between the CMDs is obtained **Fig.6.1 (left)**. However, the color superposition further improves if a shift of $\Delta(E(B-V)) = 0.0)$ was subtracted to Terzan 6 color, thus implying a final E(B-V)=2.30±0.23 (conservatively assuming a 10% error) for Terzan 6 (**Fig.6.1 (right)**).

Now, by assuming this new estimate for E(B-V) we refined the distance modulus estimate for Terzan 6 and we compared the luminosity function of the two GCs normalized to the peak of the stellar number counts (**Fig.6.2**).
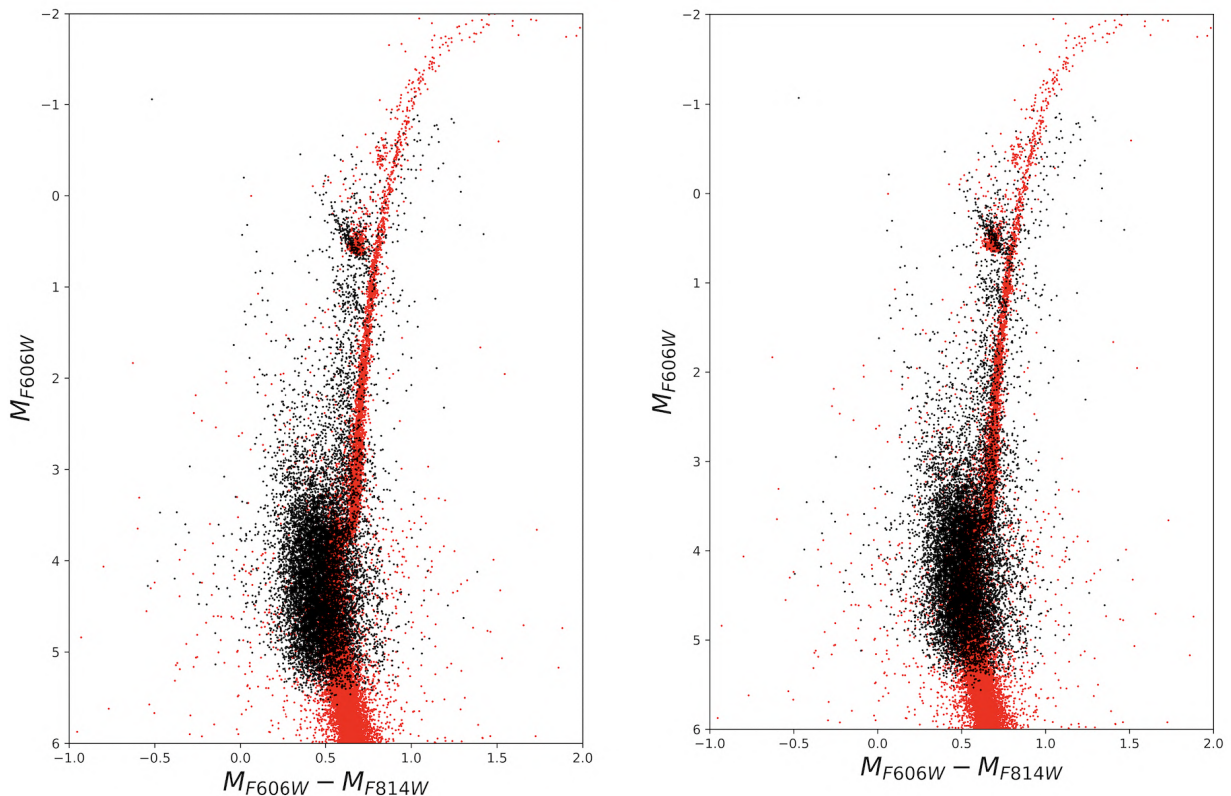
(a) *Original Terzan 6 and 47Tuc CMDs.* **(b)** *Terzan 6 and 47Tuc CMDs after the application of a shift of 0.05 in color excess.*

Figure 6.1: Comparison between the $(M_{F606W}\text{-}M_{F814W}, M_{F606W})$ CMD of the PM-selected catalog of Terzan 6 (black) and 47Tuc (red).

We derived also the true distance modulus $(m - M)_0 = 14.26 \pm 0.72$, in agreement with $(m - M)_0 = 14.11$ (Harris, 1996 (2010 edition)[79]), $(m - M)_0 = 14.25$ (Barbuy et al.,1997[3]), $(m - M)_0 = 14.16 \pm 0.14$ (Fahlman et al.,1995[22]) assuming the same value for the R parameter $(R_V = 3.12)$.

At this point, it was possible to estimate the distance (d) of Terzan 6 by using:

$$(m - M)_0 = -5 + 5log(d) \tag{6.1}$$
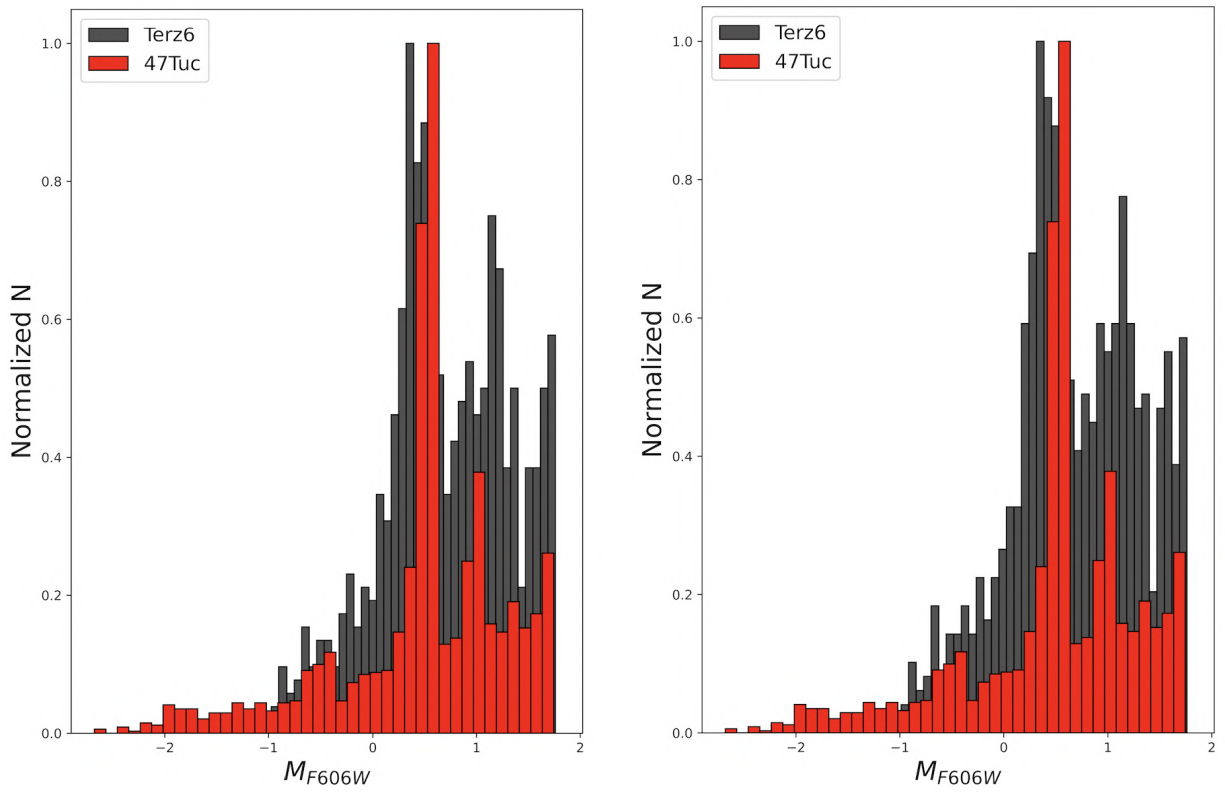
(a) *Original Terzan 6 and 47Tuc luminosity functions.*

(b) *Terzan 6 and 47Tuc luminosity functions after the application of a shift of 0.05 in color excess.*

Figure 6.2: Comparison between the luminosity functions of Terzan 6 (black) and 47Tuc (red).

The result we obtained is d=7.13 ±0.70 kpc and it is slightly larger but again comparable, within the errors' range, with $d_{Harris} = 6.80$ kpc, $d_{Barbuy} = 7.0 \pm 0.6$ kpc and $d_{Fahlman} = 6.80 \pm 0.46$ kpc.

6.2 Isochrone fitting

The procedure we adopted for the determination of the age of Terzan 6 is the so-called *isochrone fitting* which consists in the comparison of the observed CMD with different stellar evolution models.

To perform such a comparison we adopted the previously obtained distance modulus and reddening (we also adopted R_V=3.12), and the available estimate for metallicity [Fe/H]=-0.56 (Harris 1996, 2010 edition[79]). We also assumed that Terzan 6 stars have [α/Fe]=+0.4, as typically observed in old bulge globular clusters.

The theoretical models which have been used for this analysis are the *BASTI (A Bag of Stellar Tracks and Isochrones)* α-enhanced isochrones (Pietrinferni et al.,2004[60]). They can be retrieved at the following link http://albione.oa-teramo.inaf.it/main.php.

In particular, we assumed a [Fe/H]=-0.60 (the closer value to the Harris one we adopted in our work), which means Z=0.01, Y=0.259 and [M/H]=-0.25, where Z and Y are the metals and the He mass fractions respectively, while [M/H] is the abundance of metals (considering both Fe and α elements) normalized to the H and the solar abundances.

We retrieve models in both the Johnson-Cousin photometric system (UBVRIJKL) and ACS/WFC bands (F435W, F475W, F555W, F606W, F625W, F775W, F814W). In particular, we focused on a limited interval of ages going from 8 to 14 Gyr and we considered the $(m_{F814W} - K_s, K_s)$ CMD since it provides the best compromise between large wavelength range baseline and photometric accuracy at the level of the turnoff (**Fig.6.3**).

To determine the age of the system, we implemented an iterative procedure that is able to find the best fit among the different theoretical models according to the minimization of the χ^2. We evaluated the minimum distance, both in magnitude and in color, normalized by the quadratic sum of the error associated with the color and the K magnitude, between each observed star and the corresponding point on the isochrone.

The χ^2 parameter has been computed by selecting a sub-sample of stars located in the magnitude range $14 < K_s < 18$ in order to analyze the TO region, where the isochrone shape is particularly sensitive to age variations.

The best-fit age for Terzan 6 obtained from this procedure was 13.5 ± 0.5 Gyr (**Fig.6.4**). The error was obtained by considering the one on the color excess and using it in the routine for the age determination so that it was possible to get two different age values that represent the error range.

To check for possible systematic effects on the age estimate determined by the adopted set
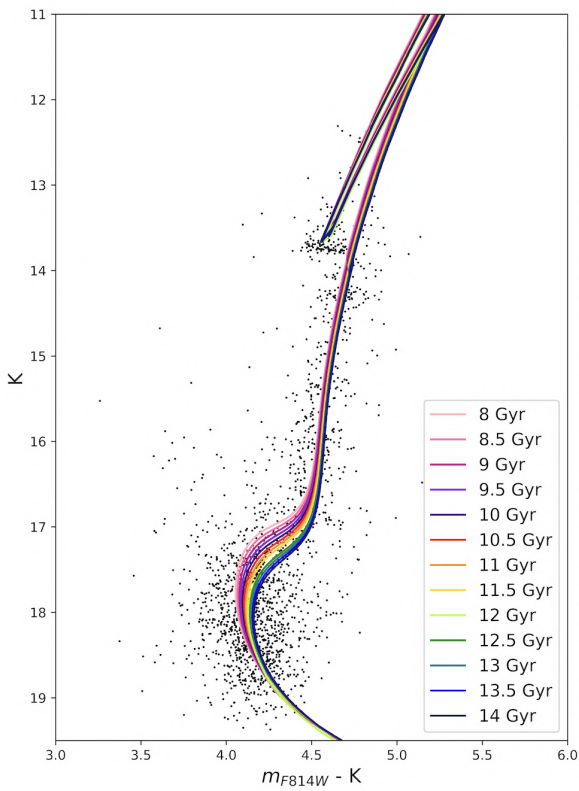
(a) *($m_{F814W} - K_s, K_s$) CMD of Terzan 6.*
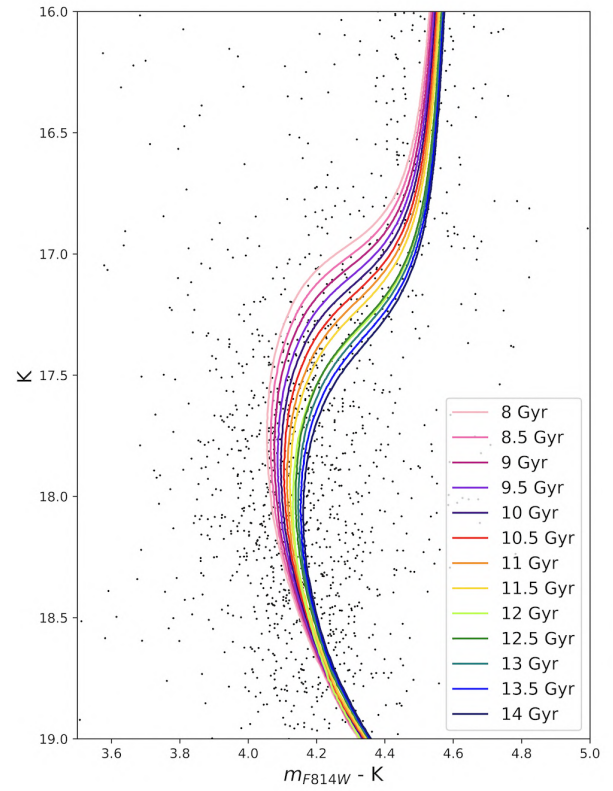
(b) *Zoomed ($m_{F814W} - K_s, K_s$) CMD of the MS-TO region of Terzan 6 with the different isochrones.*

Figure 6.3: PM-selected ($m_{F814W} - K_s, K_s$) CMD in which the different isochrones (8-14 Gyr) are plotted with different colors.

Figure 6.4: Best fit *BASTI* isochrone obtained from the χ^2 procedure.

of theoretical models, we also decided to compare the result we obtained by exploiting the BASTI isochrone with the *PARSEC (Padova and Trieste Stellar Evolution Code)* ones[57], by adopting the same input parameters' value 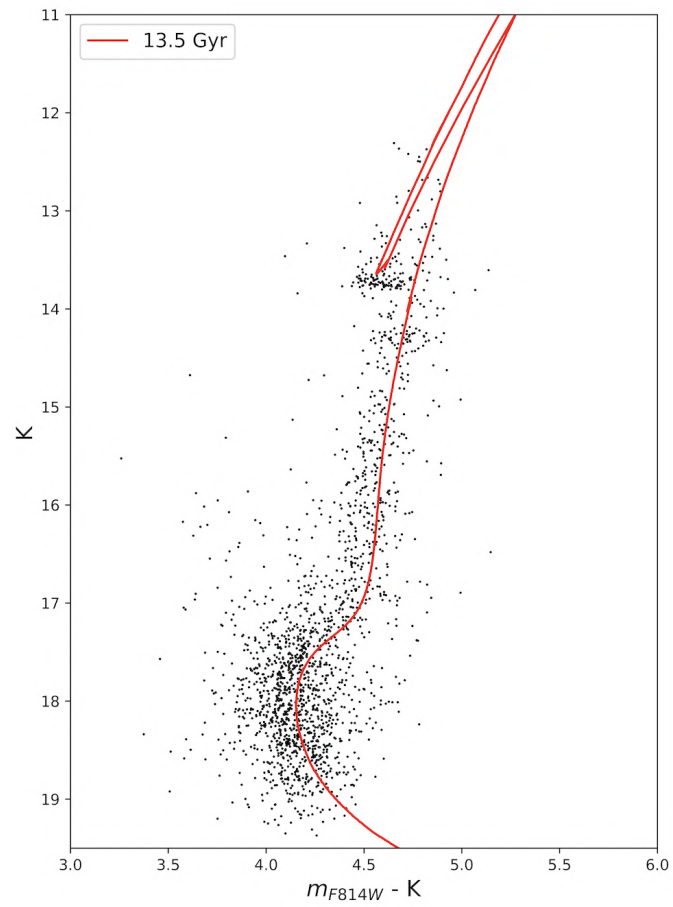as before ([Fe/H], E(B-V),$(m - M)_V$ etc.). These models can be retrieved at the following link http://stev.oapd.inaf.it/cgi-bin/cmd.

In performing such a comparison we had to take into account that one of the main differences is that they are computed by assuming a solar $[\alpha/Fe]$ and the reddening correction is automatically performed.

We considered the same age range and iterative procedure as in the case of the BASTI isochrones. The result that minimized the χ^2 is $t = 13 \pm 0.5$ Gyr. Such an estimate is in full agreement with the one obtained with the BASTI database, the comparison is shown in **Fig.6.5**.

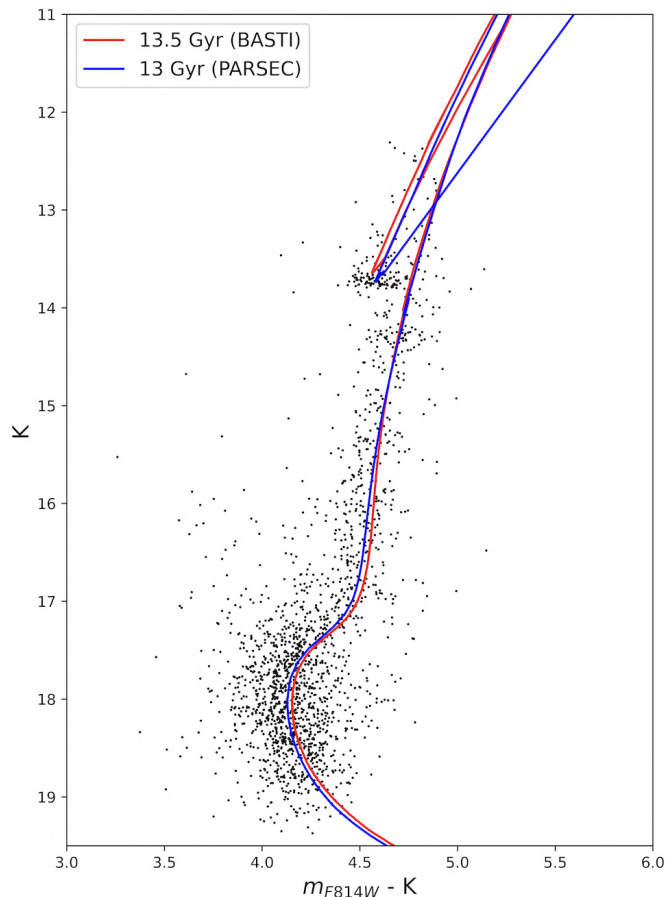Since a GC is most likely to be characterized by a super-solar $[\alpha/Fe]$, we assumed in the

Figure 6.5: Comparison between the best fit *BASTI* and *PARSEC* isochrones obtained from the χ^2 procedure.

following analysis the age obtained from the BASTI isochrone ($t = 13.5 \pm 0.5$ Gyr).

We compared Terzan 6 age with different already analyzed Bulge GCs (**Table 6.1**), as shown in **Fig.6.6**.

The age measurements have been obtained from different works: NGC 6528 (Lagioia et al. 2014[39]; Calamida et al. 2014[9]), NGC6553 (Zoccali et al. 2001[81]), Terzan 5 (Ferraro et al. 2016 [24]; here we take into account only the old, dominant component of the system), NGC6304 (Dotter et al. 2010[19]), NGC6637, NGC6652, NGC6723 (Dotter et al. 2010[19]; VandenBerg et al. 2013[78]), NGC 6624 (Dotter et al. 2010[19]; VandenBerg et al. 2013[78]; Saracino et al. 2016[68]), NGC 6569 (Saracino et al. 2019[67]), HP1 (Kerber et al. 2019[36]), NGC 6558 (Barbuy et al. 2007[4]), NGC 6522 and NGC 6626 (Kerber et al. 2018[37]). Their metallicity was collected from Harris 1996, 2010 edition[79] with only two exceptions: NGC 6569 (Johnson et al. 2018[34]) and NGC 6624 (Valenti et al. 2011[77]).

We noticed that the derived age of Terzan 6 is completely compatible, within the errors' range, with the average Bulge GCs age.

Finally, by exploiting the information about the age of the system and the metallicity, we
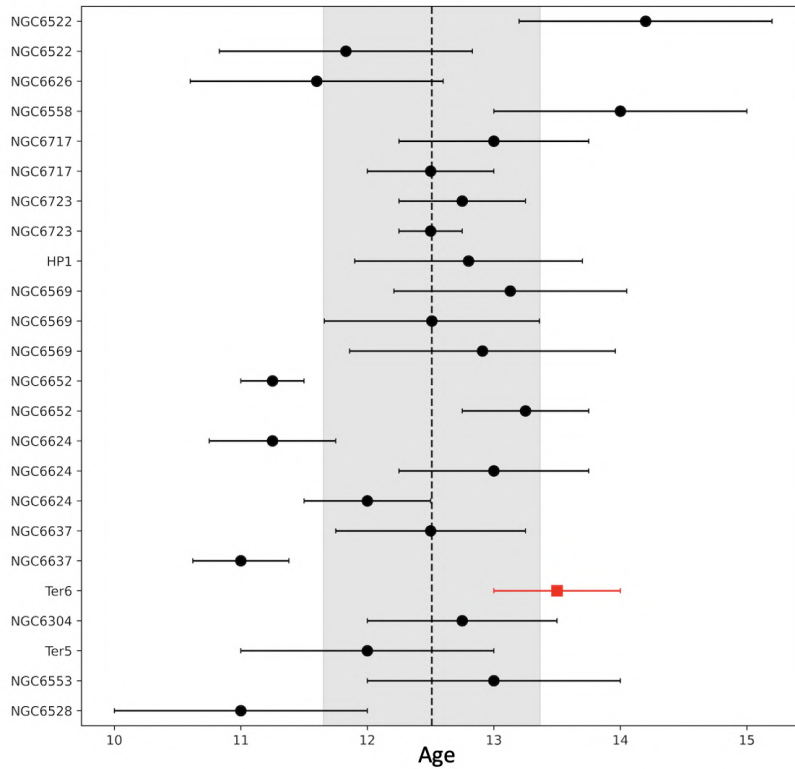
Figure 6.6: Age distribution of different Bulge GCs, where Terzan 6 is highlighted (red square). The mean age value (black dotted line) ± its associated standard deviation (grey shaded region) is shown.

can place Terzan 6 in the age-metallicity plane, together with the Bulge GCs reported in **Table 6.1** (**Fig.6.7**).

They can be compared with a sample of Halo GCs (Forbes et al.,2010[27]), which are metal-poor and characterized by larger distances from the Galactic center.

In the comparison (**Fig.6.8**) we can easily notice a younger and metal-poor branch in the Halo GCs distribution (blue shaded region), which represents the accreted systems, and a

Name	Age (Gyr)	Error	[Fe/H]
NGC6528	11.00	1.00	-0.11
NGC6553	13.00	1.00	-0.18
Ter5	12.00	1.00	-0.23
NGC6304	12.75	0.75	-0.45
NGC6637	11.00	0.38	-0.64
NGC6637	12.50	0.75	-0.64
NGC6624	12.00	0.50	-0.69
NGC6624	13.00	0.75	-0.69
NGC6624	11.25	0.50	-0.69
NGC6652	13.25	0.50	-0.81
NGC6652	11.25	0.25	-0.81
NGC6569	12.91	1.05	-0.87
NGC6569	12.51	0.85	-0.87
NGC6569	13.13	0.92	-0.87
HP1	12.80	0.90	-1.00
NGC6723	12.50	0.25	-1.10
NGC6723	12.75	0.50	-1.10
NGC6717	12.50	0.50	-1.23
NGC6717	13.00	0.75	-1.23
NGC6558	14.00	1.00	-1.32
NGC6626	11.60	1.00	-1.32
NGC6522	11.83	1.00	-1.34

Table 6.1: Information about different Bulge GCs: age and associated error, metallicity [Fe/H].
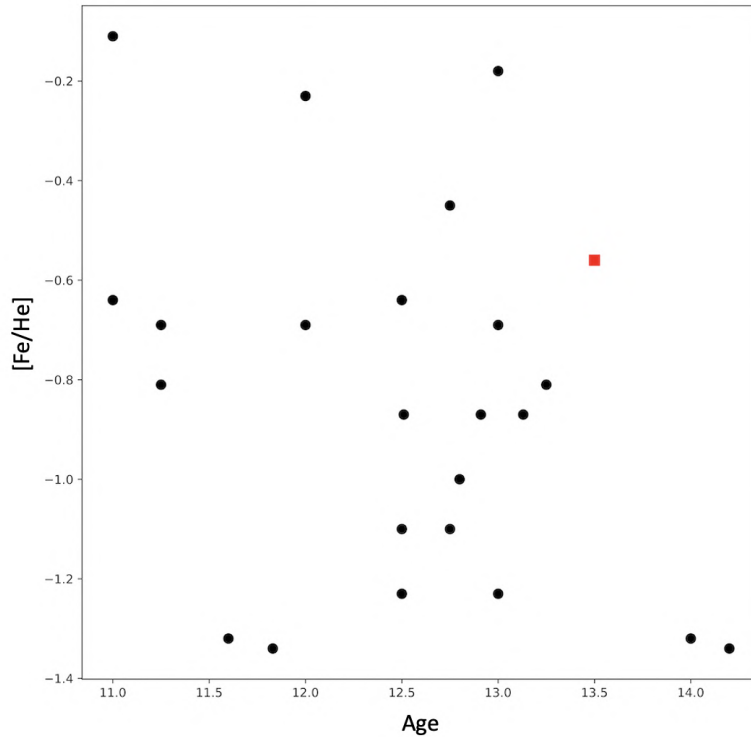
Figure 6.7: Age-metallicity plane populated by different Bulge GCs (Terzan 6 is reported as a red square).

second component, more limited in age (t>11.5) characterized by larger metallicity (green shaded region), composed by systems more likely formed in situ.

The age-metallicity relation is strictly linked to the progenitor's mass, the larger it is the easier is to reach higher metallicity values (*Mass-Metallicity relation*). So, since we are observing Milky Way's GCs, we expect that the metal-rich systems are more likely formed in situ.

Also, a large fraction of the 'in situ' metal-rich systems is composed of Bulge GCs, as expected since it is quite difficult to find accreted GCs in the central region of our Galaxy due to the hostility of the environment (tidal shock, interactions with the potential well, etc.). In this scenario, Terzan 6 position in this plane is in perfect agreement with the expected one.

Figure 6.8: Comparison between Halo GCs (black dots) and Bulge GCs (orange dots) in the age-metallicity plane. The position of Terzan 6 is highlighted in red. The blue and green shaded regions represent the two different branches approximately.

Conclusion

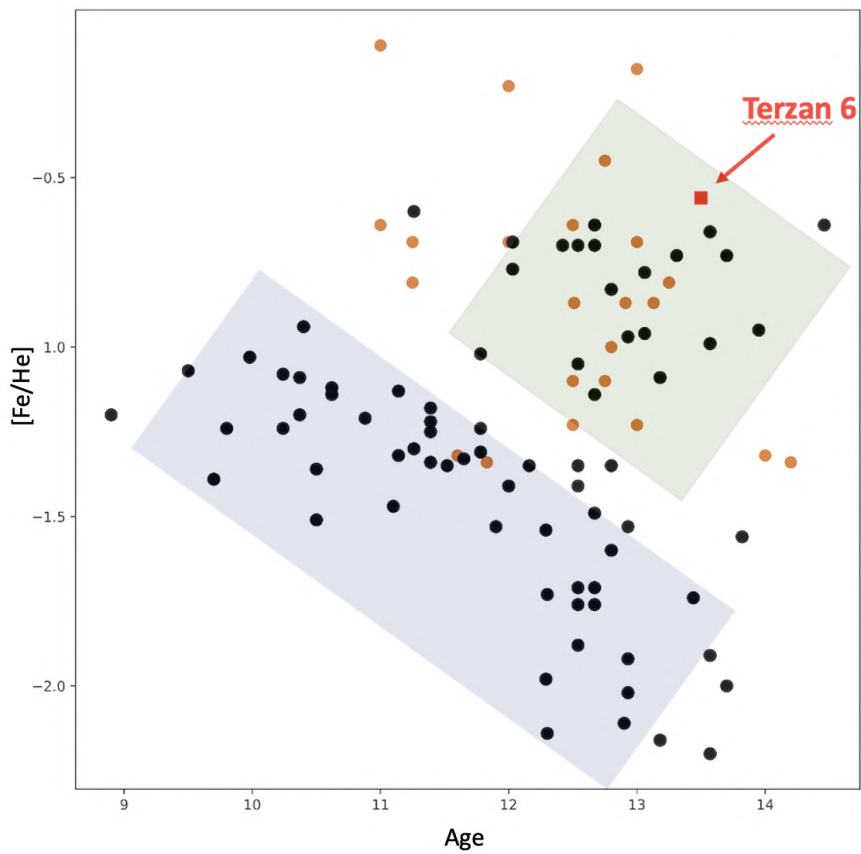The work presented in this Thesis is set in the framework of the use of GCs as possible tracers of the early stages of the formation and evolution of the Milky Way. In particular, this work is part of a larger project aimed at performing detailed photometric analysis and characterization of the population of Galactic Bulge clusters, which has been admittedly poorly studied so far because of the large foreground extinction and stellar density.

To overcome these limitations, this work makes use of a combination of data obtained through adaptive optics-assisted, ground-based facilities and space-based instruments, which guarantee images of superb quality and spatial resolution.

The astrophysical object of study is **Terzan 6**, a globular cluster located in the Galactic Bulge. It is affected by strong extinction (E(B-V)=2.35 (Harris 1996, 2010 edition[79])) and it has been suggested to be one of the densest GC in the Galaxy.

The data set adopted for this master thesis work consists of a combination of images obtained with GeMS and the GSAOI camera (in the J and K_s bands) mounted at the Gemini South Telescope (Chile) and a set of HST images obtained with ACS/WFC (in the F606W and F814W, roughly corresponding to V and I respectively).

Thanks to the high spatial resolution secured by both data sets and to the NIR sensitivity of the Gemini data, which overcome at least partially the limitations due to the large extinction, it has been possible to perform for the first time a detailed study of the stellar population of the GC Terzan 6.

The temporal baseline of about 8 years between the different data sets has been optimal to derive relative proper motions for such a contaminated stellar system. This analysis enabled a clear separation between stellar cluster members and stars belonging to the Galaxy, thus making possible a detailed characterization of stellar populations of the system.

By using cluster member stars, we constrained the variation of the extinction within the field of view, the so-called *differential reddening*, which has an impact on the distribution of stars in a color-magnitude diagram as it stretches all evolutionary sequences.

We found that within the analyzed field of view, reddening varies by ≈0.1 mag, which corresponds to about 5% of the mean reddening in the direction of the system. Single star magnitudes have been then corrected by accounting for this effect.

Both analyses enabled a clear view of the stellar evolutionary sequences of Terzan 6 in the

color-magnitude diagram, thus allowing the first accurate age derivation from resolved stars for the system.

GC ages represent key information to constrain the timescales of formation of the Galactic structures.

The age estimate of Terzan 6 was performed by using the isochrone-fitting approach and two families of stellar evolution models: BASTI (Pietrinferni et al., 2004[60]) and PARSEC[57]. The adoption of different models allows the investigation of possible systematic errors, which may result from different assumptions about stellar physics.

For this analysis, we constrained the distance and average reddening of Terzan 6 by performing a direct comparison with the nearby ($l = 305.89°$, $b = -44.89°$) massive and low-extincted (E(B-V)=0.04) system 47 Tucanae. This is one of the best studied stellar systems in the Galaxy and it shares a similar metallicity ([Fe/H]=-0.72 (Harris 1996, 2010 edition[79])) with Terzan 6, also its distance modulus is well constrained $(m - M)_V$=13.37. We adopted models with metallicity [Fe/H]=-0.60 dex, which is appropriate based on a few direct metallicity measures ([Fe/H]=-0.56; Harris 1996, 2010 edition[79]).

The results we obtained in the comparison are E(B-V)=2.30 $\pm$ 0.23 and $(m - M)_V$=21.44, with no changes in the latter one compared to the literature value (Harris 1996, 2010 edition[79]), the true distance modulus $(m - M)_0$=14.26 $\pm$ 0.72 and the distance d=7.13 $\pm$ 0.70 Kpc.

By using both families of models (BASTI and PARSEC) we obtained an age of 13.5$\pm$0.5 Gyr. The result that we derived is overall consistent, within the errors' range, with the literature ones (Harris 1996, 2010 edition[79]; Barbuy et al., 1997[3]; Fahlman et al., 1995[22]). This value also appears to be consistent, being probably on the older end of the distribution, with that obtained for other GCs analyzed so far in the bulge (see for example Zoccali et al. 2001[81]; Barbuy et al. 2007[4]; Dotter et al. 2010[19]; VandenBerg et al. 2013[78]; Lagioia et al. 2014[39]; Calamida et al. 2014[9]; Ferraro et al. 2016 [24]; Saracino et al. 2016[68], 2019[67]; Kerber et al. 2018[37], 2019[36]) and suggests that the stellar populations in the central regions of the Galaxy formed in the very early stages of the Galaxy formation.

Considering the age we estimated and the adopted metallicity [Fe/H]=-0.56, we placed Terzan 6 in the age-metallicity plane, together with Bulge and Halo globular clusters. Its position is perfectly consistent with the expectation, being in the metal-rich branch of the globular clusters of our Galaxy characterized by an in-situ formation.

Thanks to the high spatial resolution of the adopted data we derived for the first time the center of gravity and the density profile of Terzan 6 by using resolved star counts.

The center of gravity is located at $\alpha_{J200} = 17^h\ 50^m\ 46.9^s$, $\delta_{J200} = -31°\ 16'\ 30.14''$ with an error of 0.53" on α_{J200} and 0.91" on δ_{J200}, which turns out to be at $\approx$ 8.6" from the one reported in the literature (Harris 1996, 2010 edition[79]) based on surface brightness analyses. Starting from the new center of gravity, the radial density profile from number counts was

realized and it was the first one by using resolved stars.

We first tried to fit the profile with a King model only and the best one, according to the χ^2 test, is characterized by $r_c = 2.75''[\pm 0.35]$, $c = 1.91[+0.13, -0.15]$, $r_h = 24.08''$ and $r_t = 229.01'' = 3.82' \pm 1.5'$.

They can be compared with the literature results (Harris 1996, 2010 edition[79]): c=2.50, $r_c = 3''$, $r_h = 26.4''$.

So, since the large c value and the small r_c value can be considered hints of a dynamically evolved cluster (Post core-collapse), we also tried to fit the central region of the density profile with a power law to enhance the presence of a cusp. In this case the obtained structural parameters are $W_0 = 7.20[+0.60, -0.75]$, $r_c = 5.75''[+0.40, -0.75]$, $c = 1.59[+0.0, -0.22]$, $r_h = 25.93''$, $r_t = 232.59'' = 3.88' \pm 1.1'$, while the power law is defined as $\log \Sigma_* = -0.88 \times log$ $r + 1.036$.

Both models were overall consistent, according to the χ^2 test, but due to the large value of c (in the first model) and the presence of a cusp (in the second model), the core collapse scenario is the most plausible.

In conclusion, this work allowed the characterization of the stellar population properties of the bulge GC Terzan 6 with a level of detail never reached before.

This thesis shows the wealth of information that it is possible to obtain even in high-density and large extinction regions such as the Galactic bulge, from the combination of adaptive optics supported systems and space-based instruments.

This analysis shows important applications in the use of state-of-the-art instruments such as JWST and the next generation of ground-based adaptive optics-supported observatories such as the ESO/ELT and the TMT. These instruments are very sensitive to NIR wavelengths that they will sample with a similar spatial resolution to present-day space-based observatories working at optical bands. Hence, these instruments promise to provide a significant contribution to the study of GC in the bulge of the Galaxy and major nearby galaxies.

Bibliography

[1] Jay Anderson et al. "The Acs Survey of Globular Clusters. V. Generating a Comprehensive Star Catalog for each Cluster". In: 135.6 (June 2008), pp. 2055–2073. DOI: 10.1088/0004-6256/135/6/2055. arXiv: 0804.2025 [astro-ph].

[2] H. W. Babcock. "The Possibility of Compensating Astronomical Seeing". In: 65.386 (Oct. 1953), p. 229. DOI: 10.1086/126606.

[3] B. Barbuy, S. Ortolani, and E. Bica. "NTT V, I, Z photometry of the metal-rich bulge globular cluster Terzan 6". In: 122 (May 1997), pp. 483–488. DOI: 10.1051/aas:1997148.

[4] B. Barbuy et al. "NGC 6558: A Blue Horizontal Branch Moderately Metal-Poor Globular Cluster in the Bulge". In: 134.4 (Oct. 2007), p. 1613. DOI: 10.1086/521556.

[5] G. Beccari et al. "Deep Multi-telescope Photometry of NGC 5466. I. Blue Stragglers and Binary Systems". In: 776.1, 60 (Oct. 2013), p. 60. DOI: 10.1088/0004-637X/776/1/60. arXiv: 1308.5810 [astro-ph.SR].

[6] J. M. Beckers. "Detailed compensation of atmospheric seeing using multiconjugate adaptive optics." In: *Active telescope systems.* Ed. by Francois J. Roddier. Vol. 1114. Society of Photo-Optical Instrumentation Engineers (SPIE) Conference Series. Sept. 1989, pp. 215–217. DOI: 10.1117/12.960826.

[7] E. Bertin and S. Arnouts. "SExtractor: Software for source extraction." In: 117 (June 1996), pp. 393–404. DOI: 10.1051/aas:1996164.

[8] James Binney and Scott Tremaine. *Galactic dynamics.* 1987.

[9] A. Calamida et al. "Strömgren and near-infrared photometry of metal-rich bulge globular clusters. I. NGC 6528 and its surrounding field". In: 565, A8 (May 2014), A8. DOI: 10.1051/0004-6361/201323081. arXiv: 1402.0446 [astro-ph.GA].

[10] Eleazar R. Carrasco et al. "Results from the commissioning of the Gemini South Adaptive Optics Imager (GSAOI) at Gemini South Observatory". In: *Adaptive Optics Systems III.* Ed. by Brent L. Ellerbroek, Enrico Marchetti, and Jean-Pierre Véran. Vol. 8447. Society of Photo-Optical Instrumentation Engineers (SPIE) Conference Series. July 2012, 84470N, 84470N. DOI: 10.1117/12.926240.

[11]   L. Casagrande and Don A. VandenBerg. "Synthetic stellar photometry - I. General considerations and new transformations for broad-band systems". In: 444.1 (Oct. 2014), pp. 392–419. DOI: 10.1093/mnras/stu1476. arXiv: 1407.6095 [astro-ph.SR].

[12]   Bogdan C. Ciambur. "Profiler – A Fast and Versatile New Program for Decomposing Galaxy Light Profiles". In: *Publications of the Astronomical Society of Australia* 33 (2016), e062. DOI: 10.1017/pasa.2016.60.

[13]   Richard M. Clare, Marcos A. van Dam, and Antonin H. Bouchez. "Modeling low order aberrations in laser guide star adaptive optics systems". In: *Optics Express* 15.8 (Apr. 2007), pp. 4711–4725. DOI: 10.1364/OE.15.004711.

[14]   Cosmic-Lab. *BHKing: King and Wilson single-mass models with IMBH for Globular Clusters*. URL: hhttp://www.cosmic-lab.eu/bhking/index.php.

[15]   Chiara Crociati et al. "First Evidence of Multi-iron Subpopulations in the Bulge Fossil Fragment Candidate Liller 1". In: 951.1, 17 (July 2023), p. 17. DOI: 10.3847/1538-4357/acd382. arXiv: 2305.04595 [astro-ph.GA].

[16]   E. Dalessandro et al. "Double Blue Straggler Sequences in Globular Clusters: The Case of NGC 362". In: 778.2, 135 (Dec. 2013), p. 135. DOI: 10.1088/0004-637X/778/2/135. arXiv: 1310.2389 [astro-ph.SR].

[17]   E. Dalessandro et al. "IC 4499 revised: Spectro-photometric evidence of small light-element variations". In: 618, A131 (Oct. 2018), A131. DOI: 10.1051/0004-6361/201833650. arXiv: 1807.07618 [astro-ph.SR].

[18]   Emanuele Dalessandro et al. "Clues to the Formation of Liller 1 from Modeling Its Complex Star Formation History". In: 940.2, 170 (Dec. 2022), p. 170. DOI: 10.3847/1538-4357/ac9907. arXiv: 2210.05694 [astro-ph.GA].

[19]   Aaron Dotter et al. "The ACS Survey of Galactic Globular Clusters. IX. Horizontal Branch Morphology and the Second Parameter Phenomenon". In: 708.1 (Jan. 2010), pp. 698–716. DOI: 10.1088/0004-637X/708/1/698. arXiv: 0911.2469 [astro-ph.SR].

[20]   Linda Dressel and Mariarosa Marinelli. "WFC3 Instrument Handbook for Cycle 31 v. 15.0". In: *WFC3 Instrument Handbook for Cycle 31 v. 15.0*. Vol. 15. 2023, p. 15.

[21]   Bruce G. Elmegreen, Frédéric Bournaud, and Debra Meloy Elmegreen. "Bulge Formation by the Coalescence of Giant Clumps in Primordial Disk Galaxies". In: 688.1 (Nov. 2008), pp. 67–77. DOI: 10.1086/592190. arXiv: 0808.0716 [astro-ph].

[22]   G. G. Fahlman, K. A. Douglas, and I. B. Thompson. "Infrared Photometry of the Globular Cluster Terzan 6". In: 110 (Nov. 1995), p. 2189. DOI: 10.1086/117678.

[23]   F. R. Ferraro et al. "A new class of fossil fragments from the hierarchical assembly of the Galactic bulge". In: *Nature Astronomy* 5 (Jan. 2021), pp. 311–318. DOI: 10.1038/s41550-020-01267-y. arXiv: 2011.09966 [astro-ph.GA].

[24]   F. R. Ferraro et al. "The Age of the Young Bulge-like Population in the Stellar System Terzan 5: Linking the Galactic Bulge to the High-z Universe". In: 828.2, 75 (Sept. 2016), p. 75. DOI: 10.3847/0004-637X/828/2/75. arXiv: 1609.01515 [astro-ph.GA].

[25]   F. R. Ferraro et al. "The cluster Terzan 5 as a remnant of a primordial building block of the Galactic bulge". In: 462.7272 (Nov. 2009), pp. 483–486. DOI: 10.1038/nature08581. arXiv: 0912.0192 [astro-ph.GA].

[26]   Francesco R. Ferraro et al. "Blue Straggler Stars: The Spectacular Population in M80". In: 522.2 (Sept. 1999), pp. 983–990. DOI: 10.1086/307700. arXiv: astro-ph/9904196 [astro-ph].

[27]   Duncan A. Forbes and Terry Bridges. "Accreted versus in situ Milky Way globular clusters". In: *Monthly Notices of the Royal Astronomical Society* 404.3 (May 2010), pp. 1203–1214. ISSN: 0035-8711. DOI: 10.1111/j.1365-2966.2010.16373.x. eprint: https://academic.oup.com/mnras/article-pdf/404/3/1203/18692252/mnras0404-1203.pdf. URL: https://doi.org/10.1111/j.1365-2966.2010.16373.x.

[28]   R. Foy and A. Labeyrie. "Feasibility of adaptive telescope with laser probe". In: 152.2 (Nov. 1985), pp. L29–L31.

[29]   V. Grieco et al. "Chemical evolution of the Galactic bulge: different stellar populations and possible gradients". In: 548, A60 (Dec. 2012), A60. DOI: 10.1051/0004-6361/201219761. arXiv: 1209.4462 [astro-ph.GA].

[30]   W. E. Harris. "Spatial structure of the globular cluster system and the distance to the galactic center." In: 81 (Dec. 1976), pp. 1095–1116. DOI: 10.1086/111991.

[31]   M. Hénon. "Sur l'évolution dynamique des amas globulaires". In: *Annales d'Astrophysique* 24 (Feb. 1961), p. 369.

[32]   A. Immeli et al. "Gas physics, disk fragmentation, and bulge formation in young galaxies". In: 413 (Jan. 2004), pp. 547–561. DOI: 10.1051/0004-6361:20034282. arXiv: astro-ph/0312139 [astro-ph].

[33]   Roy Irwan. "Wavefront estimation in astronomical imaging : a thesis presented for the degree of Doctor of Philosophy, University of Canterbury". In: (July 2023).

[34]   Christian I. Johnson et al. "Exploring the Chemical Composition and Double Horizontal Branch of the Bulge Globular Cluster NGC 6569". In: 155.2, 71 (Feb. 2018), p. 71. DOI: 10.3847/1538-3881/aaa294. arXiv: 1801.10475 [astro-ph.SR].

[35] James A. Kaduk and Joel Reid. "Typical values of Rietveld instrument profile coefficients". In: *Powder Diffraction* 26.1 (Mar. 2011), pp. 88–93. DOI: 10.1154/1.3548128.

[36] L. O. Kerber et al. "A deep view of a fossil relic in the Galactic bulge: the Globular Cluster HP 1". In: 484.4 (Apr. 2019), pp. 5530–5550. DOI: 10.1093/mnras/stz003. arXiv: 1901.03721 [astro-ph.SR].

[37] L. O. Kerber et al. "Ages of the Bulge Globular Clusters NGC 6522 and NGC 6626 (M28) from HST Proper-motion-cleaned Color-Magnitude Diagrams". In: 853.1, 15 (Jan. 2018), p. 15. DOI: 10.3847/1538-4357/aaa3fc. arXiv: 1801.03876 [astro-ph.SR].

[38] Ivan R. King. "The structure of star clusters. III. Some simple dynamical models". In: 71 (Feb. 1966), p. 64. DOI: 10.1086/109857.

[39] E. P. Lagioia et al. "On the Kinematic Separation of Field and Cluster Stars across the Bulge Globular NGC 6528". In: 782.1, 50 (Feb. 2014), p. 50. DOI: 10.1088/0004-637X/782/1/50. arXiv: 1312.2272 [astro-ph.SR].

[40] B. Lanzoni et al. "New Density Profile and Structural Parameters of the Complex Stellar System Terzan 5". In: 717.2 (July 2010), pp. 653–657. DOI: 10.1088/0004-637X/717/2/653. arXiv: 1005.2847 [astro-ph.GA].

[41] Aigen Li et al. "Dust in the Local Group: A Conference in honour of David Block and Bruce Elmegreen". In: *Lessons from the Local Group: A Conference in honor of David Block and Bruce Elmegreen.* 2015, pp. 85–103. DOI: 10.1007/978-3-319-10614-4_8.

[42] Enrico Marchetti et al. "On-sky Testing of the Multi-Conjugate Adaptive Optics Demonstrator". In: *The Messenger* 129 (Sept. 2007), pp. 8–13.

[43] D. Massari et al. "Terzan 5: a fossil remnant of the Galactic bulge." In: 84 (Jan. 2013), p. 236. DOI: 10.48550/arXiv.1301.2436. arXiv: 1301.2436 [astro-ph.GA].

[44] Sophia Medallon and Dan Welty. "STIS Instrument Handbook for Cycle 31 v. 22.0". In: *STIS Instrument Handbook for Cycle 31 v. 22.* Vol. 22. 2023, p. 22.

[45] P. Miocchi. "Central energy equipartition in multimass models of globular clusters". In: 366.1 (Feb. 2006), pp. 227–234. DOI: 10.1111/j.1365-2966.2005.09842.x. arXiv: astro-ph/0511263 [astro-ph].

[46] A. F. J. Moffat. "A Theoretical Investigation of Focal Stellar Images in the Photographic Emulsion and Application to Photographic Photometry". In: 3 (Dec. 1969), p. 455.

[47] P. Montegriffo et al. "IR-array photometry of Galactic globular clusters - II. JK photometry of 47 TUC". In: 276.3 (Oct. 1995), pp. 739–752. DOI: 10.1093/mnras/276.3.739.

[48] NASA. *Hubble Space Telescope*. URL: `https://hubblesite.org/mission-and-telescope` (visited on 10/06/2023).

[49] Benoit Neichel et al. "Gemini multiconjugate adaptive optics system review - II. Commissioning, operation and overall performance". In: 440.2 (May 2014), pp. 1002–1019. DOI: `10.1093/mnras/stu403`. arXiv: `1402.6906 [astro-ph.IM]`.

[50] E. Nelan and et al. *Fine Guidance Sensor Instrument Handbook for Cycle 21 v.20.0*. 2012.

[51] M. Ness et al. "ARGOS - III. Stellar populations in the Galactic bulge of the Milky Way". In: 430.2 (Apr. 2013), pp. 836–857. DOI: `10.1093/mnras/sts629`. arXiv: `1212.1540 [astro-ph.GA]`.

[52] European Southern Observatory. *Adaptive optics with MAD*. URL: `https://www.eso.org/public/` (visited on 10/06/2023).

[53] International GEMINI Observatory. URL: `https://www.gemini.edu` (visited on 10/06/2023).

[54] L. Origlia, R. M. Rich, and S. M. Castro. "High resolution infrared spectra of Bulge Globular Clusters: Liller 1, NGC 6553, and Ter 5". In: *American Astronomical Society Meeting Abstracts*. Vol. 199. American Astronomical Society Meeting Abstracts. Dec. 2001, 56.16, p. 56.16.

[55] L. Origlia et al. "Spectroscopy Unveils the Complex Nature of Terzan 5". In: 726.2, L20 (Jan. 2011), p. L20. DOI: `10.1088/2041-8205/726/2/L20`. arXiv: `1012.2047 [astro-ph.GA]`.

[56] Livia Origlia. "A review of the chemical abundances and kinematics of the Galactic bulge". In: *Setting the scene for Gaia and LAMOST*. Ed. by Sofia Feltzing et al. Vol. 298. Jan. 2014, pp. 28–39. DOI: `10.1017/S1743921313006170`.

[57] INAF (OAPd-INAF) Osservatorio Astronomico di Padova. URL: `http://stev.oapd.inaf.it/cgi-bin/cmd`.

[58] Cristina Pallanca et al. "High-resolution Extinction Map in the Direction of the Strongly Obscured Bulge Fossil Fragment Liller 1". In: 917.2, 92 (Aug. 2021), p. 92. DOI: `10.3847/1538-4357/ac0889`. arXiv: `2106.02448 [astro-ph.GA]`.

[59] Thomas Pfrommer and Paul Hickson. "High-resolution mesospheric sodium observations for extremely large telescopes". In: *Adaptive Optics Systems II*. Ed. by Brent L. Ellerbroek et al. Vol. 7736. Society of Photo-Optical Instrumentation Engineers (SPIE) Conference Series. July 2010, 773620, p. 773620. DOI: `10.1117/12.857703`.

[60] Adriano Pietrinferni et al. "A Large Stellar Evolution Database for Population Synthesis Studies. I. Scaled Solar Models and Isochrones". In: 612.1 (Sept. 2004), pp. 168–190. DOI: 10.1086/422498. arXiv: astro-ph/0405193 [astro-ph].

[61] Roberto Ragazzoni, Jacopo Farinato, and Enrico Marchetti. "Adaptive optics for 100-m-class telescopes: new challenges require new solutions". In: *Adaptive Optical Systems Technology*. Ed. by Peter L. Wizinowich. Vol. 4007. Society of Photo-Optical Instrumentation Engineers (SPIE) Conference Series. July 2000, pp. 1076–1087. DOI: 10.1117/12.390313.

[62] R. M. Rich. "The Galactic bulge (Review)". In: *The Central Regions of the Galaxy and Galaxies*. Ed. by Yoshiaki Sofue. Vol. 184. Jan. 1998, p. 11.

[63] F. Rigaut and E. Gendron. "Laser guide star in adaptive optics: the tilt determination problem." In: 261 (Aug. 1992), pp. 677–684.

[64] François Rigaut and Benoit Neichel. "Multiconjugate Adaptive Optics for Astronomy". In: 56 (Sept. 2018), pp. 277–314. DOI: 10.1146/annurev-astro-091916-055320.

[65] Gabriele Rodeghiero. *Lecture notes of Astronomical Instrumentation*. Department of Physics and Astronomy, University of Bologna, 2022.

[66] J. E. Ryon. "ACS Instrument Handbook for Cycle 31 v. 22.0". In: *ACS Instrument Handbook for Cycle 31 v. 22.0*. Vol. 22. 2023, p. 22.

[67] S. Saracino et al. "A Panchromatic View of the Bulge Globular Cluster NGC 6569". In: 874.1, 86 (Mar. 2019), p. 86. DOI: 10.3847/1538-4357/ab07c4. arXiv: 1902.05558 [astro-ph.GA].

[68] S. Saracino et al. "Ultra-deep GEMINI Near-infrared Observations of the Bulge Globular Cluster NGC 6624." In: 832.1, 48 (Nov. 2016), p. 48. DOI: 10.3847/0004-637X/832/1/48. arXiv: 1609.02152 [astro-ph.SR].

[69] Ata Sarajedini. "The HST/ACS Survey of Galactic Globular Clusters". In: *Stellar Populations as Building Blocks of Galaxies*. Ed. by Alexandre Vazdekis and Reynier Peletier. Vol. 241. Aug. 2007, pp. 218–222. DOI: 10.1017/S1743921307007946.

[70] D. R. Soderblom. "COS Instrument Handbook v. 15.0". In: *COS Instrument Handbook v. 15.0*. Vol. 15. 2023, p. 15.

[71] Peter B. Stetson. *DAOPHOT: Crowded-field Stellar Photometry Package*. Astrophysics Source Code Library, record ascl:1104.011. Apr. 2011. ascl: 1104.011.

[72] Peter B. Stetson. "The Center of the Core-Cusp Globular Cluster M15: CFHT and HST Observations, ALLFRAME Reductions". In: 106 (Mar. 1994), p. 250. DOI: 10.1086/133378.

[73] ACSTOOLS Space Telescope Science Institute (STScI). *ACS Zeropoint Calculator.* URL: https://acszeropoints.stsci.edu.

[74] ACSTOOLS Space Telescope Science Institute (STScI). *Aperture Corrections.* URL: https://www.stsci.edu/hst/instrumentation/acs/data-analysis/aperture-corrections.

[75] A. Terzan. "Six nouveaux amas stellaires (Terzan 3-8) dans la region du centre de la Voie lactee et les constellations du Scorpion et du Sagittaire." In: *Academie des Sciences Paris Comptes Rendus Serie B Sciences Physiques* 267 (Jan. 1968), pp. 1245–1248.

[76] E. Valenti, F. R. Ferraro, and L. Origlia. "Near-infrared properties of 12 globular clusters towards the inner bulge of the Galaxy". In: 402.3 (Mar. 2010), pp. 1729–1739. DOI: 10.1111/j.1365-2966.2009.15991.x. arXiv: 0911.1264 [astro-ph.GA].

[77] E. Valenti, L. Origlia, and R. M. Rich. "High-resolution near-infrared spectra of NGC 6624 and 6569". In: 414.3 (July 2011), pp. 2690–2695. DOI: 10.1111/j.1365-2966.2011.18580.x. arXiv: 1103.0233 [astro-ph.SR].

[78] Don A. VandenBerg et al. "The Ages of 55 Globular Clusters as Determined Using an Improved VĤB_TO Method along with Color-Magnitude Diagram Constraints, and Their Implications for Broader Issues". In: 775.2, 134 (Oct. 2013), p. 134. DOI: 10.1088/0004-637X/775/2/134. arXiv: 1308.2257 [astro-ph.GA].

[79] McMaster University William E. Harris. *CATALOG OF PARAMETERS FOR MILKY WAY GLOBULAR CLUSTERS: THE DATABASE.* URL: https://physics.mcmaster.ca/~harris/mwgc.dat.

[80] Peter Wizinowich. "Adaptive optics in astronomy". In: *Contemporary Physics* 56.4 (Oct. 2015), pp. 432–450. DOI: 10.1080/00107514.2015.1041765.

[81] M. Zoccali et al. "The Proper Motion of the Globular Cluster NGC 6553 and of Bulge Stars with the Hubble Space Telescope". In: 121.5 (May 2001), pp. 2638–2646. DOI: 10.1086/320411.

[82] Manuela Zoccali and Elena Valenti. "The 3D Structure of the Galactic Bulge". In: 33, e025 (June 2016), e025. DOI: 10.1017/pasa.2015.56. arXiv: 1601.02839 [astro-ph.GA].